CONTROL STRATEGIES FOR TIMESTEP SELECTION IN FINITE ELEMENT SIMULATION OF INCOMPRESSIBLE FLOWS AND COUPLED HEAT AND MASS TRANSFER

Andréa M. P. Valli

Technical Report
COPPE/Federal University of Rio de Janeiro
PO Box 68506, Rio de Janeiro RJ 21945-970, Brazil

November, 2001

CONTROL STRATEGIES FOR TIMESTEP SELECTION IN THE SIMULATION OF INCOMPRESSIBLE FLOWS AND COUPLED HEAT AND MASS TRANSFER

Andréa Maria Pedrosa Valli

November/2001

Adaptive techniques for automatic timestep selection are probably the most important means to improve efficiency of a given integration method in the numerical solution of ordinary differential equations. These strategies are usually based on approximate local truncation error measures or on purely heuristic considerations. We remark that this process can be viewed as an examples of feedback control problems. In the present work, we propose two PID timestep control algorithms for finite element simulations of steady-state and transient 2D viscous flow and coupled reaction-convection-diffusion processes combined with surface tension effects. We solve chemical reaction systems, Rayleigh-Benard and Rayleigh-Benard-Marangoni flows and heat and mass transfer by natural convection.

Numerical experiments confirm that we can find approximate solutions with a smaller number of steps without any significant loss of accuracy. Moreover, the PID controller produces a very smooth curve suggesting that a robust control algorithm is possible. Numerical results also show that the non-dimensional kinetic energy could be a suitable parameter to improve the timestep selection when coordinated with the convergence control of nonlinear iterations. Further, computational cost of the selection procedures are negligible, since they involve only storing a few extra vectors, computation of norms and evaluation of kinetic energy.

ESTRATÉGIAS DE CONTROLE PARA A SELEÇÃO DE PASSO DE TEMPO PARA ANÁLISE DE ESCOAMENTOS INCOMPRESSÍVEIS ACOPLADOS COM TRANSPORTE DE CALOR E MASSA

Andréa Maria Pedrosa Valli

Novembro/2001

Técnicas adaptativas para a seleção de passo de tempo são as mais importantes ferramentas para melhorar a eficiência de um método de integração de sistemas de ODE's. Estas estratégias são geralmente baseadas em medidas do erro de truncamento local ou por considerações heurísticas. No entanto, este processo pode ser visto como um problema de controle retroalimentado. No presente trabalho, propomos dois algoritmos de controle PID de passo de tempo para as simulações em elementos finitos de escoamentos viscosos e incompressíveis acoplados à processos de reação, difusão e convecção combinados com efeitos na tensão superficial. Resolvemos sistemas de reações químicas, problemas de Rayleigh-Benard-Marangoni e transferência de calor e massa por conveção natural.

Experimentos numéricos confirmam que encontramos soluções aproximadas com um número menor de passos sem nenhuma perda significativa de precisão. Os controladores produzem uma curva bastante suave para a variação do passo, sugerindo que um algoritmo de controle robusto é possível. Resultados numéricos demostraram que a energia cinética é um parâmetro adequado para a seleção de passo de tempo quando coordenado com a convergência das iterações não lineares. Além disso, os custos computacionais para os processos de seleção do passo são desprezíveis, uma vez que involvem apenas o armazenamento de alguns vetores, o cálculo de normas e avaliação da energia cinética.

Contents

List of Figures

List of Tables

Chapter 1

Introduction

With the evolution of finite element methodology and its extension to more complex classes of coupled problems there has been an increasing need for improved algorithms and other enhancements such as adaptive grid refinement and coarsening. Several adaptive timestepping selection strategies have been studied as a means to provide stable accurate transient (and steady state) solutions more efficiently. This adaptive timestepping selection process is usually approached by means of local truncation error analysis. In the same way, the adaptive grid schemes use feedback from the computed solution on a given intermediate grid to ascertain where the grid should be locally refined. We remark that both of these processes (adaptive timestep selection and adaptive grid refinement) can be viewed as examples of feedback control problems. This brings us to the main theme of the present work - the utilization of feedback control algorithms for timestep selection in conjunction of finite element analysis in the simulations of steady-state and transient 2D viscous flow and coupled reaction-convection-diffusion processes combined with surface tension effects.

Besides the control algorithms for timestep selection, we are also interested in the numerical simulation of chemical reaction systems, Rayleigh-Benard and Rayleigh-Benard-Marangoni flows, heat and mass transfer by natural convection and double diffusive convection. In particular, we want to study the performance of the controllers to solve these classes of application problems, perform numerical experiments for different parameters that influence the problems, and compare our results with those found in the literature. Practical applications of the related problems include, for example, nonisothermal reaction on a catalyst section [33, 58], pattern formation during solidification and welding in manufacturing processes [78, 7, 25], physical behavior of fluids under microgravity conditions [13, 38, 31], semiconductor crystal growth and double diffusive and Marangoni instabilities [65, 63, 62, 66, 42].

The first class of problems studied in this work involves nonlinear flow and reactive transport. We solve isothermal reaction inside a porous catalyst and chemical reaction on a catalyst section with heat effects included [58, 33]. In the second problem, the process is highly nonlinear because of an exponential chemical reaction term arising from the temperature dependence of the chemical reaction rate. As a consequence, we need to choose a very small timestep to obtain convergence of the nonlinear iterations in the transport equation. Therefore, efficient computation of the transport process in this example demands the use of a timestep selection algorithm.

The second class of application problems we investigate is Rayleigh-Benard flows and Rayleigh-Benard-Marangoni flows. When buoyancy forces due to temperature gradients are the dominant component in driving the flow, we have a Rayleigh-Benard problem [31, 30, 25]. For example, when a thin horizontal layer of fluid between two horizontal plates is heated from below, a temperature gradient is generated across the plates. At a critical Rayleigh number, circular convection cells set in. If the plate is removed from the upper surface, then the surface tension effects associated with temperature gradients on the free surface become important. Now both buoyancy and thermocapillary effects provide the dominant forces driving the flow, termed Rayleigh-Benard-Marangoni problems [61, 18, 80]. Rayleigh-Benard-Marangoni problems become very popular as prototypes of complex behavior where nonlinear theories of pattern formation may be tested.

When heat and species transfer exist within a fluid layer, the temperature and concentration gradients create a coupled transport mode, called double diffusion. This phenomenon is found in fluid mixtures of two components having two different molecular diffusivities, where the potential energy of one component may be released by differential diffusion, thus driving the convective motion, even though the system may be gravitation stable [69, 70, 56, 42, 66]. One example of double diffusive convection is when a hot salty fluid layer (slower diffusion) is underlying a cold fresh fluid layer (faster diffusion) [63, 62, 66]. In the present work, the third class of application problems we solve is simultaneous heat and mass transfer by natural convection above horizontal surfaces [65]. Our future works involves solving the coupling between Marangoni (thermal and solutal) convection and double diffusion convection in a multi-cavity system with a non-deforming free surface.

Viscous flow is modeled by the incompressible 2D Navier-Stokes equations, written in primitive variables, with a forcing term that may depend on temperature

and concentration. In the transient transport equation, the time rate of change (evolution) of the species component fields may depend on advection, diffusion and chemical reactions. There are two primary approaches to the numerical formulation of the class of coupled problems we are investigating. One approach is called the decoupled formulation, where the momentum and continuity equations are solved first, in each timestep or iteration, lagging the temperature and concentration vector in the forcing term. Then, the transport equations are solved with the computed velocities as input. The second approach, called the fully-coupled formulation, requires simultaneous coupled solution of the flow and transport systems. Here, we consider only the decoupled formulation.

Among the most notable finite element formulations for incompressible flows are the mixed (or multiplier) method [16, 55], the penalty method [81, 55, 14, 15, 16], the stabilized formulations, such as, the Streamline-Upwind/Petrov-Galerkin (SUPG) formulation [44, 11, 23, 68], Galerkin/Least-Squares (GLS) formulation [45, 17, 28], Pressure-Stabilizing/Petrov-Galerkin (PSPG) formulation [67, 21] and fractional step formulations [8, 22]. We can also find finite element formulations based on the stream function-vorticity equations [16, 3]. The finite element method makes use of a spatial discretization and a weighted residual formulation to arrive at a system of matrix equations. The Galerkin method, which is the most common weighted residual formulation, uses weighting and interpolation functions from the same class of functions. The success of the Galerkin finite element method in several application problems is due to its *best approximation minimization property* [43], which means that the difference between the finite element solution and the exact solution is minimized with respect to a certain norm. When the problem is convection-dominated, the Galerkin method loses this property. For general treatments of these issues see, for example, Carey and Oden [16], Zienkiewicz [81], Hughes [43] and Bathe [4].

The subject of finite element approximations to incompressible flow problems encompasses several mixed and penalty formulations. The essential character of mixed methods is exhibited in the framework of a constrained variational problem, in which both velocities and pressure must be approximated. The formal development of a mixed finite element analysis is quite straightforward and the method has been extensively applied (see, e.g., [57, 35, 54]). The penalty approach for the Navier-Stokes problem is designed to determine an approximate formulation involving only velocities and not pressures. Hence the size of the problem is reduced accordingly. The divergence-free condition $\nabla \cdot \mathbf{u} = 0$ is viewed as a constraint condition embedded

in the variational problem by using a penalty term. In the present work, we are only interested in the velocity solution and the associated coupled transport processes. Hence, for simplicity and convenience we use a penalty method to enforce the incompressibility constraint.

In computation of incompressible Navier-Stokes equations for convection-dominated flows, the Galerkin method loses the *best approximation property*, and solutions are often corrupted by spurious oscillations. In order to overcome or minimize those oscillations, Petrov-Galerkin formulations, which modify the Galerkin's weighting functions by adding a perturbation term, have been derived and used with success in the analysis of convection-dominated flows. The SUPG stabilization technique was first introduced by Hughes and Brooks in [44], and investigated in detail by Brooks and Hughes in [11]. The SUPG techniques are consistent stabilization methods, in the sense that the exact solution still satisfies the stabilized formulation, just as it satisfies the Galerkin formulation of the problem. The perturbation term in this method acts only in the streamline direction, chosen as upwind direction, resulting in good stability and accuracy properties if the exact solution is regular, showing a convergence improvement over the Galerkin method. Since the application problems we are investigating in this work are not convection-dominated, the penalty method works well for the Navier-Stokes equations.

For the transport equations, we use a SUPG formulation to find approximate solutions for the temperature and species concentration. Although we are using a SUPG formulation for the transport equation, the perturbation term can always be turned off if the problem is not convection-dominated. Spatial discretization of the Navier-Stokes equations gives rise to a non-linear semi-discrete ODE system, linearized by successive approximations and integrated implicitly using a Crank-Nicolson scheme. The solutions of the linear systems are obtained using a frontal solver. In the transport equations, we use a Crank-Nicolson scheme to integrate in time, the Newton's method to solve the nonlinear algebraic system, and a frontal solver for the linear system. Errors and computational efficiency in the transient solution of the coupled problems are controlled by automatic timestep control algorithms.

Adaptive techniques for automatic timestep selection are probably the most important means to improve efficiency of a given integration method in the numerical solution of ordinary differential equations. These strategies are usually based on approximate local truncation error measures or on purely heuristic considerations.

For example, standard automatic timestep selection algorithms use an estimate of the local truncation error to adjust the stepsize in accordance with a user-specified accuracy requirement, as shown in [51, 59, 9, 60]. Gresho, Sani and Engelman in [37] use a predictor-corrector scheme with a time truncation estimate for error control. Winget and Hughes [79], Johan, Hughes and Shakib [49] and Jacob and Ebecken [48] develop stepsize selection schemes based on heuristic rules for transient heat conduction, compressible Navier-Stokes equations and structural dynamics problems, respectively. However, Gustafsson, Lundh and Söderlind [39] showed that adaptive timestep selection can be viewed as a standard automatic control problem, which motivated Hairer and Wanner [41] to derive a timestep selection algorithm using the concept of proportional-integral-derivative (PID) control. Later, Coutinho and Alves [24] use this approach in their work of finite element simulation of miscible displacements in porous media. In this work, we propose two PID timestep control algorithms based on controlling accuracy or the convergence rate of the successive iterations [71, 74, 75, 76, 73, 72].

The first control utilizes normalized changes in the variables of interest (velocities, temperature, concentration, etc) to compute the local truncation errors. In the second control, the timestep size is limited by the normalized changes in the nondimensional kinetic energy or by the rate of convergence of the successive approximations. The efficiency of these controls are compared with another timestepping strategy developed by Winget and Hughes in [79]. We demonstrate that, with the controllers, we find approximate solutions with a smaller number of steps without any significant loss of accuracy. In addition, the controllers also produce a smooth variation of timestep, suggesting that a robust control algorithm is possible.

The outline of this work is as follows. In Chapter 2 we present the class of transient coupled problems under investigation, the finite element formulations and the solution algorithm. In Chapter 3 we discuss the two control algorithms for timestep selection, and we present the algorithm for timestep selection suggested by Winget and Hughes. In Chapter 4 we provide results of the numerical experiments to validate the finite element formulations of the Navier-Stokes equations, the transport equations and our timestep control algorithms. In Chapter 5 we apply the first timestep control algorithm to solve nonlinear flow and reactive transport. In Chapter 6 we study the performance of the controllers to solve Rayleigh-Benard and Rayleigh-Benard-Marangoni problems, and compare their efficiency with the scheme proposed by Winget and Hughes. In Chapter 7 we solve simultaneous heat and mass transfer

by natural convection above horizontal surfaces. Finally, in Chapter 8 we presented some conclusions and opportunities for future study.

Chapter 2

Formulation and Approximation

In this chapter we present the class of coupled flow and transport equations under investigation, the finite element formulations and the solution approach. In the first section, we state the class of transient coupled problems; then, we describe the penalty finite element formulation for the transient Navier-Stokes equations. Following this, the SUPG stabilization technique for the transient transport equations is developed. Finally, the solution algorithm to obtain approximate transient solutions for the velocity field, temperature and concentration is presented.

2.1 Coupled Viscous Flow and Transport

We consider the stationary and transient flow of a viscous incompressible fluid as described by the Navier-Stokes equations coupled to the transport of heat and mass by convection, conduction and reaction in the fluid including surface tension effects. For example, in Rayleigh-Benard-Marangoni flows buoyancy is included as a temperature dependent body force term in the momentum equation, and the effect of thermocapillary surface tension enters as an applied surface shear stress that is dependent on the surface temperature gradient [30, 13, 75]. An exponential chemical reaction term arising from the temperature dependence of the chemical reaction rate is included, coupling the heat and mass transfer equations [33, 71]. Finally, in double diffusion problems heat and species transfer exist within a fluid and the surface tension depends on the surface temperature and concentration gradients [63, 42].

The transient Navier Stokes equations for viscous flow of an incompressible fluid may be written as

$$\frac{\partial \mathbf{u}}{\partial t} + \mathbf{u} \cdot \nabla \mathbf{u} - \nu \nabla^2 \mathbf{u} + \frac{1}{\rho} \boldsymbol{\nabla} p = \mathbf{q} + \mathbf{f}(T, c) \quad \text{in } \Omega \tag{2.1}$$

$$\boldsymbol{\nabla} \cdot \mathbf{u} = 0 \quad \text{in } \Omega \tag{2.2}$$

where Ω is the flow domain, $\mathbf{u}$ is the velocity vector, p is the pressure, $\nu = \frac{\mu}{\rho}$ is the kinematic viscosity, ρ is the density, $\mathbf{q}$ is an applied body force and $\mathbf{f}(T, c)$ is a temperature (T) and concentration (c) dependent body force. For example, $\mathbf{f}(T, c)$ may be a buoyancy force given by $\mathbf{f}(T, c) = \mathbf{g}(\beta_T(T - T_0) - \beta_c(c - c_0))$ where $\mathbf{g}$ is the gravity vector, β_T and β_c are the thermal and solutal volume expansion coefficients, and T_0 and c_0 are reference temperature and concentration. We assume that there is no slip at the solid walls $\partial\Omega_1$,

$$\mathbf{u} = \mathbf{u_w} \quad \text{on } \partial\Omega_1, \tag{2.3}$$

where $\mathbf{u_w}$ is the specified wall boundary velocity. The Marangoni problem involves a shear stress boundary condition on the free surface $\partial\Omega_2$.

The temperature of the fluid is governed by the energy transport equation. Assuming negligible viscous dissipation, we have

$$\rho c_p \frac{\partial T}{\partial t} + \rho c_p \mathbf{u} \cdot \nabla T - \nabla \cdot (k \nabla T) = h_1(T, c) \quad \text{in } \Omega \tag{2.4}$$

where c_p is the specific heat, k is the thermal conductivity, $h_1(T, c)$ is a nonlinear reaction source/sink term, usually associated with chemical reactions, and c is the concentration of the fluid. The boundary conditions are as follows: $T = T_w(x, y)$ (isothermal boundary) or $\frac{\partial T}{\partial \mathbf{n}} = 0$ (adiabatic boundary) on the solid walls $\partial\Omega_3$ where $\mathbf{n}$ is the unit outward normal, and mixed conditions $\alpha_T \frac{\partial T}{\partial \mathbf{n}} = h_c(T - T_e)$ (Robin) on $\partial\Omega_4$, where $\alpha_T = \frac{k}{\rho c_p}$ is the thermal diffusivity, h_c is the heat transfer coefficient for the medium, T_e is the exterior temperature.

Finally, the mass transfer equation for a single species is given by

$$\frac{\partial c}{\partial t} + \mathbf{u} \cdot \nabla c - \nabla \cdot (\alpha_c \nabla c) = h_2(T, c) \quad \text{in } \Omega \tag{2.5}$$

where c is the concentration, α_c is the mass diffusion coefficient, and $h_2(T, c)$ is a nonlinear reaction source/sink term. Concentration, flux or mixed boundary conditions may be applied.

For convenience, we rewrite equations (2.5) for the vector $\mathbf{c}$ of component species. We can handle up to eight different species and temperature in our code, that is, $\mathbf{c} = \{c_s\}$, $s = 1, 2, \cdots, n_s$, where n_s is the number of species. Then, the vector counterpart of the transient transport equation is,

$$\frac{\partial \mathbf{c}}{\partial t} + u_i \frac{\partial \mathbf{c}}{\partial x_i} - \frac{\partial}{\partial x_i}(\mathbf{K}_{ij} \frac{\partial \mathbf{c}}{\partial x_j}) = \mathbf{h_2}(T, \mathbf{c}) \tag{2.6}$$

where repeated indices imply summation over the range of spatial dimensions, u_i is velocity component i, $\mathbf{h_2}(T, \mathbf{c})$ is a nonlinear reaction source/sink term, and $\mathbf{K} =$

$\{\mathbf{k}^{s_1 s_2}\}$ is the diffusion tensor with $s_1, s_2 = 1, 2, \cdots, n_s$. From (2.6) it is clear that the time rate of change (evolution) of the species component fields depends on advection, diffusion and chemical reaction, respectively. Boundary conditions for species concentration or flux and initial conditions for velocities and concentration vectors complete the statement of the problem for (2.1), (2.2), (2.4) and (2.6).

Thus, the class of transient coupled problems we are interested in solving may be summarized by the following equations:

$$\frac{\partial \mathbf{u}}{\partial t} + \mathbf{u} \cdot \nabla \mathbf{u} - \nu \nabla^2 \mathbf{u} + \frac{1}{\rho} \boldsymbol{\nabla} p = \mathbf{q} + \mathbf{f}(T, \mathbf{c}) \quad \text{in } \Omega \tag{2.7}$$

$$\boldsymbol{\nabla} \cdot \mathbf{u} = 0 \quad \text{in } \Omega \tag{2.8}$$

$$\rho c_p \frac{\partial T}{\partial t} + \rho c_p \mathbf{u} \cdot \nabla T - \nabla \cdot (k \nabla T) = h_1(T, \mathbf{c}) \quad \text{in } \Omega \tag{2.9}$$

$$\frac{\partial \mathbf{c}}{\partial t} + \mathbf{u} \cdot \nabla \mathbf{c} - \nabla \cdot (\mathbf{K} \nabla \mathbf{c}) = \mathbf{h_2}(T, \mathbf{c}) \quad \text{in } \Omega \tag{2.10}$$

with initial conditions

$$\mathbf{u}(0) = \mathbf{u}_0 \tag{2.11}$$

$$T(0) = T_0 \tag{2.12}$$

$$\mathbf{c}(0) = \mathbf{c}_0 \tag{2.13}$$

and boundary conditions as follows

- velocities, flux or free surface boundary conditions

$$\mathbf{u} = \mathbf{u_w} \quad \text{or} \quad \nu \nabla \mathbf{u} \cdot \mathbf{n} = 0 \quad \text{on } \partial\Omega_1 \tag{2.14}$$

$$\nu \nabla \mathbf{u} \cdot \mathbf{n} = \boldsymbol{\Gamma}(T, \mathbf{c}) \quad \text{on } \partial\Omega_2 \tag{2.15}$$

- temperature, flux or mixed boundary conditions

$$T = T_w \quad \text{or} \quad k \nabla T \cdot \mathbf{n} = 0 \quad \text{on } \partial\Omega_3 \tag{2.16}$$

$$k \nabla T \cdot \mathbf{n} = h_T (T - T_e) \quad \text{on } \partial\Omega_4 \tag{2.17}$$

- species concentration, flux or mixed boundary conditions

$$\mathbf{c} = \mathbf{c_w} \quad \text{or} \quad \mathbf{K} \nabla \mathbf{c} \cdot \mathbf{n} = 0 \quad \text{on } \partial\Omega_5 \tag{2.18}$$

$$-\mathbf{K} \nabla \mathbf{c} \cdot \mathbf{n} = \gamma \, \mathbf{c} - \boldsymbol{\Psi} \quad \text{on } \partial\Omega_6 \tag{2.19}$$

In the next section we present the penalty finite element formulation for the Navier-Stokes equations, (2.7), (2.8), (2.11), (2.14) and (2.15).

2.2 Penalty Formulation for the Navier-Stokes Equations

For simplicity and convenience we use a penalty method to enforce the incompressibility constraint. The penalty approach for the Navier-Stokes problem is designed to determine an approximate formulation involving only velocities and not pressures, but without the added complexity of requiring special divergence-free elements. Hence the size of the problem is reduced accordingly. The divergence-free condition $\nabla \cdot \mathbf{u} = 0$ is viewed as a constraint condition embedded in the variational problem by using a penalty term.

Let V be the space for the velocities, and consider the following penalized variational formulation for the Navier-Stokes equations [16]: for $\epsilon > 0$, find $\mathbf{u}^\epsilon \in V$ satisfying the initial condition with $\mathbf{u}^\epsilon = \mathbf{u_w}$ on $\partial\Omega_1$ such that

$$\begin{aligned} \int_\Omega (\frac{\partial \mathbf{u}^\epsilon}{\partial t} \cdot \mathbf{v} \;+\; \nu \nabla \mathbf{u}^\epsilon : \nabla \mathbf{v} \;+\; (\mathbf{u}^\epsilon \cdot \nabla)\mathbf{u}^\epsilon \cdot \mathbf{v} \;+\; \frac{1}{\epsilon}(\nabla \cdot \mathbf{u}^\epsilon)(\nabla \cdot \mathbf{v}))\, d\Omega \\ = \int_\Omega (\mathbf{q} + \mathbf{f}(T, \mathbf{c})) \cdot \mathbf{v}\, d\Omega \;+\; \int_{\partial\Omega_2} \mathbf{\Gamma}(T, \mathbf{c}) \cdot \mathbf{v}\, dl \end{aligned} \tag{2.20}$$

for all admissible $\mathbf{v} \in V$ with $\mathbf{v} = \mathbf{0}$ on $\partial\Omega_1$, where the last integral implies the surface shear boundary condition (2.15) at the free surface. For a discussion of coercivity, existence and uniqueness of the solutions see, e.g., [15, 16]. The pressure approximation for the penalty formulation is given by

$$p^\epsilon = -\frac{1}{\epsilon} \nabla \cdot \mathbf{u}^\epsilon \tag{2.21}$$

Consider now approximation of the variational problem (2.20) using finite elements. Let $V^h \subset V$ be the finite element approximation space for velocities. In the usual way, the flow domain Ω is discretized into a union Ω_h of elements Ω_e, e = 1, 2,..., E. Lagrange piecewise polynomials are used as global basis functions ϕ_j, j = 1, 2,..., N, for the approximate subspace V^h. The direct approximation of the penalized variational problem (2.20) is to find $\mathbf{u}_h^\epsilon \in V^h$ satisfying the initial condition with $\mathbf{u}_h^\epsilon = \mathbf{u}_w$ on $\partial\Omega_1$ such that

$$\begin{aligned} \int_{\Omega_h} (\frac{\partial \mathbf{u}_h^\epsilon}{\partial t} \cdot \mathbf{v}_h \;+\; \nu \nabla \mathbf{u}_h^\epsilon : \nabla \mathbf{v}_h \;+\; (\mathbf{u}_h^\epsilon \cdot \nabla)\mathbf{u}_h^\epsilon \cdot \mathbf{v}_h)\, d\Omega \\ + \frac{1}{\epsilon}\mathbf{I}(\nabla \cdot \mathbf{u}_h^\epsilon)(\nabla \cdot \mathbf{v}_h)\, d\Omega \\ = \int_{\Omega_h} (\mathbf{q} + \mathbf{f}(T_h, \mathbf{c}_h)) \cdot \mathbf{v}_h\, d\Omega + \int_{\partial\Omega_{2h}} \mathbf{\Gamma}(T_h, \mathbf{c}_h) \cdot \mathbf{v}_h\, dl \end{aligned} \tag{2.22}$$

for all $\mathbf{v}_h \in V^h$, where $\mathbf{I}$ denotes reduced numerical integration. If the penalty term in (2.22) is integrated exactly then the method will not yield solutions $\mathbf{u}_h^\epsilon$ that converge to $\mathbf{u}_h$ as $\epsilon \to 0$. The velocity field $\mathbf{u}_h^\epsilon \to 0$ as $\epsilon \to 0$ and the constraint equation $\nabla \cdot \mathbf{u} = 0$ dominates in this limit. The finite element solution fails the "consistency condition" or the "LBB condition" and is said to "lock" [see, e.g., [81], [55], [50]]. The second term is associated with the investigations of Ladyzhenskaya [53], Babuška and Aziz [2] and Brezzi [10]. The "LBB condition" dictates how to choose compatible interpolations for velocities and pressure when using penalty or mixed formulations. To obtain an approximate solution other than the "locking" solution, we use reduced integration for evaluating the penalty integral.

The penalty term is approximately integrated using a Gauss quadrature rule of lower order than that required for exact integration. The selective reduced integration guarantee consistency of the implied pressure field approximation and the velocity approximation. In the numerical studies we consider two special cases, continuous piecewise bilinear basis for the 4-node bilinear quadrilateral with one-point Gauss quadrature rule for the penalty term and continuous piecewise biquadratic basis for the 9-node biquadratic quadrilateral with (2×2) Gauss quadrature rule for the penalty term, which can be projected to suppress the spurious mode if the pressure approximation is desired. In the present work, we are only interested in the velocity solution and the associated coupled transport processes.

Introducing the discretization of elements and the basis functions, the velocities are

$$u_{hl}^\epsilon(x,y) = \sum_{j=1}^{N} u_j^l \, \phi_j(x,y), \tag{2.23}$$

where l is the velocity component index ($l = 1, 2$ for 2D flow) and $\mathbf{u}^l$ is the nodal vector. Using $\mathbf{v}_h = (\phi_i, 0)$ and $(0, \phi_i)$ at an interior node i, we have the following non-linear semidiscrete system of ordinary differential equations

$$\mathcal{M}\frac{d\mathbf{U}}{dt} + \nu\mathcal{A}\mathbf{U} + \mathcal{D}(\mathbf{U}) + \frac{1}{\epsilon}\mathcal{B}\mathbf{U} = \mathcal{F}(\mathbf{T}, \mathbf{C}) \tag{2.24}$$

where $\mathbf{U} = (\mathbf{u}^1, \mathbf{u}^2)^T$ and

$$\mathcal{M} = \begin{bmatrix} \mathbf{M} & \mathbf{0} \\ \mathbf{0} & \mathbf{M} \end{bmatrix} \quad \mathcal{A} = \begin{bmatrix} \mathbf{A} & \mathbf{0} \\ \mathbf{0} & \mathbf{A} \end{bmatrix} \quad \mathcal{B} = \begin{bmatrix} \mathbf{B}_x & \mathbf{B}_{xy} \\ \mathbf{B}_{xy}^T & \mathbf{B}_y \end{bmatrix} \quad \mathcal{F} = \begin{bmatrix} \mathbf{F}_x \\ \mathbf{F}_y \end{bmatrix}$$

with

$$\mathbf{M} = [m_{ij}]; \qquad m_{ij} = \int_{\Omega_h} \phi_i \phi_j \, d\Omega \tag{2.25}$$

$$\mathbf{A} = [a_{ij}]; \qquad a_{ij} = \int_{\Omega_h} ((\phi_i)_{,x}(\phi_j)_{,x} + (\phi_i)_{,y}(\phi_j)_{,y}) \, d\Omega \tag{2.26}$$

$$\mathbf{B_x} = [(b_x)_{ij}]; \qquad (b_x)_{ij} = \int_{\Omega_h} (\phi_i)_{,x}(\phi_j)_{,x} \, d\Omega \tag{2.27}$$

$$\mathbf{B_{xy}} = [(b_{xy})_{ij}]; \qquad (b_{xy})_{ij} = \int_{\Omega_h} (\phi_i)_{,x}(\phi_j)_{,y} \, d\Omega \tag{2.28}$$

$$\mathbf{B_y} = [(b_y)_{ij}]; \qquad (b_y)_{ij} = \int_{\Omega_h} (\phi_i)_{,y}(\phi_j)_{,y} \, d\Omega \tag{2.29}$$

$$\mathbf{F_x} = [(f_x)_i]; \qquad (f_x)_i = \int_{\Omega_h} (q_1 + f_1(T_h, \mathbf{c}_h)) \, \phi_i \, d\Omega + \int_{\partial\Omega_{2h}} \Gamma_1(T_h, \mathbf{c}_h) \, \phi_i \, dl \tag{2.30}$$

$$\mathbf{F_y} = [(f_y)_i]; \qquad (f_y)_i = \int_{\Omega_h} (q_2 + f_2(T_h, \mathbf{c}_h)) \, \phi_i \, d\Omega + \int_{\partial\Omega_{2h}} \Gamma_2(T_h, \mathbf{c}_h) \, \phi_i \, dl \tag{2.31}$$

$$\mathcal{D}(\mathbf{U}) = \int_{\Omega_h} (\mathbf{u}_h^\epsilon \cdot \nabla)\mathbf{u}_h^\epsilon \cdot \mathbf{v}_h \, d\Omega. \tag{2.32}$$

Here, the nonlinearity in the convective term $\mathcal{D}(\mathbf{U})$ is linearized by successive approximations [16] according to the approximation

$$\mathcal{D}(\mathbf{U}) \approx \mathcal{D}(\mathbf{U}_{k-1})\mathbf{U}_k = \int_{\Omega_h} (\mathbf{u}_{h,k-1}^\epsilon \cdot \nabla)\mathbf{u}_{h,k}^\epsilon \cdot \mathbf{v}_h \, d\Omega \tag{2.33}$$

with initial iterates given by the solution at the previous step. To decouple the flow and transport equations, we evaluate $\mathbf{f} = \mathbf{f}(\mathbf{T}, \mathbf{C})$ at $\mathbf{T}^{n-1}$ and $\mathbf{C}^{n-1}$, i.e., at the previous temperature and species concentration solutions. Substituting (2.33) into (2.24), we obtain a sequence of linear problems for $\mathbf{U}_k$ at iterate k. Given $\mathbf{U}_0$, for $k = 1, 2, \ldots$, solve

$$\mathcal{M}\frac{d\mathbf{U}_k}{dt} + (\nu\mathcal{A} + \mathcal{D} + \frac{1}{\epsilon}\mathcal{B})\mathbf{U}_k = \mathcal{F}(\mathbf{T}^{n-1}, \mathbf{C}^{n-1}) \tag{2.34}$$

with

$$\mathcal{D} = \begin{bmatrix} \mathbf{D} & \mathbf{0} \\ \mathbf{0} & \mathbf{D} \end{bmatrix}, \quad d_{ij} = \int_{\Omega_h} \mathbf{U}_{k-1} \cdot \nabla\phi_j \, \phi_i \, d\Omega \tag{2.35}$$

until

$$\frac{||\mathbf{U}_k - \mathbf{U}_{k-1}||}{||\mathbf{U}_k||} < \tau_{sa} \quad \text{or} \quad k > ksa_{max} \tag{2.36}$$

where τ_{sa} is an input tolerance and ksa_{max} is the maximum number of successive iterations allowed. To advance the solution from a specified initial state, we integrate

implicitly using a standard θ method, so that at timestep t_n:

$$\begin{aligned}\frac{\mathcal{M}(\mathbf{U}_k^n - \mathbf{U}_k^{n-1})}{\Delta t} &+ \theta\left[\nu\mathcal{A} + \mathcal{D} + \frac{1}{\epsilon}\mathcal{B}\right]\mathbf{U}_k^n \\ &+ (1-\theta)\left[\nu\mathcal{A} + \mathcal{D} + \frac{1}{\epsilon}\mathcal{B}\right]\mathbf{U}_k^{n-1} \\ &= \theta\mathcal{F}^n + (1-\theta)\mathcal{F}^{n-1} \end{aligned} \tag{2.37}$$

Here $\theta = 1/2$ which corresponds to the familiar Crank-Nicolson integrator, and $\mathcal{F}^n = \mathbf{q}^n + \mathbf{f}$ where $\mathbf{f} = \mathbf{f}(\mathbf{T}^{n-1}, \mathbf{C}^{n-1})$. Hence, in each successive approximation within each timestep we have to solve linear systems of the form

$$\mathcal{P}\mathbf{U}_k^n = \mathcal{Q} \tag{2.38}$$

where

$$\mathcal{P} = \mathcal{M} + \frac{\triangle t}{2}(\nu\mathcal{A} + \mathcal{D} + \frac{1}{\epsilon}\mathcal{B}) \tag{2.39}$$

$$\mathcal{Q} = (\mathcal{M} - \frac{\triangle t}{2}(\nu\mathcal{A} + \mathcal{D} + \frac{1}{\epsilon}\mathcal{B}))\,\mathbf{U}_k^{n-1} + \frac{\triangle t}{2}(\mathcal{F}^n + \mathcal{F}^{n-1}) \tag{2.40}$$

and n denotes the time index. Solutions of the resulting linear systems are obtained using a direct frontal solver [46]. In the next section we present the SUPG (Streamline-Upwind/Petrov-Galerkin) finite element formulation used to find approximate solutions for the transport component c_s. Since the SUPG finite element formulation for the heat equation is analogous to the SUPG formulation for the transport equation, we are not going to repeat the formulation for the temperature.

2.3 SUPG Formulation for the Transport Equations

For the transport equations, we use a SUPG (Streamline-Upwind/Petrov-Galerkin) stabilization technique [11, 23] to prevent spurious oscillation generated by the dominance of the advection terms in the differential equation. For simplicity, we show the finite element formulation for the mass transfer equation of a single species c_s. The same procedure may be used to obtain the SUPG formulation for the energy transport equation (2.9).

Consider a finite element discretization of the domain Ω into a union Ω_h of subdomains (elements) Ω_e, $e = 1, 2, \ldots,$ E. Based on this discretization, we define the finite element function spaces S^h and W^h for the concentration corresponding

to the trial solutions and weighting functions, respectively. The SUPG weighted residual formulation for the transport component c_{hs} is

$$\int_{\Omega_h} \left(w_h \, (\frac{\partial c_{hs}}{\partial t} + u_{hi} \, \frac{\partial c_{hs}}{\partial x_i}) + \frac{\partial w_h}{\partial x_i} \, k_{ij}^s \, \frac{\partial c_{hs}}{\partial x_j} - w_h \, h_{2s}(T_h, \mathbf{c}_h) \right) \, d\Omega$$

$$+ \sum_{e=1}^{E} \int_{\Omega_e} \tau \frac{u_{hm}}{||\mathbf{u}_h||} \frac{\partial w_h}{\partial x_m} \left(\frac{\partial c_{hs}}{\partial t} + u_{hi} \frac{\partial c_{hs}}{\partial x_i} - \frac{\partial}{\partial x_i} \, (k_{ij}^s \, \frac{\partial c_{hs}}{\partial x_j}) - h_{2s}(T_h, \mathbf{c}_h) \right) \, d\Omega$$

$$= \int_{\partial \Omega_{6h}} w_h \, (\gamma \, c_{hs} - \Psi_s) \, dl \tag{2.41}$$

where the first integral represents the Galerkin formulation of the problem, the second integral is the SUPG stabilization term added to the variational formulation, the last integral is due to the mixed boundary condition (2.19). We assume that $\mathbf{k}^{s_1 s_2} \neq \mathbf{0}$ only for $s_1 = s_2 = s$, $s = 1, 2, \cdots, n_s$, where $\mathbf{k}^s = \{k_{ij}^s\}$, $i, j = 1, 2$, is the diffusion tensor for species component s. The parameter τ is computed as suggested by Codina, Oñate and Cervera in [23],

$$\tau = \frac{\alpha \tilde{h}}{2}, \tag{2.42}$$

$$\alpha = \min(\frac{Pe}{3}, 1), \quad \tilde{h} = \sqrt{2A}, \tag{2.43}$$

$$Pe = \frac{||\mathbf{u}_h|| \tilde{h}}{2\tilde{k}}, \qquad \tilde{k} = \frac{\mathbf{u}_h^T}{||\mathbf{u}_h||} \mathbf{k}^s \frac{\mathbf{u}_h}{||\mathbf{u}_h||}, \tag{2.44}$$

where A is defined as the element area, $\tilde{h}$ is the element characteristic length, $\mathbf{u}_h$ is the velocity vector and Pe is the local (element) Peclet number. Introducing the finite element discretization, the transport component c_{hs} has the form

$$c_{hs}(x, y) = \sum_{j=1}^{N} c_j^s \, \psi_j(x, y), \tag{2.45}$$

where s is the species component index ($s = 1, 2, \ldots, n_s$) and $\mathbf{c}^s = \{c_j^s\}$, $j = 1, 2, \cdots, N$, is the nodal vector. We have in this study continuous piecewise basis functions defined by the 4-node bilinear quadrilateral, the 9-node biquadratic quadrilateral and the 6-node quadratic triangle.

Introducing (2.45) into (2.41) and setting $w_h = \psi_i$, $i = 1, 2, \ldots, N$, we have the resulting semi-discrete ODE system

$$\mathcal{N} \frac{d\mathbf{C}}{dt} + \mathcal{R}(\mathbf{U}) \, \mathbf{C} + \mathcal{E} \, \mathbf{C} = \mathcal{H}(\mathbf{T}, \mathbf{C}) \tag{2.46}$$

where $\mathbf{C} = (\mathbf{c}^1, \mathbf{c}^2, \ldots, \mathbf{c}^{n_s})^T$,

$$\mathcal{N} = \begin{bmatrix} \mathbf{N} & \mathbf{0} & \cdots & \mathbf{0} \\ \mathbf{0} & \mathbf{N} & \cdots & \mathbf{0} \\ \vdots & \vdots & \ddots & \vdots \\ \mathbf{0} & \mathbf{0} & \cdots & \mathbf{N} \end{bmatrix}_{n_s \times n_s} \quad \mathcal{R} = \begin{bmatrix} \mathbf{R} & \mathbf{0} & \cdots & \mathbf{0} \\ \mathbf{0} & \mathbf{R} & \cdots & \mathbf{0} \\ \vdots & \vdots & \ddots & \vdots \\ \mathbf{0} & \mathbf{0} & \cdots & \mathbf{R} \end{bmatrix}_{n_s \times n_s} \quad \mathcal{E} = \begin{bmatrix} \mathbf{E} & \mathbf{0} & \cdots & \mathbf{0} \\ \mathbf{0} & \mathbf{E} & \cdots & \mathbf{0} \\ \vdots & \vdots & \ddots & \vdots \\ \mathbf{0} & \mathbf{0} & \cdots & \mathbf{E} \end{bmatrix}_{n_s \times n_s}$$

and

$$\mathcal{H} = \begin{bmatrix} \mathbf{H}_1 \\ \mathbf{H}_2 \\ \vdots \\ \mathbf{H}_{n_s} \end{bmatrix}$$

with

$$\mathbf{N} = [n_{ij}]; \quad n_{ij} = \int_{\Omega_h} \psi_i \psi_j \, d\Omega + \int_{\Omega_h} \tau \frac{\mathbf{u}_h}{||\mathbf{u}_h||} \cdot \nabla \psi_i \psi_j \, d\Omega \tag{2.47}$$

$$\mathbf{R} = [r_{ij}]; \quad r_{ij} = \int_{\Omega_h} \mathbf{u}_h \cdot \nabla \psi_j \psi_i \, d\Omega + \int_{\Omega_h} \frac{\tau}{||\mathbf{u}_h||} \nabla \psi_i^T \mathbf{u}_h \otimes \mathbf{u}_h \nabla \psi_j \, d\Omega \tag{2.48}$$

$$\mathbf{E} = [e_{ij}]; \quad e_{ij} = \int_{\Omega_h} k_{ij}^s \nabla \psi_i \cdot \nabla \psi_j \, d\Omega + \int_{\partial \Omega_{6h}} \gamma \, \psi_i \psi_j \, dl \tag{2.49}$$

$$\mathbf{H}_s = [(h_s)_i]; \quad (h_s)_i = \int_{\Omega_h} h_{2s}(\mathbf{T}_h, \mathbf{C}_h) \, \psi_i \, d\Omega + \int_{\partial \Omega_{6h}} \Psi_s \, \psi_i \, dl + \int_{\Omega_h} \tau \frac{\mathbf{u}_h}{||\mathbf{u}_h||} \cdot \nabla \psi_i \, h_{2s}(\mathbf{T}_h, \mathbf{C}_h) \, d\Omega \tag{2.50}$$

where $\otimes$ denotes the tensor outer product $\mathbf{u}\,\mathbf{u}^T$. The streamline upwind function does not affect the weighting of the diffusion term in (2.41) because we have bilinear shape functions. We have

$$\int_{\Omega_e} \tau \frac{\mathbf{u}_h}{||\mathbf{u}_h||} \cdot \nabla \psi_j \; k_{ij}^s \nabla^2 \psi_i \, d\Omega = 0 \tag{2.51}$$

since, on the interior of each element, $\psi_{,ii}$ is zero. In the numerical experiments where the SUPG stabilization term is needed, we use only bilinear elements and the element domains are rectangular. When the element domains are not rectangular, $\psi_{,ii}$ will not in general vanish identically, and thus the term (2.51) may be not zero. However, for reasonable element shapes, this streamline upwind contribution will be small and can be neglected. This is not the case for higher-order elements.

We integrate the ODE system of equations (2.46) implicitly using a standard θ method with $\theta = 1/2$, which corresponds to the familiar Crank-Nicolson method. At timestep t_n, we have to solve

$$\begin{aligned} \frac{\mathcal{N}(\mathbf{C}^n - \mathbf{C}^{n-1})}{\Delta t} &+ \theta \left[\mathcal{R}(\mathbf{U}^n) + \mathcal{E}\right] \mathbf{C}^n \\ &+ (1-\theta) \left[\mathcal{R}(\mathbf{U}^{n-1}) + \mathcal{E}\right] \mathbf{C}^{n-1} \\ &= \theta \, \mathcal{H}^n + (1-\theta) \, \mathcal{H}^{n-1} \end{aligned} \tag{2.52}$$

Since the reaction term $\mathcal{H}$ is a nonlinear function of the unknown species solution,

we have to solve at each timestep a nonlinear system of the form

$$\mathcal{L}\left(\mathbf{C}^n\right) = 0 \tag{2.53}$$

where

$$\mathcal{L}\left(\mathbf{C}^n\right) = \left(\mathcal{N} + \frac{\triangle t}{2}\left(\mathcal{R}(\mathbf{U}^n) + \mathcal{E}\right)\right)\mathbf{C}^n \; - \; \frac{\triangle t}{2}\,\mathcal{H}^n \; + \; \mathcal{I} \tag{2.54}$$

with

$$\mathcal{I} = -\left(\mathcal{N} - \frac{\triangle t}{2}\left(\mathcal{R}(\mathbf{U}^{n-1}) + \mathcal{E}\right)\right)\mathbf{C}^{n-1} \; - \; \frac{\triangle t}{2}\,\mathcal{H}^{n-1} \tag{2.55}$$

and n denotes the timestep index. The nonlinear system (2.53) is solved by Newton's method in the present study. Given $\mathbf{C}_0^n$, $\mathbf{U}^{n-1}$ and $\mathbf{U}^n$, at each timestep and $k = 1, 2, \ldots$, solve linear systems of the form

$$\mathcal{J}(\mathbf{C}_k^n \; - \; \mathbf{C}_{k-1}^n) = -\,\mathcal{V} \tag{2.56}$$

with

$$\mathcal{J} = \left(\mathcal{N} + \frac{\triangle t}{2}\left(\mathcal{R}(\mathbf{U}^n) + \mathcal{E}\right)\right) \; - \; \frac{\triangle t}{2}\,\frac{\partial \mathcal{H}_{k-1}^n}{\partial \mathbf{C}^n} \tag{2.57}$$

and

$$\mathcal{V} = \left(\mathcal{N} + \frac{\triangle t}{2}\left(\mathcal{R}(\mathbf{U}^n) + \mathcal{E}\right)\right)\mathbf{C}_{k-1}^n \; - \; \frac{\triangle t}{2}\,\mathcal{H}_{k-1}^n \; + \; \mathcal{I} \tag{2.58}$$

where $\mathcal{I}$ is defined in (2.55) and $\mathcal{H}_{k-1}^n = \mathcal{H}(\mathbf{T}_{k-1}^n, \mathbf{C}_{k-1}^n)$. Here the solution of the linear systems (2.56) are also obtained using a direct frontal solver [46]. In the next section the main algorithm to calculate approximate solutions for the velocity field, temperature and concentration vector is constructed. We also present the Navier-Stokes and transport algorithms in detail.

2.4 Decoupled Algorithm

In the present work, we consider a decoupled formulation to solve the class of coupled problems of interest. In this approach, the momentum and continuity equations are solved first, in each timestep or iteration, lagging the temperature and concentration vector in the forcing term. Then, the transport equations are solved with the computed velocities as input.

The solution algorithm is obtained by simply 'lagging' the temperature and concentration vector $\mathbf{c}_h$ on the right hand side of (2.24). That is, for iterate $n = 1$, $2, \cdots$ we set $\mathbf{T}_h = \mathbf{T}_h^{n-1}$ and $\mathbf{c}_h = \mathbf{c}_h^{n-1}$ in (2.24). This decouples the flow and transport equations within each global iteration. Our algorithm to calculate approximate solutions for the velocity field and concentration vector as time progress

may be summarized by the steps in Figure 2.1. Here $\mathbf{U}^0$, $\mathbf{T}^0$ and $\mathbf{C}^0$ are the initial approximations for the velocity field, temperature and concentration vector, respectively. The timestep size $\triangle t$ is initialized with $(\triangle t)_{min}$ and is chosen adaptively using the control algorithms discussed in the next chapter. If the steady-state solution is needed, we stop the calculations when the nondimensional kinetic energy K at two different timesteps reaches a difference less than an input tolerance, that is,

$$|K^n - K^{n-1}| < \tau_K \, |K^n|, \qquad K = \int_\Omega \frac{(u^{*2} + v^{*2})}{2} \, d\Omega \tag{2.59}$$

or when the approximate solutions at two different timesteps reaches a difference less than input tolerances,

$$\|\mathbf{U}^n - \mathbf{U}^{n-1}\| < \tau_u \, \|\mathbf{U}^n\|, \;\; \|\mathbf{T}^n - \mathbf{T}^{n-1}\| < \tau_T \, \|\mathbf{T}^n\|, \;\; \|\mathbf{C}^n - \mathbf{C}^{n-1}\| < \tau_c \, \|\mathbf{C}^n\| \tag{2.60}$$

where n denotes the timestep index, $\|\cdot\|$ denotes Euclidean norm, u^* and v^* are the nondimensional velocity components, and τ_K, τ_u, τ_T and τ_c are input tolerances.

1. Input data: $\mathbf{U}^0$, $\mathbf{T}^0$, $\mathbf{C}^0$, t_{max}, $(\triangle t)_{min}$
2. Initialize variables: $n \leftarrow 1$, $t_0 \leftarrow 0$, $\triangle t \leftarrow (\triangle t)_{min}$
3. Repeat
   - (a) $t_n \leftarrow t_{n-1} + \triangle t$
   - (b) Calculate the solutions $\mathbf{U}^n$, $\mathbf{T}^n$, $\mathbf{C}^n$
   - (c) If $(n > 1)$ calculate the new $\triangle t$ using a timestep selection algorithm
   - (d) Update solutions: $\mathbf{U}^{n-1} \leftarrow \mathbf{U}^n$, $\mathbf{T}^{n-1} \leftarrow \mathbf{T}^n$, $\mathbf{C}^{n-1} \leftarrow \mathbf{C}^n$
   - (e) $n \leftarrow n + 1$

   until $(t_n > t_{max})$

Figure 2.1: Main Algorithm

In step 3(b) of Figure 2.1, we have to calculate the approximated solution $\mathbf{U}^n$ for the velocity field at time t_n. Figure 2.2 shows the algorithm to obtain $\mathbf{U}^n$ given $\mathbf{U}^{n-1}$, $\mathbf{T}^{n-1}$, $\mathbf{C}^{n-1}$, nsa_{max} and τ_{sa}. The successive approximation process used to linearize the non-linear semidiscrete system of ordinary differential equations (2.24) is described in step 4 of the algorithm given in Figure 2.2. This process is interrupted when the condition in step 4(d) is achieved or the number of successive iterations exceeds a maximum given value nsa_{max}. We consider the maximum number of

successive approximations allowed equal to $nsa_{max} = 10$. At each timestep, the total number of successive approximations calculated is given by nsa in step 5.

To calculate an approximate solution for the concentration vector $\mathbf{C}^n$ in step 3(b) of Figure 2.1, we have to use equations (2.56), (2.57), (2.58) and (2.55). The transport algorithm may be summarized by the steps in Figure 2.3, and an analogous algorithm can be used to calculate the temperature. If the nonlinear reaction source or sink term in the transport equation (2.6) is a linear function of the concentration vector or is zero, the approximate solution $\mathbf{C}^n$ is obtained with only two iterations in step 4 of Figure 2.3. Here, $kn_{max} = 10$ is the maximum number of Newton iterations allowed.

To complete our main algorithm given in Figure 2.1, we have to specify how the stepsize is adaptively calculated in step 3(c). In the next chapter we discuss in details the control algorithms for the timestep selection we are using in this work and also the approach used by Winget and Hughes in [79].

1. Input data: $\mathbf{U}^{n-1}$, $\mathbf{T}^{n-1}$, $\mathbf{C}^{n-1}$, nsa_{max}, τ_{sa}.

2. Initialize variables: $k \leftarrow 1$, $\mathbf{U}_0^n \leftarrow \mathbf{U}^{n-1}$

3. Calculate $\mathcal{M}$, $\mathcal{A}$, $\mathcal{D}$, $\mathcal{B}$, $\mathcal{F}^n$, $\mathcal{F}^{n-1}$ using (2.25)-(2.31), (2.35).

4. Repeat

   (a) Set $\mathbf{U}_{k-1} \leftarrow \mathbf{U}_{k-1}^n$ in (2.35) and calculate $\mathcal{D}$.

   (b) Set $\mathbf{U}_k^{n-1} \leftarrow \mathbf{U}^{n-1}$, calculate $\mathcal{P}$, $\mathcal{Q}$ using (2.39), (2.40).

   (c) Solve the linear system (2.38) to obtain $\mathbf{U}_k^n$.

   (d) Calculate $cond \leftarrow \frac{||\mathbf{U}_k^n - \mathbf{U}_{k-1}^n||}{||\mathbf{U}_k^n||}$

   (e) Update solution: $\mathbf{U}_{k-1}^n \leftarrow \mathbf{U}_k^n$

   (f) $k \leftarrow k+1$

   until $(k > nsa_{max})$ or $(cond < \tau_{sa})$

5. Set $\mathbf{U}^n \leftarrow \mathbf{U}_k^n$ and $nsa \leftarrow k-1$

Figure 2.2: Navier-Stokes Algorithm

1. Input data: $\mathbf{C}^{n-1}$, $\mathbf{U}^{n-1}$, $\mathbf{U}^n$, kn_{max}, τ_n.

2. Initialize variables: $k \leftarrow 1$, $\mathbf{C}_0^n \leftarrow \mathbf{C}^{n-1}$

3. Calculate $\mathcal{I}$ in (2.55).

4. Repeat

   (a) Calculate $\mathcal{J}$ and $\mathcal{V}$ using (2.57) and (2.58).

   (b) Solve the linear system (2.56) to obtain $\mathbf{C}_k^n$.

   (c) Calculate $cond \leftarrow \frac{||\mathbf{C}_k^n - \mathbf{C}_{k-1}^n||}{||\mathbf{C}_k^n||}$

   (d) Update solution: $\mathbf{C}_{k-1}^n \leftarrow \mathbf{C}_k^n$

   (e) $k \leftarrow k+1$

   until $(k > kn_{max})$ or $(cond < \tau_n)$

5. Set $\mathbf{C}^n \leftarrow \mathbf{C}_k^n$

Figure 2.3: Transport Algorithm

Chapter 3

Control Algorithms

The objective here is to discuss timestep control algorithms developed to improve efficiency of codes to solve coupled problems. The outline of this chapter is the following. In the first section, we present our PID control algorithm for timestep selection based on controlling accuracy. Then, we discuss the control algorithm used when the stepsize is limited by the convergence rate of nonlinear iterations. Next, we describe the two control strategies for timestep selection in simulation of transient coupled flow and heat and mass transfer problems. Finally, we present the algorithm for timestep selection suggested by Winget and Hughes in [79], used here for comparative purposes.

3.1 PID Stepsize Control Algorithm

Control can be defined as the process of making a system of variables follow a particular value, called the reference value. Closed-loop process control uses a measurement of the controlled variable and feedback of this signal to compare it with a reference value. The feedback is supplied from an output sensor of some sort, and feeds an input of the controller to tell the controller how far the output is from its reference value. The controller uses this information to correct the output error. This kind of process is used in applications ranging, for example, from air conditioning thermostats to guidance and control of aircraft.

A simple feedback system consists of an actuator, a control device often called the controller, the process (or plant), and an output sensor, as shown in Figure 3.1. The central component of a feedback control system is the process, whose output is to be controlled. In our case we are interested in process control. The difference between the desired output and the actual output of the system measured by an sensor is equal to the error, which is adjusted by the controller. The actuator is the

device that can influence the controlled variable of the process. The output of the control device causes the actuator to modulate the process in order to reduce the error.

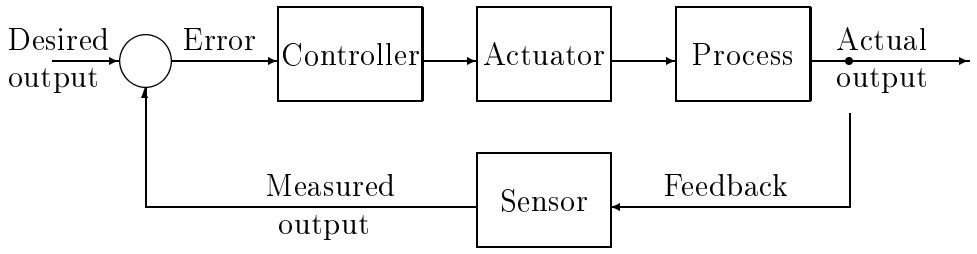

Figure 3.1: A feedback system block diagram of a basic closed-loop control system

One example of a feedback control system is the room-temperature control system of a house [36]. The process is the house, the thermostat is the output sensor, the gas valve is the controller, and the furnace is the actuator. Suppose the thermostat is turned on when both the temperature in the house and the outside temperature are below the reference temperature. The gas valve will be open causing the furnace to fire and heat to be supplied to the house. This is a closed loop system.

One of the most widely used algorithms for closed-loop control is the three-term control, known as the Proportional-Integral-Differential (PID) control loop. The popularity of PID controllers can be attributed to their functional simplicity and to their robust performance in a large range of operating conditions. The objective in using PID control algorithms is to control the output along a smooth curve (vs. time) toward the set-point while minimizing overshoot, that is, the amount the system output response proceeds beyond the desire response.

A PID control algorithm includes a term which is proportional (P) to the output error, a term proportional to the integral (I) of the error, and a term proportional to the derivative (D) of the error, and therefore has the form

$$-S(\tau) = k\left\{\theta(\tau) + \frac{1}{T_I}\int_0^{\tau}\theta(\tilde{\tau})d\tilde{\tau} + T_D\frac{d\theta(\tau)}{d\tau}\right\} \tag{3.1}$$

or

$$-\dot{S}(\tau) = k_P\dot{\theta}(\tau) + k_I\theta(\tau) + k_D\ddot{\theta}(\tau) \tag{3.2}$$

where $S(\tau)$ is the controller output deviation, $\dot{S}(\tau)$ implies time rate of change of S, $\theta(\tau)$ is the error, k is the proportional gain, T_I is called the integral or reset time, T_D is the derivative time, and k_P, k_I and k_D are the proportional, integral and

derivative parameters, respectively. In order to adapt the continuous-time model to a discrete environment, we replace derivatives by differences in (3.2) to obtain:

$$-(S_{n+1} - S_n) = k_P\,(\theta_n - \theta_{n-1}) + k_I\,\theta_n + k_D\,(\theta_n - 2\theta_{n-1} + \theta_{n-2}) \tag{3.3}$$

The proportional term acts like a rubber band in an analogous mechanical system: it exerts a restoring force proportional to how much the rubber band is stretched from its original shape. The proportional term can reduce error responses to disturbances as we adjust k_D up or down. The integral term is added to reduce or eliminate constant steady state errors. It can do this because it sums up errors over time. The derivative feedback is used in conjunction with proportional and/or integral feedback to increase the damping of the dynamic response. In general, it also improves the stability of the system. These three kinds of control attempt to provide a good degree of error reduction simultaneously with acceptable stability and damping [32, 52, 36].

Designing a particular PID control loop requires merely tuning the controller. The constants k_P, k_I, and k_D have to be adjust to yield satisfactory control. Increasing k_P and k_I tends to reduce system errors but may lead to instability, while increasing k_D tends to improve stability. The selection of the parameters is basically a search in a three-dimensional space. There are several methods and rules proposed to solve this parameter selection problem. Dorf and Bishop, [32], for instance, show many design methods using root loci and performance indexes.

In the numerical integration of ordinary differential equations, automatic stepsize control is probably the most important means to improve efficiency of a given integration method. Most timestep schemes are based on controlling accuracy as determined by truncation error estimates (e.g. Prediction-Modification-Correction). The objective of timestep selection is minimize the computational effort to construct an approximate solution of a given problem in accordance with a desired accuracy. This strategy is motivated by the fact that the global error can be bounded in terms of the local truncation error per unit step [51, 59, 9, 37, 60].

In general, a typical stepsize control algorithm for integration methods, such as explicit Runge-Kutta methods of order $p-1$, can be expressed as

$$\triangle t_{n+1} = \left(\frac{tol}{e_n}\right)^{1/p} \triangle t_n \tag{3.4}$$

where *tol* is some input tolerance and e_n is an estimate of the local truncation error in timestep $\triangle t_n$. If the error is too big in one step, then the step is rejected and

re-calculated with a new step. One standard stepsize control algorithm of this type can be found in [39]. This kind of algorithm normally performs quite well. However, there are differential equations and integration methods for which its performance is unacceptable. The stepsize oscillates tremendously and the number of rejected steps is too high. As a consequence, much computation time is spent re-calculating rejected steps and changing the stepsize.

Gustafsson, Lind and Söderlind [39] showed that the above problem (3.4) can be viewed as a standard automatic control problem. Equation (3.4) can be rewritten as

$$-\left(\log \triangle t_{n+1} - \log \triangle t_n\right) = \frac{1}{p}\left(\log e_n - \log tol\right) \tag{3.5}$$

or

$$-(S_{n+1} - S_n) = k_I\, \theta_n \tag{3.6}$$

where

$$S_n = \log \triangle t_n \tag{3.7}$$

$$\theta_n = \log e_n - \log tol \tag{3.8}$$

Equation (3.6) is equivalent to equation (3.3) if we take $k_P = 0$, $k_I = 1/p$ and $k_D = 0$. Thus, the stepsize control schemes based on the control of maximum change in key variables are nothing but versions of the standard integral feedback controller. We recognize $\log \triangle t_n$ as the control signal or control variable, the deviation $(\log e_n - \log tol)$ as the control error, $\log e_n$ as the plant output and $\log tol$ as the set point.

Figure (3.2) shows a block diagram of the feedback control problem. The process takes the timestep size $\triangle t_n$ as a input, calculates the solution of the problem, and produces an error estimate e_n that is fed back to the controller. The controller tries to select the new timestep in a such way that the quantity $\log e_n$ comes as close as possible to $\log tol$ along a smooth curve.

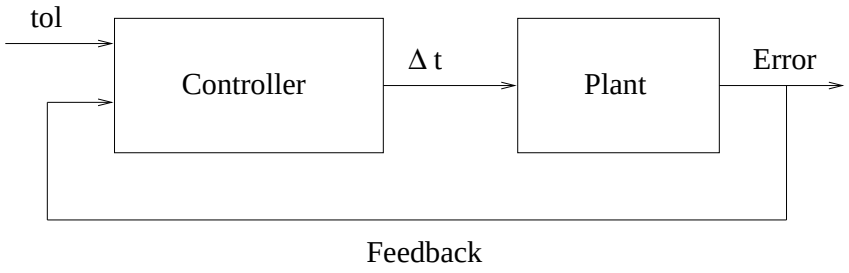

Figure 3.2: Stepsize selection viewed as a control problem.

Motivated by these ideas, Hairer and Wanner [41] design a new stepsize control algorithm using the standard discrete PID controller (3.3). Substituting the

definitions (3.7) and (3.8) into (3.3), we obtain

$$\begin{aligned} -(\log \triangle t_{n+1} - \log \triangle t_n) &= k_I(\log e_n - \log tol) + \\ & \quad k_P\left[(\log e_n - \log tol) - (\log e_{n-1} - \log tol)\right] + \\ & \quad k_D\left[(\log e_n - \log tol) - 2(\log e_{n-1} - \log tol) + \right. \\ & \quad \left. (\log e_{n-2} - \log tol)\right] \end{aligned}$$

which can be rearranged as,

$$\triangle t_{n+1} = (\frac{e_{n-1}}{e_n})^{k_P}(\frac{tol}{e_n})^{k_I}(\frac{{e_{n-1}}^2}{e_n e_{n-2}})^{k_D}\ \triangle t_n, \tag{3.9}$$

where tol is some input tolerance, e_n is the measure of the change of the quantities of interest in timestep $\triangle t_n$, and k_P, k_I and k_D are the PID parameters. Equation (3.9) can be rewritten using the normalized changes in the variables of interest, $e_n^* = e_n/tol$, $e_{n-1}^* = e_{n-1}/tol$ and $e_{n-2}^* = e_{n-2}/tol$,

$$\triangle t_{n+1} = (\frac{e_{n-1}}{e_n})^{k_P}(\frac{1}{e_n})^{k_I}(\frac{{e_{n-1}}^2}{e_n e_{n-2}})^{k_D}\ \triangle t_n. \tag{3.10}$$

where we drop the superscript * for simplicity.

Three consecutive estimates of the solution are needed to calculate the local normalized truncation errors e_{n-2}, e_{n-1} and e_n in (3.10). In the present work, we consider two different ways to define e_n. First, we may use the changes in nodal velocities, temperature and concentration vector to compute e_n taking,

$$e_n = \max(e_u, e_T, e_c) \tag{3.11}$$

where

$$e_u = \frac{e_u^*}{\mathrm{tol}_u} \qquad e_u^* = \frac{\|\mathbf{U}^n - \mathbf{U}^{n-1}\|}{\|\mathbf{U}^n\|} \tag{3.12}$$

$$e_T = \frac{e_T^*}{\mathrm{tol}_T} \qquad e_T^* = \frac{\|\mathbf{T}^n - \mathbf{T}^{n-1}\|}{\|\mathbf{T}^n\|} \tag{3.13}$$

$$e_c = \frac{e_c^*}{\mathrm{tol}_c} \qquad e_c^* = \frac{\|\mathbf{C}^n - \mathbf{C}^{n-1}\|}{\|\mathbf{C}^n\|} \tag{3.14}$$

where tol_u, tol_T and tol_c are user supplied tolerances corresponding to the normalized changes in velocities, temperature and concentration vector, respectively. Second, we may define e_n computing changes in the nondimensional kinetic energy given by

$$K = \int_\Omega \frac{(u^{*2} + v^{*2})}{2}\, d\Omega, \tag{3.15}$$

where u^* and v^* are the nondimensional velocity components. Now e_n is defined by

$$e_n = \frac{e_K^*}{\text{tol}_K}, \qquad e_K^* = \frac{|K^n - K^{n-1}|}{|K^n|} \tag{3.16}$$

where tol_K is a given tolerance. The nondimensional kinetic energy is also a suitable parameter for monitoring the behavior of the fluid and for constructing bifurcation diagrams. Here we also use the kinetic energy to obtain the steady-state solution.

The algorithm for controlling the timestep has two main parts. First, a step size is assumed, and using the newly computed solution, an *a posteriori* estimate is made of the error in the step. Second, this error measure is used to accept or reject the solution and modify the timestep accordingly. If the error is unacceptable, the new solution is discarded and we restart the time integration in the previous step with a reduced step size. If the error is acceptable, a new timestep is calculated using equation (3.9) and we proceed with the time integration. Here, the size of the timestep is limited by the changes in velocities, temperature and concentrations.

The initial data for the timestep control algorithm should be: two consecutive estimates of the solution $\mathbf{U}^{n-1}$, $\mathbf{U}^n$, $\mathbf{T}^{n-1}$, $\mathbf{T}^n$, $\mathbf{C}^{n-1}$, $\mathbf{C}^n$, the current time t, the timestep size $\triangle t$, the timestep index n and the number of successive approximations nsa. We have to define the control data: the minimum timestep size $\triangle t_{min}$, the maximum timestep size $\triangle t_{max}$, the PID parameters k_P, k_I, k_D, the tolerances tol_u, tol_T, tol_c, and the maximum number of successive approximations nsa_{max}. We initialize the normalized errors, $e_{n-2} \leftarrow 1.0$ and $e_{n-1} \leftarrow 1.0$, the timestep size at the previous step, $\triangle t_n = \triangle t_{prev} \leftarrow \triangle t_{min}$, and the number of rejected timesteps, $nrej \leftarrow 0$. Our PID timestep selection algorithm to calculate the new timestep size $\triangle t_{n+1} = \triangle t$ at time $t_n = t$ may be summarize by the steps in Figure 3.3.

If a timestep gives an unacceptable value of e_n, the step is rejected. Then the step is repeated with a scaled timestep size based on the magnitude of the error relative to the tolerance. However, we find in numerical experiments that the number of rejections is very small, producing a smooth sequence of timesteps. In our algorithm, if the sequence of iterates of the nonlinear system is converging at a slow rate, the timestep is also rejected. That is, if the number of successive approximations nsa is greater than the maximum number of successive approximations allowed nsa_{max}, the step size is rejected.

In almost all systems, actuators saturate because the dynamic range of practical actuators is usually limited. Whenever control saturation happens, the integration with the PID control law has to stop or this may result in substantial overshoot.

This problem is called the windup effect [36]. So, to prevent an excessive growth or reduction of the step size $\triangle t$, we supply timestep limiters $\triangle t_{min}$ and $\triangle t_{max}$ which limit the control signal (anti-windup effect). The effect of the anti-windup is to reduce both overshoot and the control effort in the feedback system. Omission of this technique may lead to deterioration of response and even instability.

Although feedback control theory provides sophisticated techniques to choose PID parameters, robustness is required when a general finite element method is used for a wide range of different simulations. We perform parametric studies of the PID controller for values similar to those used by Gustafsson *et al.* [39] and also by Coutinho and Alves [24]. We investigate values for k_P ranging from 0.03 to 0.20, k_I from 0.03 to 0.40 and k_D from 0.003 to 0.02. Subsequent numerical experiments demonstrate that the PID controller is very robust for all the applications studied here, and that we can adopt the following parameters: $k_P = 0.075$, $k_I = 0.175$ and $k_D = 0.01$.

3.2 Convergence Rate Control Algorithm

Gustafsson and Söderlind [40] establish a model for controlling the convergence rate of the iterative method that relates the convergence rate to the stepsize. Integrating an ODE,

$$\dot{\mathbf{y}} = \mathbf{f}(\mathbf{y}) \tag{3.17}$$

by implicit time-stepping methods leads to the nonlinear equation

$$\mathbf{y} = \gamma\, h\, \mathbf{f}(\mathbf{y}) + \mathbf{\Psi} \tag{3.18}$$

where h is the stepsize, γ is a constant of moderate size, characteristic of the discretization method, and $\mathbf{\Psi}$ is a known vector. Applying a fixed-point iteration to (3.18) yields

$$\mathbf{y}_{n+1} = \gamma\, h\, \mathbf{f}(\mathbf{y}_n) + \mathbf{\Psi} \tag{3.19}$$

Let the error in the solution be denoted by $\mathbf{e}_n = \mathbf{y}_n - \mathbf{y}$. Using equations (3.18) and (3.19), and assuming that $\mathbf{J}\mathbf{e}_n = \mathbf{f}(\mathbf{y}_n) - \mathbf{f}(\mathbf{y})$ where $\mathbf{J}$ is a mean value Jacobian, we obtain

$$\mathbf{e}_{n+1} = \gamma\, h\, \mathbf{J}\, \mathbf{e}_n \tag{3.20}$$

from which it follows that

$$||\mathbf{e}_{n+1}|| \leq \gamma\, h\, ||\mathbf{J}||\, ||\mathbf{e}_n||. \tag{3.21}$$

1. Input data: $\mathtt{U}^{n-1}$, $\mathtt{U}^{n}$, $\mathtt{T}^{n-1}$, $\mathtt{T}^{n}$, $\mathtt{C}^{n-1}$, $\mathtt{C}^{n}$, t, Δt, n, nsa.

2. Control data: $\triangle t_{min}$, $\triangle t_{max}$, k_P, k_I, k_D, tol_u, tol_T, tol_c, nsa_{max}.

3. Initialize variables: $e_{n-2} \leftarrow 1.0$, $e_{n-1} \leftarrow 1.0$, $\triangle t_{prev} \leftarrow \triangle t_{min}$, $nrej \leftarrow 0$.

4. Calculate e_n using (3.11)-(3.14).

5. If (($e_n > 1.0$) or ($nsa > nsa_{max}$)) and ($\triangle t > \triangle t_{min}$) then reject the timestep:

   (a) $nrej \leftarrow nrej + 1$

   (b) $\mathtt{U}^{n} \leftarrow \mathtt{U}^{n-1}$, $\mathtt{T}^{n} \leftarrow \mathtt{T}^{n-1}$, $\mathtt{C}^{n} \leftarrow \mathtt{C}^{n-1}$

   (c) $t \leftarrow t - \triangle t$

   (d) $n \leftarrow n - 1$

   (e) $factor = \frac{1}{e_n}$

   (f) if ($factor > 0.8$) $factor = 0.8$

   (g) $\triangle t \leftarrow \mathtt{max}(factor\, \triangle t, \triangle t_{min})$

   (h) $\triangle t_{prev} \leftarrow \triangle t^2 / \triangle t_{prev}$

   else

   (i) calculate $\triangle t \leftarrow (\frac{e_{n-1}}{e_n})^{k_P} (\frac{1}{e_n})^{k_I} (\frac{{e_{n-1}}^2}{e_n\, e_{n-2}})^{k_D}\ \triangle t_{prev}$

   (j) $\triangle t \leftarrow \mathtt{max}\ (\triangle t,\ \triangle t_{min})$

   (k) $\triangle t \leftarrow \mathtt{min}\ (\triangle t,\ \triangle t_{max})$

   (l) $\triangle t_{prev} \leftarrow \triangle t$

   (m) $e_{n-2} \leftarrow e_{n-1}$, $e_{n-1} \leftarrow e_n$

   endif

Figure 3.3: PID Stepsize Control Algorithm

Hence the convergence rate depends on the stepsize h and the (unknown) Jacobian $\mathbf{J}$. The stepsize-convergence relation may be modeled by

$$\alpha = \upsilon\, h, \tag{3.22}$$

where $\upsilon \leq \gamma\, ||\mathbf{J}||$ and α is the convergence rate depending on the spectral radius of $\gamma h \mathbf{J}$. This model is confirmed by actual computations in [40] showing that the convergence rate is in practice largely (but not perfectly) proportional to h. To avoid expensive eigenvalues estimates, α is obtained by using three consecutive iterates $\mathbf{y}_{n-2}$, $\mathbf{y}_{n-1}$, and $\mathbf{y}_n$, as follows

$$\alpha = \max \alpha_n = \max_n \frac{\|\mathbf{y}_n - \mathbf{y}_{n-1}\|}{\|\mathbf{y}_{n-1} - \mathbf{y}_{n-2}\|}. \tag{3.23}$$

Assuming that the stepsize is limited by the convergence rate of nonlinear iterations and that the change in υ from step to step is small, the new stepsize should be chosen as

$$\Delta t_{n+1} = \frac{\alpha_{ref}}{\alpha}\, \Delta t_n \tag{3.24}$$

where α_{ref} is a reference rate of convergence and α is the estimated rate of convergence (3.23). Now the controller tries to keep the estimated convergence rate as close as possible of a reference value. The low quality of the estimate (3.23) of the convergence rate α together with variations in υ imply that it is usually not worthwhile trying a more sophisticated strategy than (3.24).

We must find what convergence rate α_{ref} the controller should aim for to give the most efficient integration. This question can be analyzed using the technique presented in [40]. In general, any value $0.2 < \alpha_{ref} < 0.4$ would be acceptable, and $\alpha_{ref} \approx 0.2$ gives performance near to optimal [40]. It is necessary to coordinate the convergence control algorithm (3.24) with the stepsize control strategy (3.9) so that efficiency is maintained.

3.3 The Timestep Control Algorithms

We propose two timestep control algorithms based on controlling accuracy or the convergence rate of the successive iterations. These algorithms will be used to find timestep sizes in steady-state and transient chemical reaction systems, Rayleigh-Benard-Marangoni flows and heat and mass transfer problems. The algorithms are very simple and easy to implement.

The first control uses only the PID control for timestep selection (3.9) with changes in velocities, temperature and concentrations. The **Control 1** is defined by

$$\triangle t = \left(\frac{e_{n-1}}{e_n}\right)^{k_P} \left(\frac{1}{e_n}\right)^{k_I} \left(\frac{{e_{n-1}}^2}{e_n e_{n-2}}\right)^{k_D} \triangle t_{prev} \tag{3.25}$$

with

$$e_n = \max\left(e_u, e_T, e_c\right), \tag{3.26}$$

where

$$e_u = \frac{e_u^*}{\mathrm{tol}_u} \qquad e_u^* = \frac{\|\mathbf{U}^n - \mathbf{U}^{n-1}\|}{\|\mathbf{U}^n\|} \tag{3.27}$$

$$e_T = \frac{e_T^*}{\mathrm{tol}_T} \qquad e_T^* = \frac{\|\mathbf{T}^n - \mathbf{T}^{n-1}\|}{\|\mathbf{T}^n\|} \tag{3.28}$$

$$e_c = \frac{e_c^*}{\mathrm{tol}_c} \qquad e_c^* = \frac{\|\mathbf{C}^n - \mathbf{C}^{n-1}\|}{\|\mathbf{C}^n\|} \tag{3.29}$$

and Δt represents the new timestep size and $\triangle t_{prev}$ is the timestep size at the previous step. In the second control, the size of the timestep is limited by the changes in the kinetic energy or by the rate of convergence of the successive approximations. We take the minimum between the two values. The **Control 2** is given by

$$\Delta t = \min(\Delta t_\alpha, \Delta t_r), \tag{3.30}$$

where

$$\Delta t_\alpha = \frac{\alpha_{ref}}{\alpha} \Delta t_{prev} \tag{3.31}$$

$$\triangle t_r = \left(\frac{e_{n-1}}{e_n}\right)^{k_P} \left(\frac{1}{e_n}\right)^{k_I} \left(\frac{{e_{n-1}}^2}{e_n e_{n-2}}\right)^{k_D} \triangle t_{prev} \tag{3.32}$$

with

$$e_n = \frac{e_K^*}{\mathrm{tol}_K}, \qquad e_K^* = \frac{|K^n - K^{n-1}|}{|K^n|}. \tag{3.33}$$

We should modify the algorithm given in Figure 3.3 to include both controls. We need the calculation of Δt_α in (3.31) to obtain the new timestep Δt in (3.30). The value of the estimated rate of convergence α has to be calculated at every step and passed to the PID timestep algorithm as a parameter. The reference rate of convergence α_{ref} should be a constant defined in the algorithm. **Control 1** and **Control 2** are embodied in the algorithm given in Figure 3.4. The variable *control* in the algorithm indicates if the new timestep size Δt is calculated using Control 1 or Control 2. In the next section we briefly discuss the automatic timestep selection strategy proposed by Winget and Hughes in [79].

1. Input data: $\mathtt{U}^{n-1}$, $\mathtt{U}^n$, $\mathtt{T}^{n-1}$, $\mathtt{T}^n$, $\mathtt{C}^{n-1}$, $\mathtt{C}^n$, $\mathtt{K}^{n-1}$, $\mathtt{K}^n$, t, Δt, n, α, nsa.

2. Control data: $\triangle t_{min}$, $\triangle t_{max}$, k_P, k_I, k_D, tol_u, tol_T, tol_c, tol_K, nsa_{max}, α_{ref}, $control$.

3. Initialize variables: $e_{n-2} \leftarrow 1.0$, $e_{n-1} \leftarrow 1.0$, $\triangle t_{prev} \leftarrow \triangle t_{min}$, $nrej \leftarrow 0$.

4. If $control = 1$ then
   calculate e_n using (3.26)-(3.29)
   else
   calculate e_n using (3.33).

5. If $((e_n > 1.0)$ or $(nsa > nsa_{max}))$ and $(\triangle t > \triangle t_{min})$ then
   reject the timestep:

   (a) $nrej \leftarrow nrej + 1$

   (b) $\mathtt{U}^n \leftarrow \mathtt{U}^{n-1}$, $\mathtt{T}^n \leftarrow \mathtt{T}^{n-1}$, $\mathtt{C}^n \leftarrow \mathtt{C}^{n-1}$, $K^n \leftarrow K^{n-1}$

   (c) $t \leftarrow t - \triangle t$

   (d) $n \leftarrow n - 1$

   (e) $factor = \frac{1}{e_n}$

   (f) if $(factor > 0.8)$ $factor = 0.8$

   (g) $\triangle t \leftarrow \max(factor\, \triangle t, \triangle t_{min})$

   (h) $\triangle t_{prev} \leftarrow \triangle t^2 / \triangle t_{prev}$

   else

   (i) calculate $\triangle t \leftarrow (\frac{e_{n-1}}{e_n})^{k_P} (\frac{1}{e_n})^{k_I} (\frac{{e_{n-1}}^2}{e_n\, e_{n-2}})^{k_D}\ \triangle t_{prev}$

   (j) If $control = 2$ then

   (j1) calculate Δt_α using (3.31)

   (j2) $\triangle t \leftarrow \min\ (\triangle t_\alpha,\ \triangle t)$

   (k) $\triangle t \leftarrow \max\ (\triangle t,\ \triangle t_{min})$

   (l) $\triangle t \leftarrow \min\ (\triangle t,\ \triangle t_{max})$

   (m) $\triangle t_{prev} \leftarrow \triangle t$

   (n) $e_{n-2} \leftarrow e_{n-1}$, $e_{n-1} \leftarrow e_n$

   endif

Figure 3.4: Algorithm for Control 1 and Control 2

3.4 The Winget and Hughes Approach

Winget and Hughes [79] in their work on finite element simulation of transient heat conduction develop timestep selection strategies based on heuristic rules. Errors and computational efficiency in the transient solution are controlled by this automatic timestep selection strategy. The algorithm for controlling the timestep error has two parts: *an posteriori* error estimate for the newly computed solution, and an algorithm that uses this error measure to accept or reject the solution and modify the timestep accordingly. The main ideas of the their approach are described below.

The selection of the timestep Δt is based on controlling the maximum normalized error e_n of quantities of interest with respect to user specified error tolerances. The objective is minimize this error, but at the same time keep Δt as large as possible to avoid excessive "work" in obtaining the solution for a given time interval. As long as $e_n \leq 1$ the solution satisfies the user specified error tolerances and solution error is acceptable. Observe that a very small solution error indicates that the stepsize should be increased to reduce the amount of "work" required to integrate the time interval under consideration. If the error is unacceptable, $e_n > 1$, the new solution is rejected and the time integration at the previous step is restarted with a reduced stepsize.

Thus, the selection of Δt as a function of e_n is based on the two rules: at no time should a timestep be acceptable if $e_n > 1$, and the step size Δt should be increased until $e_n = O(1)$. The initial data for the algorithm should be: two consecutive estimates of the solution $\mathbf{U}^{n-1}$, $\mathbf{U}^n$, $\mathbf{T}^{n-1}$, $\mathbf{T}^n$, $\mathbf{C}^{n-1}$, $\mathbf{C}^n$, the current time t, the timestep size $\triangle t$ and the timestep index n. We need to define the following parameters: the minimum timestep size $\triangle t_{min}$, the maximum timestep size $\triangle t_{max}$, N, M, e_{good}, η and μ. We initialize the variables $nupdat \leftarrow 0$, $mupdat \leftarrow 0$ and $\nu \leftarrow 1.25$. The algorithm may be summarized by the steps in Figure 3.5.

Observe in Figure 3.5 that if $e_n > 1.0$ then the solution is unacceptable: Δt is replaced by $\mu \Delta t$, $\mu < 1$, the step growth rate ν is reset to the initial value 1.25, and the time integration is restarted at the previous step. If $e_{good} < e_n \leq 1$ then the solution is acceptable, the algorithm proceeds with the time integration using the current Δt. If $e_n \leq e_{good}$ for N successive steps then the solution is 'overly' accurate. So, Δt is replaced by $\nu \Delta t$, $\nu > 1$. The purpose of step (h) is to provide a variable step size growth rate which allows Δt to be increased at a fast enough rate to raise $e_n = O(1)$ for even the fastest decaying exponential. The cost effectiveness of the

algorithm depends on the subtle interplay between increasing and decreasing step sizes.

The computed step size should always be within user specified bounds, $\Delta t_{min} \leq \Delta t \leq \Delta t_{max}$. If Δt is reduced below Δt_{min}, the user should be informed, and the integration should proceed with $\Delta t = \Delta t_{min}$. The algorithm will generate an accurate solution for any value of μ less than one if the lower bound Δt_{min} is not encountered. In practice they have found the values $\mu = 0.5$, $e_{good} = 0.25$, $N = 2$, $\nu = 1.25$, $M = 3$, and $\eta = 1.1$ to perform well. In the next chapters, the efficiency of our two control strategies for timestep selection will be compared with this approach suggested by Winget and Hughes for some validation problems, chemical reaction systems, Rayleigh-Benard-Marangoni flows and double diffusive problems.

1. Input data: $\mathtt{U}^{n-1}$, $\mathtt{U}^{n}$, $\mathtt{T}^{n-1}$, $\mathtt{T}^{n}$, $\mathtt{C}^{n-1}$, $\mathtt{C}^{n}$, t, Δt, n.

2. Define Parameters: $\triangle t_{min}$, $\triangle t_{max}$, $N = 2$, $M = 3$, $e_{good} = 0.25$, $\eta = 1.1$, $\mu = 0.5$.

3. Initialize variables: $nupdat \leftarrow 0$, $mupdat \leftarrow 0$, $\nu \leftarrow 1.25$, $nrej \leftarrow 0$.

4. Calculate e_n using (3.26)-(3.29).

5. If ($e_n > 1.0$) and ($\triangle t > \triangle t_{min}$) then reject the timestep:

   (a) $nrej \leftarrow nrej + 1$

   (b) $\mathtt{U}^{n} \leftarrow \mathtt{U}^{n-1}$, $\mathtt{T}^{n} \leftarrow \mathtt{T}^{n-1}$, $\mathtt{C}^{n} \leftarrow \mathtt{C}^{n-1}$

   (c) $t \leftarrow t - \triangle t$

   (d) $n \leftarrow n - 1$

   (e) $\nu \leftarrow 1.25$

   (f) $\triangle t \leftarrow \mathtt{max}(\mu \triangle t, \triangle t_{min})$

   else

   (g) If ($e_n \leq e_{good}$) then

      (g1) $nupdat \leftarrow nupdat + 1$

      (g2) If ($nupdat = N$) then

         (g21) $nupdat \leftarrow 0$

         (g22) $\triangle t \leftarrow \nu \triangle t$

         (g23) $mupdat \leftarrow mupdat + 1$

   (h) If ($mupdat = M$) then

      (h1) $mupdat \leftarrow 0$

      (h2) $\nu \leftarrow \eta \nu$

      (h3) $\triangle t \leftarrow \eta \triangle t$

   (i) $\triangle t \leftarrow \mathtt{max}(\triangle t, \triangle t_{max})$

   endif

Figure 3.5: Winget and Hughes Approach

Chapter 4

Validation Problems

The main objective of this chapter is the presentation of numerical experiments to validate the finite element formulations for the Navier-Stokes and transport equations, and our timestep control algorithms. The validation is done separately for each formulation using benchmark problems found in the literature or particular numerical examples constructed to have known solutions. First, we present three test problems to validate the Navier-Stokes equations. Then, four numerical experiments support our SUPG formulation for the transport equations. In the last section, a numerical study is presented to assess the accuracy of the solutions when our timestep control strategies is applied. We also investigate the robustness of our controller.

4.1 Navier-Stokes Equations

This example is motivated by a particular test problem introduced by Johnson and Pitkaranta [50] for the Stokes flow and also studied by Song et al. [64] and Carey and Krishnan [14]. The problem includes a constructed example with known analytic solution. Of particular interest here is to examine the rates of convergence with respect to the mesh size for this test problem and compare them with the theoretical estimates obtained in [14].

The equations describing the problem are the transient Navier-Stokes equations (2.7) and (2.8) subject to prescribed boundary conditions (2.14). The analytic solution for this problem is defined by the smooth velocity components

$$\begin{aligned} u(t,x,y) &= (t+1)^2 x^2 (1-x)^2 (2y - 6y^2 + 4y^3) \\ v(t,x,y) &= (t+1)^2 y^2 (1-y)^2 (-2x + 6x^2 - 4x^3) \end{aligned} \tag{4.1}$$

and the pressure field

$$p(x,y) = x^2 - y^2 \tag{4.2}$$

on the unit square $\Omega = (0,1) \times (0,1)$. This velocity field is divergent free and satisfies the no-slip condition $\mathbf{u} = 0$ on the boundary of the square $\partial\Omega_1$. We assume that $\mathbf{f}(\mathbf{c}) = 0$ in (2.7). Substituting (4.1) and (4.2) in the transient Navier-Stokes equation (2.7), we find that the body force $\mathbf{q} = (q_1, q_2)$ is equal to

$$\begin{aligned} q_1(t,x,y) &= 2(t+1)x^2(1-x)^2(2y-6y^2+4y^3) + \\ &\quad u(t,x,y)(t+1)^2(2x-6x^2+4x^3)(2y-6y^2+4y^3) + \\ &\quad v(t,x,y)(t+1)^2(2-12y+12y^2)(1-x)^2 + \\ &\quad (t+1)^2 2(x-0.02((1-6(x-x^2))(y-3y^2+2y^3) + \\ &\quad (1-x)^2x^2(-3+6y))) \end{aligned} \tag{4.3}$$

$$\begin{aligned} q_2(t,x,y) &= 2(t+1)y^2(1-y)^2(-2x+6x^2-4x^3) - \\ &\quad u(t,x,y)(t+1)^2y^2(-2+12x-12x^2)(1-y)^2 + \\ &\quad v(t,x,y)(t+1)^2(2y-6y^2+4y^3)(-2x+6x^2-4x^3) + \\ &\quad (t+1)^2 2(y+0.02((1-6(y-y^2))(-x+3x^2-2x^3) + \\ &\quad (1-y)^2y^2(3-6x))). \end{aligned} \tag{4.4}$$

The viscosity is chosen as 0.01, and we take a constant penalty parameter of $\epsilon = 10^{-8}$. The maximum nodal velocity is approximately 1.2×10^{-2}, which corresponds to a Reynolds number of 1.2.

The approximate solutions are computed for a sequence of uniform meshes with mesh size $h = \frac{1}{2}$, $\frac{1}{4}$, $\frac{1}{8}$, $\frac{1}{16}$ and $\frac{1}{32}$, and all the approximations are shown for the first timestep, that is, $t_0 = 10^{-5}$. The initial condition is taken as the exact solution at the initial time $t = 0$. We consider bilinear elements with 1-point Gauss quadrature for the penalty term (Case 1) and biquadratic elements with 2×2 Gauss quadrature for the penalty term (Case 2). Our objective now is to examine the rates of convergence with respect to the mesh size h and to compare with the theoretical estimates.

Table 4.1 shows the error in the approximate velocity in the L^2-norm ($\|\cdot\|_0$) and H^1-norm ($\|\cdot\|_1$) for the refined meshes in Case 1 (bilinear). The error in the approximate velocity is plotted against mesh size h on a log-log scale in Figure 4.1. The respective approximate slopes of 1.9026 and 0.9797 indicate global rates of convergence. The theoretical rates of convergence in Case 1 in the $\|\cdot\|_0$ and $\|\cdot\|_1$ norms are equal to 2 and 1, respectively.

In Case 2 (biquadratic), the errors in the velocity in the norms $\|\cdot\|_0$ and $\|\cdot\|_1$ are shown in Table 4.2. Figure 4.2 shows the error in the approximate velocity plotted

Mesh Size	L^2-norm	H^1-norm
h = 1/2	$.7746371E-02$	$.5754133E-01$
h = 1/4	$.2463945E-02$	$.3099890E-01$
h = 1/8	$.6504252E-03$	$.1551478E-01$
h = 1/16	$.1641288E-03$	$.7734176E-02$
h = 1/32	$.4107556E-04$	$.3861947E-02$

Table 4.1: The L^2-norm and H^1-norm of error in the velocity solution in Case 1 (bilinear).

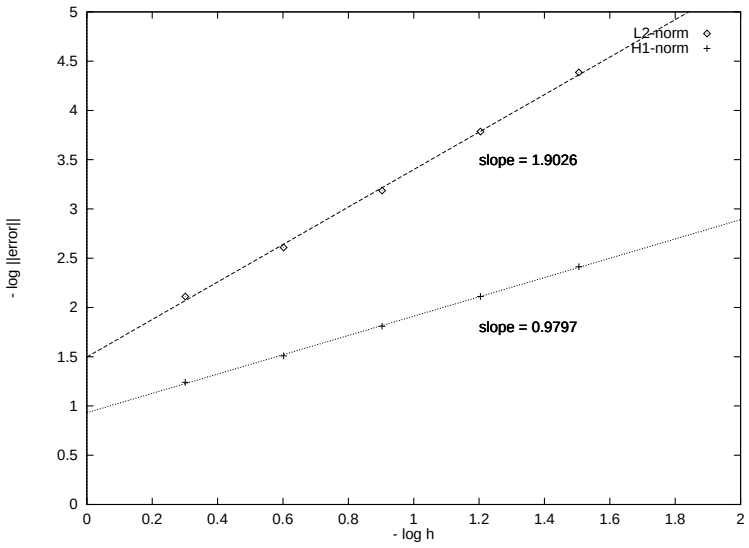

Figure 4.1: Optimal global rates of convergence for the velocity in Case 1 (bilinear).

against mesh size h on a log-log scale. Now, the theoretical rates of convergence in the $\|\cdot\|_0$ and $\|\cdot\|_1$ norms are equal to 3 and 2, respectively. The slopes of the curves yield rates of convergence for the velocity 2.9628 and 2.0154 in the $\|\cdot\|_0$ and $\|\cdot\|_1$ norms, respectively. Hence we find that the velocity approximations in both cases converge towards the exact solution at optimal rates.

Mesh Size	L^2-norm	H^1-norm
h = 1/2	$.1021730E-02$	$.1866761E-01$
h = 1/4	$.1404786E-03$	$.4521962E-02$
h = 1/8	$.1786013E-04$	$.1117877E-02$
h = 1/16	$.2242721E-05$	$.2786661E-03$
h = 1/32	$.2806901E-06$	$.6961698E-04$

Table 4.2: The L^2-norm and H^1-norm of error in the velocity solutions in Case 2 (biquadratic).

The second numerical experiment is the backward-facing step problem, which has become popular as a benchmark problem addressed by numerous authors developing flow simulation codes. It consists of a fluid flowing in a straight channel which

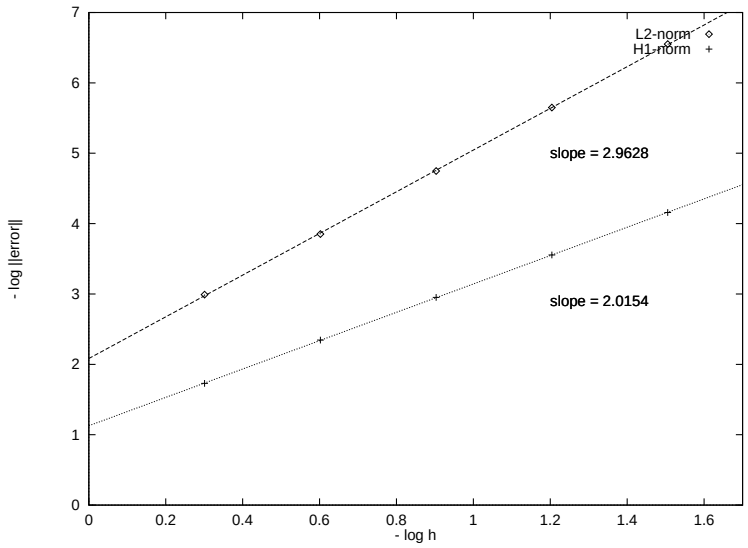

Figure 4.2: Optimal global rates of convergence for the velocity in Case 2 (biquadratic).

abruptly widens on one side. Results of physical experiments are given in Armaly et al. [1], and numerical results obtained using different finite element methods can be found, for example, in Gartling [34] and Cruchaga [26]. Griebel, Dornseifer and Neunhoeffer [38] solve the problem for different Reynolds numbers using a finite difference approach. Numerical results using our penalty finite element formulation are compared with those published by Griebel, Dornseifer and Neunhoeffer in [38].

The problem involves a viscous incompressible flow over an isothermal two-dimensional backward-facing step. Introducing the dimensionless variables

$$x^* = \frac{x}{L}, \quad y^* = \frac{y}{L}, \quad t^* = \frac{t u_\infty}{L}, \quad u^* = \frac{u}{u_\infty}, \quad v^* = \frac{v}{v_\infty}, \quad p^* = \frac{p - p_\infty}{\rho_\infty u_\infty^2} \tag{4.5}$$

with given scalar constants L, u_∞, p_∞, ρ_∞, and substituting these relations into (2.7) and (2.14), we obtain the dimensionless Navier-Stokes equations of the problem

$$\frac{\partial \mathbf{u}}{\partial t} + \mathbf{u} \cdot \nabla \mathbf{u} - \frac{1}{Re} \Delta \mathbf{u} + \boldsymbol{\nabla} p = 0 \qquad \text{in } \Omega \tag{4.6}$$

$$\boldsymbol{\nabla} \cdot \mathbf{u} = 0 \qquad \text{in } \Omega \tag{4.7}$$

where we dropped the superscript * for simplicity, and $Re = \frac{\rho_\infty u_\infty L}{\mu}$ is the Reynolds number. Figure 4.3 shows the geometry of the problem and the boundary conditions. We assume

$$\begin{aligned} \text{walls} \quad &: \quad u = v = 0; \\ \text{inlet} \quad &: \quad u = 1.0, \; v = 0; \\ \text{exit at x = 30} \quad &: \quad \frac{\partial u}{\partial x} = 0, \; \frac{\partial v}{\partial x} = 0. \end{aligned}$$

The initial velocity is $u = 1.0$, $v = 0$ in the upper half of the domain and $u = v = 0$ in the lower half. The obstacle domain representing the step is the rectangle $[0, 7.5] \times [0, 0.75]$ and the inflow velocity at the left wall has the constant value $u = 1.0$. The length L measured from the step to the end of the calculation domain was selected to make the reattachment length independent of the calculation domain, and the boundary condition at the outflow section was taken as that of a fully developed flow. We solve the problem towards to steady-state for two Reynolds numbers, $Re = 100$ and $Re = 500$.

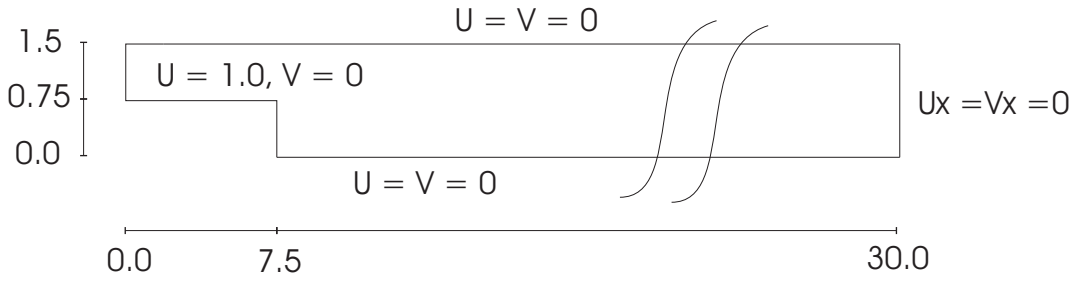

Figure 4.3: Backward-facing step geometry with channel dimensions and boundary conditions.

The rectangular channel downstream of the step was divided into two regions for purposes of mesh generation. In the upstream region $0 \leq x \leq 15$ the mesh is uniformly distributed across the channel and in the streamwise direction. Element sizes in the uniform grid region are $(\Delta x, \Delta y) = (0.1875, 0.3)$, which represents 40×5 and 80×5 elements in the bottom $(0 \leq y \leq 0.75)$ and top $(0.75 \leq y \leq 1.5)$ upstream regions, respectively. For the downstream region $15 \leq x \leq 30$ and $0 \leq y \leq 1.5$ the mesh is uniform across the channel but smoothly graded in the flow direction. For $i = 2, \ldots, nx$, the nodes in the grid are calculated using the expression,

$$x(i) = 15 + 15 * (\frac{i-1}{nx-1})^{1.2} \tag{4.8}$$

where $nx = 30$ is the number of elements in the downstream region. We have 30×10 elements in the downstream region. Elements near $x = 30$ are approximately twice the length of elements near $x = 15$. For this mesh about two-thirds of the total number of elements are located in the upstream region. We have 600 elements in the upstream region and 300 elements in the downstream region. The steady state solution is obtained when $\|\mathbf{u}^n - \mathbf{u}^{n-1}\| < 10^{-7} \|\mathbf{u}^n\|$. We used a fixed time step size of $\Delta t = 0.01$ at the beginning of the process and then we keep the time step size at $\Delta t = 0.1$. Results were obtained using the four-node continuous bilinear velocity elements with 1-point Gauss quadrature for the penalty term.

The basic character of the backward-facing step flow at $Re = 100$ and $Re = 500$ is well known and is illustrated in the contour plots of Figure 4.4. Note that the figures show only the part of the computational domain $6 \leq x \leq 20$, since this contains all the essential features. The streamlines shown in Figure 4.4 reveal that, for $Re = 100$, the flow widens immediately behind the step and an eddy is formed. When viscosity is further reduced ($Re = 500$), the main flow is drawn downward, causing it to separate from the upper boundary and leading to the formation of a second eddy. Note that the first eddy increases in size with increasing Reynolds number ($Re = 500$).

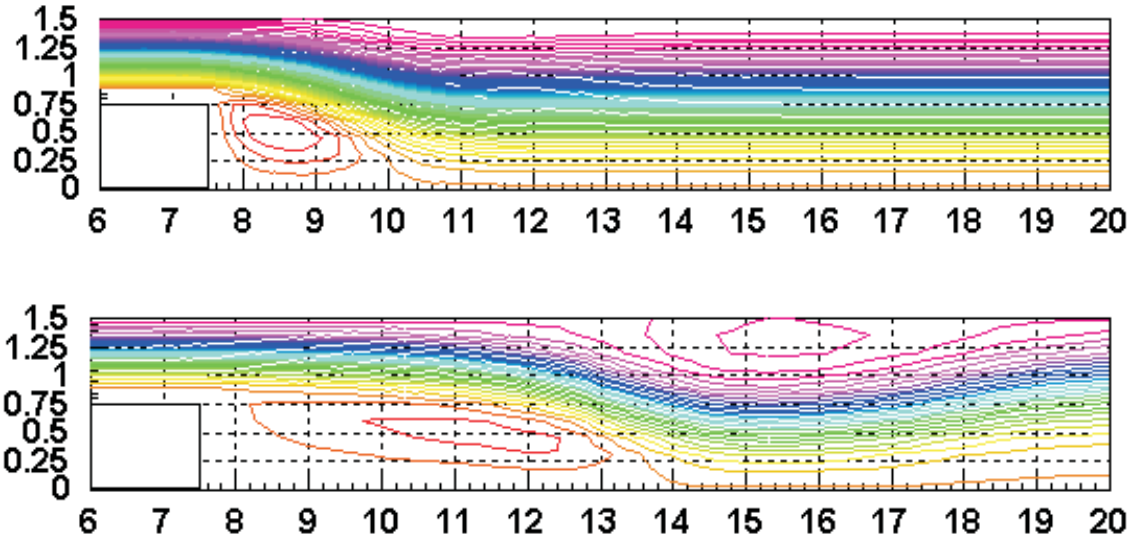

Figure 4.4: Flow over a backward-facing step, streamlines at $Re = 100$ (top) and $Re = 500$ (bottom).

The lengths x_1 and x_2 of the upper and lower eddies as well the horizontal distance x_3 from the step to the upper eddy's point of separation are values often used to characterize the resulting flow, see Figure 4.5. Table 4.3 shows the characteristic lengths - each normalized by the step height s - obtained by Griebel, Dornseifer and Neunhoeffer in [38] for $Re = 100$ and $Re = 500$.

	Griebel et al.		
Re	x_1/s	x_2/s	x_3/s
100	3.8	-	-
500	8.3	9.1	6.2

Table 4.3: Flow over a backward-facing step - characteristic lengths

For $Re = 100$, we can observe in Figure 4.4 that the flow separates at the step

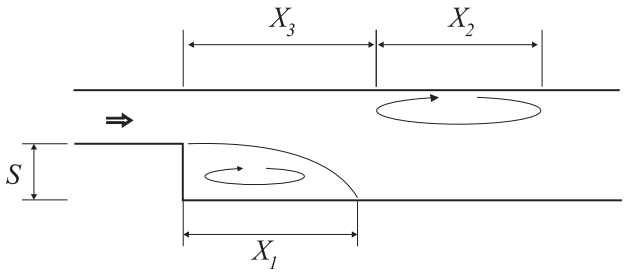

Figure 4.5: Characteristic lengths.

corner and forms a recirculation eddy with a reattachment point on the lower wall approximately at $x = 10.35$ which corresponds to $x_1 = 2.85$ ($x1/s = 3.8$). This eddy increases in size to $x = 13.725$ ($x1/s = 8.3$) with the increasing Reynolds number ($Re = 500$). A second eddy forms on the upper wall, for $Re = 500$, beginning approximately at $x = 12.15$ ($x_3/s = 6.2$) and terminating at $x = 18.975$ ($x_2/s = 9.1$). So, our results are in very good agreement with the results obtained by Griebel, Dornseifer and Neunhoeffer in [38].

The third example is also a problem involving a steady viscous incompressible flow over an isothermal two-dimensional backward-facing step. Now, the standard step geometry was simplified by excluding the channel upstream of the step (see Figure 4.6). This problem has been addressed by numerous authors but we are going to compare our results with the results presented by Gartling in [34]. The boundary conditions for the step geometry included the usual no-slip velocity specification for all solid surface walls as shown in Figure 4.6. The inlet velocity field is specified as a parallel flow given by $u(y) = 24y(0.5 - y)$ and $v(y) = 0$ for $0 \leq y \leq 0.5$. This produces a maximum inflow velocity of $u_{max} = 1.5$ and an average inflow velocity of $u_{avg} = 1.0$. We consider homogeneous natural outflow boundary condition as shown in Figure 4.6. The problem is solved for a Reynolds number of $Re = 800$.

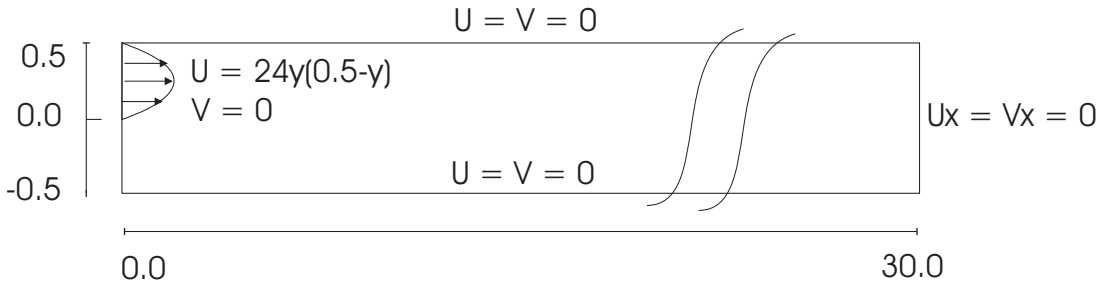

Figure 4.6: Backward-facing step geometry with channel dimensions and boundary conditions.

We use a mesh similar to the one used in the last example. In the upstream

region $0 \leq x \leq 15$ the mesh is uniformly distributed across the channel and in the streamwise direction. The lengths of the element size for the uniform grid region are $(\Delta x, \Delta y) = (0.1, 0.0833)$, which represents 150×12 elements. For the downstream region $15 \leq x \leq 30$ the mesh is uniform across the channel but smoothly graded in the flow direction. The nodes in the grid are calculated using (4.8). We have $50 \times 12 = 600$ elements in the downstream region and 1800 elements in the upstream region. The steady state solution is obtained when $\|\mathbf{u}^n - \mathbf{u}^{n-1}\| < 10^{-4} \ \|\mathbf{u}^n\|$. Results were computed using the four-node continuous bilinear velocity elements with 1-point Gauss quadrature for the penalty term, and we used a fixed time step size of $\Delta t = 0.01$.

The basic character of the backward-facing step flow at $Re = 800$ is illustrated in the streamfunction contour plots of Figure 4.7. The plot shows only part of the channel since few phenomena of interest occur downstream of this point. Gartling in [34] found that the flow separates at the step corner and forms a large recirculation eddy with a reattachment point on the lower wall approximately at $x = 6.10$. A second stronger eddy is formed on the upper wall beginning approximately at $x = 4.85$ and terminating at $x = 10.48$. Our results are in good agreement with the results obtained by Gartling in [34].

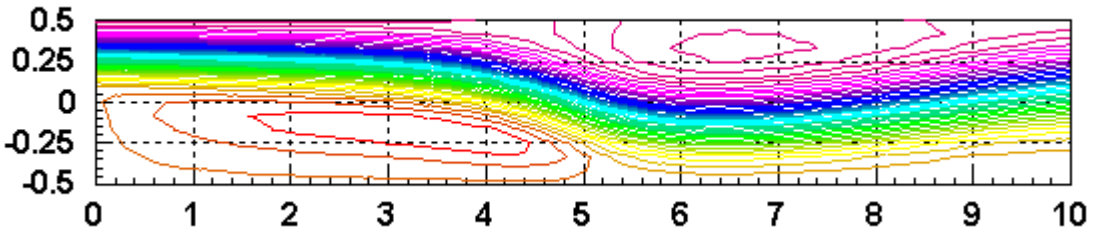

Figure 4.7: Flow over a backward-facing step, streamfunction contours at $Re = 800$.

4.2 Transport Equations

Our first experiment is a test problem constructed to have in the unit square domain $[0, 1] \times [0, 1]$ and for $t > 0$ the analytic solution

$$c = 10^2(t + 1)^2 x(x - 1)y(y - 1), \tag{4.9}$$

where c is the solution of the transport equation (2.19) considering one species component. The velocity field is the same used in the first example of the previous

section 4.1, whose velocity components are

$$\begin{aligned} u(t,x,y) &= (t+1)^2x^2(1-x)^2(2y-6y^2+4y^3) \\ v(t,x,y) &= (t+1)^2y^2(1-y)^2(-2x+6x^2-4x^3). \end{aligned}$$

We assume the diffusion tensor $k_{11} = k_{22} = 1$, $k_{12} = k_{21} = 0$ in (2.19), and the nonlinear reaction term is taken to be

$$h(x,y) = -c^2 + f, \tag{4.10}$$

where the function f is given by

$$f = \frac{\partial c}{\partial t} + u\frac{\partial c}{\partial x} + v\frac{\partial c}{\partial y} - k_{11}\frac{\partial^2 c}{\partial x^2} - k_{22}\frac{\partial^2 c}{\partial y^2} + c^2.$$

The initial solution is defined as the exact solution at the initial time $t = 0$. We specify essential boundary conditions, $c(t,x,y) = 0$ from (2.18) evaluated on the boundary of the unit square domain Ω. For this test problem, of particular interest is to examine the rates of convergence of the concentration with respect to the mesh size h and the time step Δt, and compare them with the theoretical estimates.

The transport equation is solved using the bilinear, biquadratic and six-node triangular elements described earlier for a sequence of uniform meshes with mesh size $h = \frac{1}{2}, \frac{1}{4}, \frac{1}{8}, \frac{1}{16}$, and $\frac{1}{32}$. In the case of bilinear elements, we also compute the solution at $h = \frac{1}{64}$. For the convergence study with respect to h we keep a constant small timestep of $\Delta t = 10^{-5}$. All the approximations are shown for the first time step $t = 10^{-5}$.

The L^2-norm of the error in the concentration solution for bilinear and six-node triangular elements is shown in Table 4.4. The L^2-norm and H^1-norm of the error for the concentration using bilinear elements are plotted against mesh size in Figure 4.8 on a log-log scale. The respective slopes 1.9708 and 1.0202 indicate the global rates of convergence, and are in good agreement with the theoretical predictions 2 and 1, respectively.

For biquadratic elements we obtain relative errors in the L^2-norm of order less than 10^{-8} for any number of elements. This means that we obtain the exact solution within roundoff error, as expected. Optimal global rates of convergence are also obtained for six-node triangular elements in both norms as shown in Figure 4.9. The rates of convergence for the concentration approximation in the L^2-norm and H^1-norm for this example are 2.9480 and 1.9699, respectively.

We also examined the order of convergence of the solution with respect to the time step Δt. In view of the above convergence results we select for this study

Mesh Size	4-node bilinear	6-node triangular
h = 1/2	$.12873418E+01$	$.30613016E+00$
h = 1/4	$.35371359E+00$	$.43871262E-01$
h = 1/8	$.90379168E-01$	$.56366812E-02$
h = 1/16	$.22716094E-01$	$.70867673E-03$
h = 1/32	$.56865900E-02$	$.88027891E-04$

Table 4.4: The L^2-norm of the error in concentration for 4-node bilinear and 6-node triangular elements.

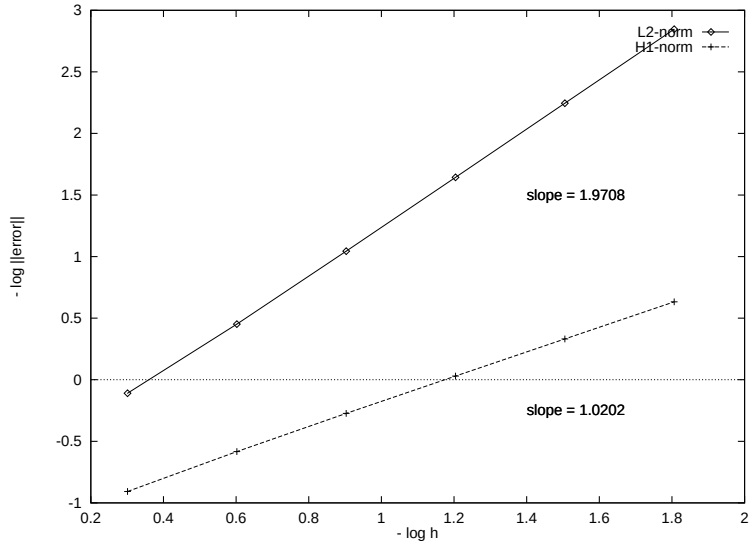

Figure 4.8: Rates of convergence for the concentration approximation in the L^2-norm and H^1-norm with bilinear functions

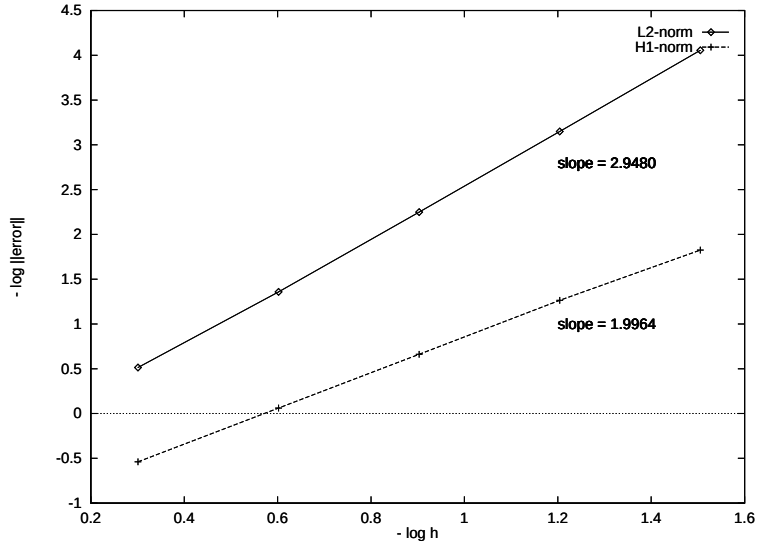

Figure 4.9: Rates of convergence for the concentration approximation in the L^2-norm and H^1-norm with six-node triangular elements

biquadratic basis functions and a mesh with 2×2 elements. The approximate solutions are compared at the time $t = 0.1$ for values of Δt equal to $10^{-2}, 10^{-3}, 10^{-4}$ in Table 4.5. The error in the L^2-norm is plotted against Δt on a log-log scale in Figure 4.10. We know that the theoretical truncation error for the Crank-Nicolson scheme is $O(\Delta t^2)$, and we see an approximate slope of 2.0397.

Time Step Size	L^2-norm of the error
$\Delta t = 10^{-2}$	$.16462243E-01$
$\Delta t = 10^{-3}$	$.13438152E-03$
$\Delta t = 10^{-4}$	$.13711075E-05$

Table 4.5: The L^2-norm of error in the concentration solution for a mesh with 2×2 biquadratic elements.

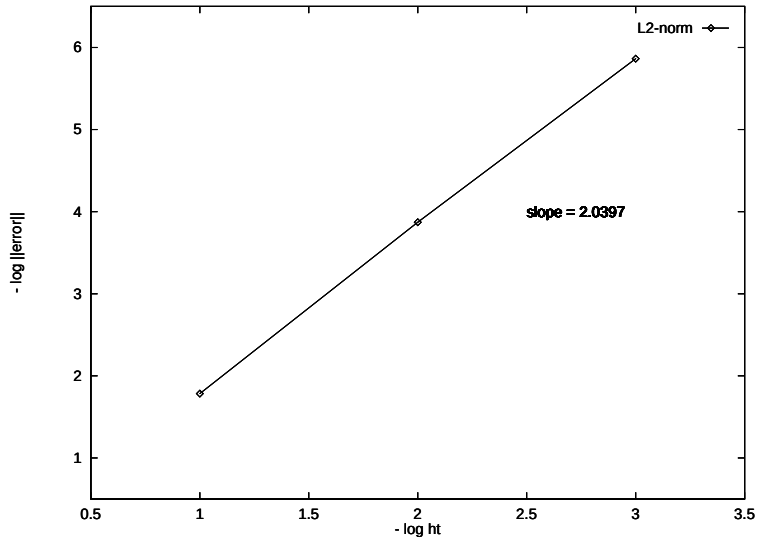

Figure 4.10: Rates of convergence for the concentration approximation in the L^2-norm using Crank-Nicolson method with 2×2 biquadratic elements

The second experiment is a test problem found in [11] to demonstrate the effectiveness of the streamline upwind method in preventing both "wiggles" and spurious crossing diffusion. The flow is unidirectional, constant ($\|c\| = 1$), and skew to the mesh ($\theta = \pi/8$) with discontinuous inflow boundary condition and homogeneous natural outflow boundary condition as shown in Figure 4.11. The diffusivity coefficient is equal to $k = 10^{-6}$ resulting in a Peclet number of $Pe = 10^6$. The steady-state solution is obtained when $\|\mathbf{c}^n - \mathbf{c}^{n-1}\| < 10^{-6} \|\mathbf{c}^n\|$. The initial conditions are

$$\begin{aligned} c &= 1 \qquad x = 0, \;\; 0 \leq y \leq 0.25 \\ c &= 0 \qquad x = 0, \;\; 0.25 < y \leq 1 \end{aligned}$$

The problem is advection dominated, and the solution is essentially one of pure advection. The "exact" solution is an advection of the inflow boundary in the flow direction. We use a 10-by-10 mesh of equal sized square elements, 2-by-2 Gaussian quadrature to integrate all element contributions, and a fixed timestep size of $\Delta t = 0.01$. Figure 4.12 shows the results using the Galerkin scheme and the SUPG formulation. We observe that as expected the SUPG scheme is significantly better than the Galerkin method in reducing the spurious oscillations on the coarse grid.

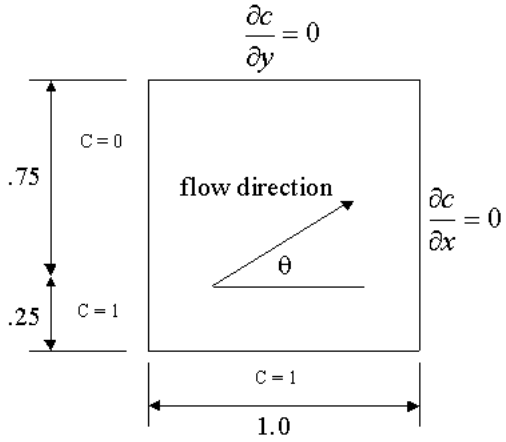

Figure 4.11: Advection skew to the mesh: problem statement.

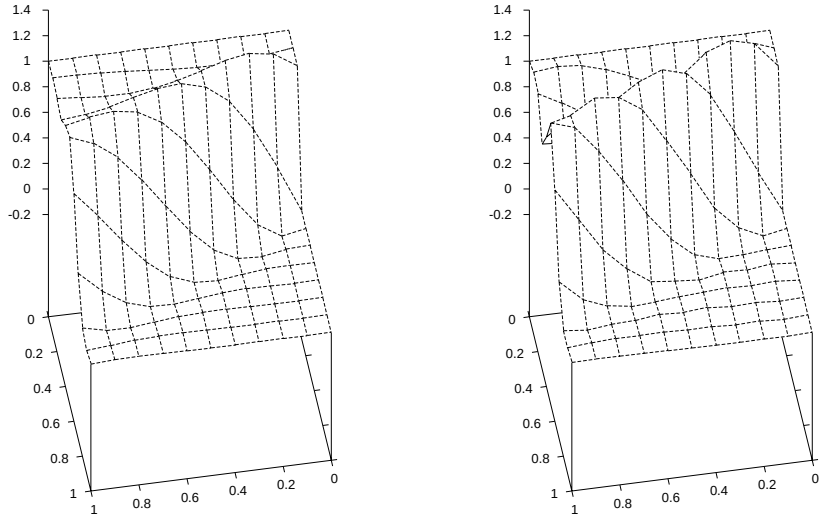

Figure 4.12: Advection skew to the mesh with homogeneous natural outflow boundary condition: elevation of c - SUPG (left) and Galerkin (right).

The third experiment is also a problem presented in [11]. The flow is a rigid rotation about the center of a unit square domain, $\Omega = [-0.5, 0.5] \times [-0.5, 0.5]$, with velocity components given by

$$u = -y \quad \text{and} \quad v = x,$$

and the diffusivity coefficient is $k = 10^{-6}$. On the external boundary of the square c is set to zero, and on the internal 'boundary' OA, c is prescribed to be a cosine hill, as shown in Figure 4.13.

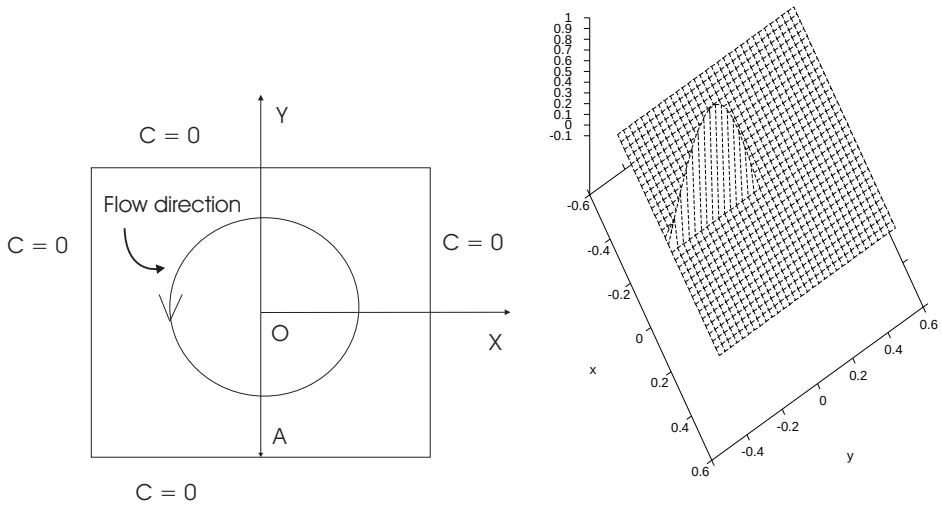

Figure 4.13: Advection in a rotating flow field: problem statement.

We used a 30-by-30 mesh of equal sized square elements, and a fixed timestep size of $\Delta t = 0.01$. The steady-state solution is obtained when $\|\mathbf{c}^n - \mathbf{c}^{n-1}\| < 10^{-3} \|\mathbf{c}^n\|$. The initial conditions are

$$\begin{aligned} c &= cos(2\pi(y + 0.25)) \qquad \text{on OA} \\ c &= 0 \qquad\qquad\qquad\quad \text{on the rest of the domain} \end{aligned}$$

The problem is also advection dominated. The exact solution is essentially a pure advection of the OA boundary condition along the circular streamlines. The elevation of c using the SUPG scheme is shown in Figure 4.14, and is in good agreement with the exact solution.

The last experiment with the SUPG method is a test problem presented in [20]. The domain of the problem is the unit square, $\Omega = [0, 1] \times [0, 1]$, discretized using a uniform mesh of 20×20 bilinear elements. The diffusion coefficient is set to

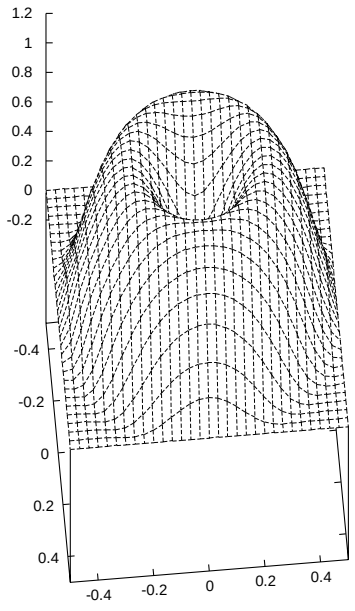

Figure 4.14: Advection in a rotating flow field: elevation of c (SUPG scheme).

$k = 10^{-4}$. The nonlinear reaction source term in (2.19) is defined as $h = 1 - s\,c$ where $s \geq 0$ is the absorption coefficient. The velocity field is

$$\mathbf{u} = \|\mathbf{u}\|\,(cos(\pi/3), sin(\pi/3)),$$

so that it is not aligned with the finite element mesh. Three different cases are considered, corresponding to dominant advection (Case 1), dominant reaction (Case 2) and combination of advection and reaction effects (Case 3). These cases are:

$$\begin{aligned}
\text{Case 1} \quad &: \quad \|\mathbf{u}\| = 1, \qquad\quad s = 0.0001 \\
\text{Case 2} \quad &: \quad \|\mathbf{u}\| = 0.0001, \quad s = 1 \\
\text{Case 3} \quad &: \quad \|\mathbf{u}\| = 0.5, \qquad\quad s = 1
\end{aligned}$$

Results for the the three cases are shown in Figure 4.15 using the SUPG formulation. For the first case, the solution shows some oscillations near the boundary layer created due to the small diffusion coefficient. In Case 3 the effect of convection and reaction are both present, and there are oscillations due to the presence of convection. The oscillations are dominated by those due to the convection since $Ab = \frac{sh^2}{2k}$ is much smaller than Pe. The dimensionless number Ab is a measure of the relative importance of the absorption and diffusion terms, where h is the element

size. Our results are in good agreement with those presented in [20] for all three cases.

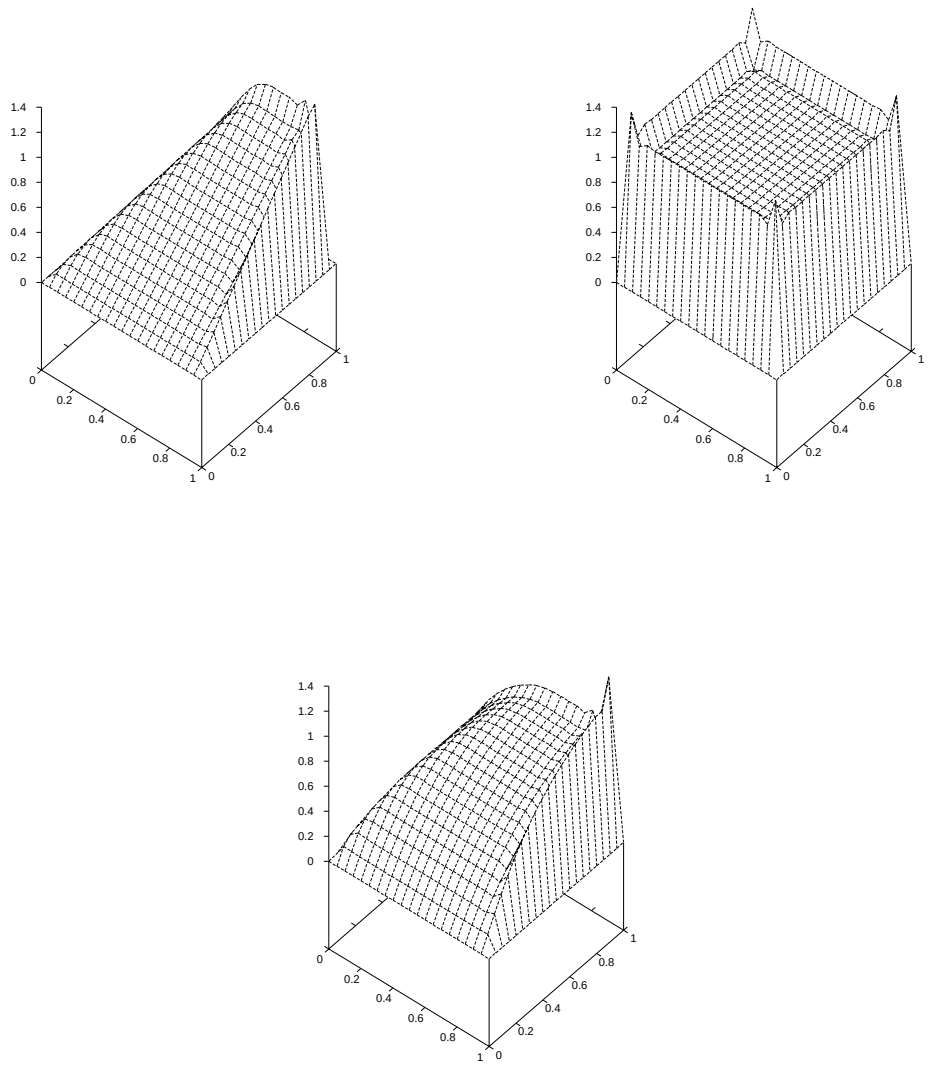

Figure 4.15: Case 1 (left top), Case 2 (right top) and Case 3 (bottom).

4.3 Timestep Control Algorithms

Our main objective now is to assess the accuracy of the solutions when the timestep control strategies studied previously are applied to a specified problem. For this investigation, we are going to apply Control 1 to the first validation problem for the transport equations. We also want to verify whether the PID controller is robust or not. Thus, we perform parametric studies for different values of PID parameters k_P, k_I and k_D, and compare our timestep control algorithm to the strategy developed by

Winget and Hughes [79]. We use in these experiments a grid with 2×2 biquadratic elements. The initial timestep size is 10^{-4}, and we allow a minimum and a maximum time step sizes of 10^{-4} and 10^{-3}, respectively. Changes in nodal concentration are calculated with an input tolerance of 10^{-5}, and the calculations stop when the time is greater than 0.1. We perform parametric studies of the timestep controller for values similar to those used by Gustafsson et al. [39] and also by Coutinho and Alves [24]. We choose values of k_P ranging from 0.03 to 0.20, k_I from 0.03 to 0.40, and k_D from 0.003 to 0.02. We also study the case where $k_P = k_D = 0$.

Table 4.6 shows the L^2-norm of the error in the concentration solution, the number of time iterations, $ntstep$, the number of rejected steps, $nrejec$, the total number of Newton iterations, $newt$, and the computational effort, c_{effort}, defined here as $newt$ divided by the number Newton iterations obtained using a fixed timestep size of 10^{-4}. We can see from Table 4.6 that the error in the approximate solution at the final time is of order 10^{-6} for all cases studies. Moreover, with the PID control strategy we find approximate solutions with a much smaller number of time steps without any significant loss of accuracy. Observe that we need 100 time steps to obtain a solution with the same accuracy when the minimum fixed time step is used (Table 4.6). The step size selection strategy developed by Winget and Hughes took 66 time steps with no rejected steps.

case	k_P, k_I, k_D	$error$	$ntstep$	$nrejec$	$newt$	c_{effort}
1	0.05 0.05 0.005	.37023368E-05	66	0	132	0.66
2	0.1 0.3 0.015	.38890581E-05	62	0	124	0.62
3	0.075 0.175 0.01	.38512072E-05	62	0	124	0.62
4	0.1 0.16 0.011	.38680409E-05	63	0	126	0.63
5	0.06 0.13 0.008	.38456781E-05	63	0	126	0.63
6	0.08 0.216 0.0116	.38684855E-05	62	0	124	0.62
7	0.15 0.32 0.017	.38897674E-05	62	1	126	0.63
8	0.2 0.4 0.02	.38896720E-05	62	2	128	0.64
9	0.04 0.04 0.004	.36271440E-05	67	0	134	0.67
10	0.03 0.03 0.003	.35057604E-05	69	0	138	0.69
11	0.0 0.175 0.0	.38528566E-05	62	0	124	0.62
12	0.075 0.175 0.0	.38512100E-05	62	0	124	0.62
13	No control	.13711077E-05	100	0	200	1
14	Winget & Hughes	.32976399E-05	66	0	132	0.66

Table 4.6: Results for Control 1 using bilinear elements on a 2×2 grid.

The PID controller is very robust as we can also see from Table 4.6. Although feedback control theory provides techniques to choose the PID parameters, robust-

ness is required when a general finite element method is used for a wide range of different simulations. The variation in the number of time iterations is very small if we keep k_P in the range 0.03 to 0.20, k_I from 0.03 to 0.40, and k_D from 0.003 to 0.02. In the numerical problems presented in the next Chapter, we see that these parameters are also suitable for the examples studied there. For these reasons, we fix the values of the PID parameters equal to $k_P = 0.075$, $k_I = 0.175$ and $k_D = 0.01$ in all the numerical experiments performed subsequently. To provide examples of the evolution of timesteps we show in Figures 4.16 and 4.17 Cases 3 and 14, where we may verify that the PID solution presents a smooth variation of timesteps when confronted with the Winget and Hughes test problems.

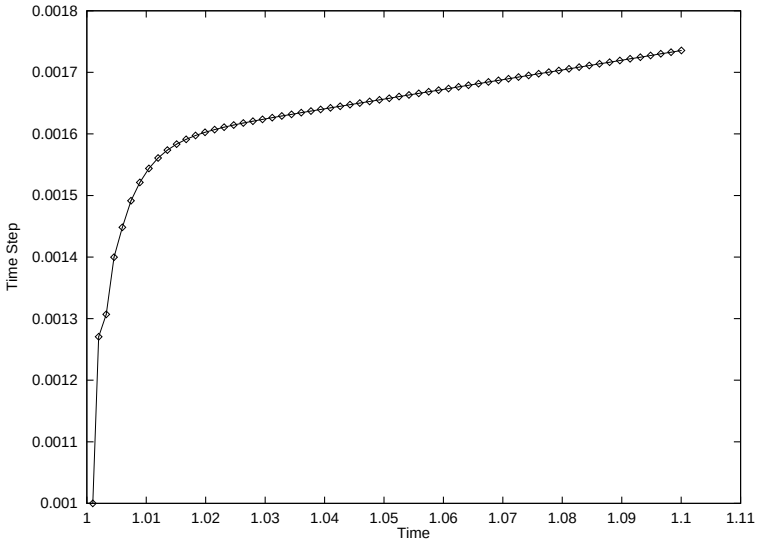

Figure 4.16: Time step variation for case 3 on a 2×2 grid using Control 1.

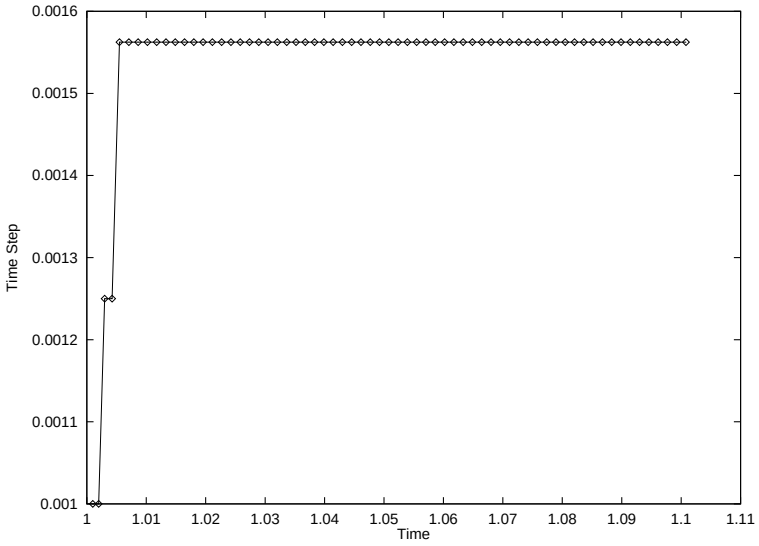

Figure 4.17: Time step variation on a 2×2 grid using Winget and Hughes approach.

Chapter 5

Chemical Reaction Systems

In this chapter we apply our adaptive timestep control algorithm to solve numerical applications involving isothermal reaction inside a porous catalyst and chemical reaction on a catalyst section with heat effects included. We compare the performance of Control 1 and the time-stepping strategy proposed by Winget and Hughes in [79]. One objective is to validate our code when Control 1 is applied to combined diffusion-reaction processes with heat effects included. We also want to demonstrate the efficiency of our PID controller to solve nonlinear flow and reactive transport problems.

5.1 Isothermal Reaction

5.1.1 Dimensionless Equations

When a catalyst particle made from a porous material impregnated with a catalytic substance is submerged in a gas stream, the reactant A diffuses into the particle, reacts on the catalytic surface, and the product B diffuses out, $A \rightarrow B$. We assume that the process is isothermal, i.e., the heat generated by the reaction can be neglected, and homogeneous, the chemical change takes place in the entire volume of the fluid. We also assume that the reaction mechanism is known [33, 7].

Consider a catalyst section exposed to reactant A with concentration $\hat{c}$ at the surface. The rate of disappearance of reactant A is given by the following second-order, irreversible reaction

$$R = -kc^2$$

where c is the concentration of reactant A in the neighborhood of the surface, and k is a rate constant. The governing equation of the problem is

$$\frac{\partial c}{\partial t} - \mathcal{D}\nabla^2 c \;=\; -kc^2 \tag{5.1}$$

with boundary conditions

$$-k\frac{\partial c}{\partial x} = 0 \qquad \text{on } \partial\Omega_2 \tag{5.2}$$

$$c = \hat{c} \qquad \text{on } \partial\Omega_1 \tag{5.3}$$

and initial condition

$$c(x, y, 0) = \hat{c}_0(x, y) \qquad \text{in } \Omega \tag{5.4}$$

where $\mathcal{D}$ is the effective diffusivity measured experimentally, $\Omega = [0, L] \times [0, L]$ is the section, $\partial\Omega_1$ is the right side of the domain, and $\partial\Omega_2 = \partial\Omega - \partial\Omega_1$.

The problem is scaled as follows: $x^* = x/L$, $y^* = y/L$, $t^* = t\mathcal{D}/L^2$, and $c^* = c/\hat{c}$. Substituting these relations into (5.1), (5.2), (5.3) and (5.4), we obtain the scaled form of the equations

$$\frac{\partial c}{\partial t} - \nabla^2 c = -\phi^2 c^2 \tag{5.5}$$

$$\frac{\partial c}{\partial x} = 0 \qquad \text{on } \partial\Omega_2 \tag{5.6}$$

$$c = 1 \qquad \text{on } \partial\Omega_1 \tag{5.7}$$

$$c(x, y, 0) = c_0(x, y) \qquad \text{in } \Omega \tag{5.8}$$

where we drop the superscript * for simplicity, $\Omega = [0, 1] \times [0, 1]$ is the dimensionless section, $\partial\Omega_1$ is the right side of the domain, $\partial\Omega_2 = \partial\Omega - \partial\Omega_1$ and ϕ is the Thiele modulus defined as

$$\phi = \sqrt{k\hat{c}L^2/\mathcal{D}}.$$

5.1.2 Isothermal Reaction in a Catalyst Slab

We are interested in steady-state solutions of the problem for different values of the Thiele modulus ϕ. We assume that the steady-state occurs when $\|c^{n+1} - c^n\| < \tau_c \|c^{n+1}\|$, where n denotes the timestep index, $\|\cdot\|$ denotes Euclidean norm, and τ_c is equal to 10^{-7} in this example. Since we are simulating a 1-D problem, we choose in all cases a mesh with 16×1 bilinear elements. We use Control 1, (3.25), (3.26), (3.27) and (3.29), to calculate all approximate steady-state solutions.

The effectiveness factor η gives the ratio of the amount reacted with diffusion to the amount that would be reacted if the concentration were everywhere the same, and equal to the value at the boundary. In this example, the effectiveness factor can be defined by the equation

$$\eta = \frac{\int_0^1 \phi^2 c^2 dx}{\int_0^1 \phi^2 1 dx}. \tag{5.9}$$

Finlayson [33] calculates approximate solutions for the problem on the interval [0,1] using the orthogonal collocation method. He shows that for one interior collocation point the effectiveness factor can be expressed by

$$\eta = \frac{1}{6} + \frac{5}{24}\frac{[-2.5 + (6.25 + 10\phi^2)^{1/2}]^2}{\phi^4}. \tag{5.10}$$

The approximation is accurate for $\phi \leq 2$, and for larger values of ϕ a higher approximation is required to improve the results. The effectiveness factor η is plotted versus the Thiele modulus ϕ in Figure 5.1 for the collocation method and Galerkin method. We can see that the two curves coincide for $\phi \leq 1.2$.

For large values of ϕ Petersen [58] shows that an asymptotic solution is available. In this case the general formula becomes

$$\eta = \sqrt{\frac{2}{3}}\frac{1}{\phi}. \tag{5.11}$$

Figure 5.2 shows the effectiveness factor η plotted against the Thiele modulus ϕ for values of $\phi \geq 3$. Observe that accurate solutions are also obtained for large values of ϕ. Consequently, the Galerkin formulation combined with Control 1 gives adequate approximations for all values of ϕ. The numerical finite element solutions for different values of the Thiele modulus are shown in Figure 5.3.

5.2 Nonisothermal Reaction

5.2.1 Dimensionless Equations

Consider a first-order, irreversible reaction in a catalyst section $\Omega = [-L, L]\times[-L, L]$ with reaction rate given by

$$R = -a\, c\, \exp(-\Delta E/\hat{R}T),$$

where T is the absolute temperature, ΔE is the activation energy, $\hat{R}$ is the gas constant, and a is constant. The corresponding governing equations are:

$$\rho c_p \frac{\partial T}{\partial t} + \rho c_p \mathbf{u}\cdot\nabla T - k\nabla^2 T = a\, c\, \exp(-\frac{\Delta E}{\hat{R}T}) \tag{5.12}$$

$$\frac{\partial c}{\partial t} + \mathbf{u}\cdot\nabla c - \mathcal{D}\nabla^2 c = -a\, c\, \exp(-\frac{\Delta E}{\hat{R}T}), \tag{5.13}$$

with initial conditions

$$\begin{aligned} T(x, y, 0) &= \tilde{h}_1(x, y) \\ c(x, y, 0) &= \tilde{h}_2(x, y), \end{aligned} \tag{5.14}$$

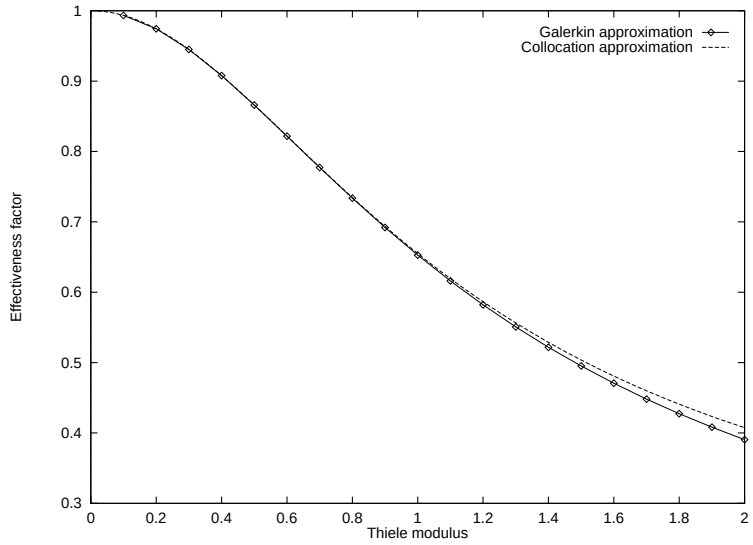

Figure 5.1: Effectiveness factor as a function of Thiele modulus for collocation method and Galerkin method.

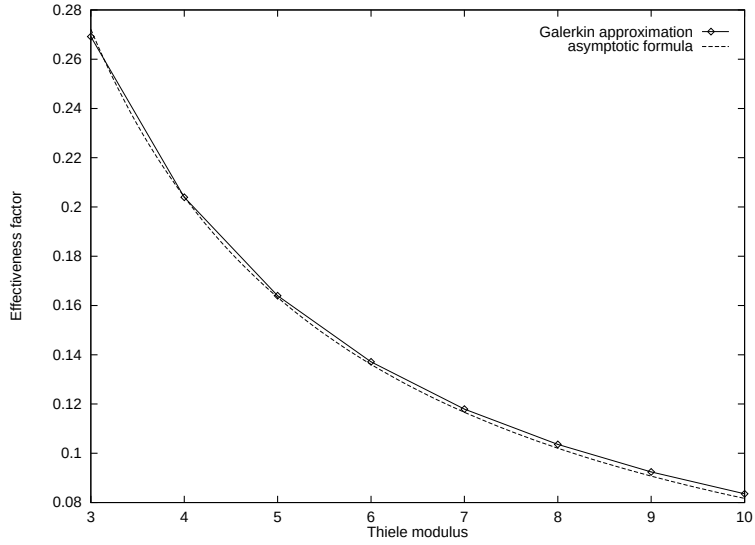

Figure 5.2: Effectiveness factor as a function of Thiele modulus for the asymptotic formula and Galerkin method.

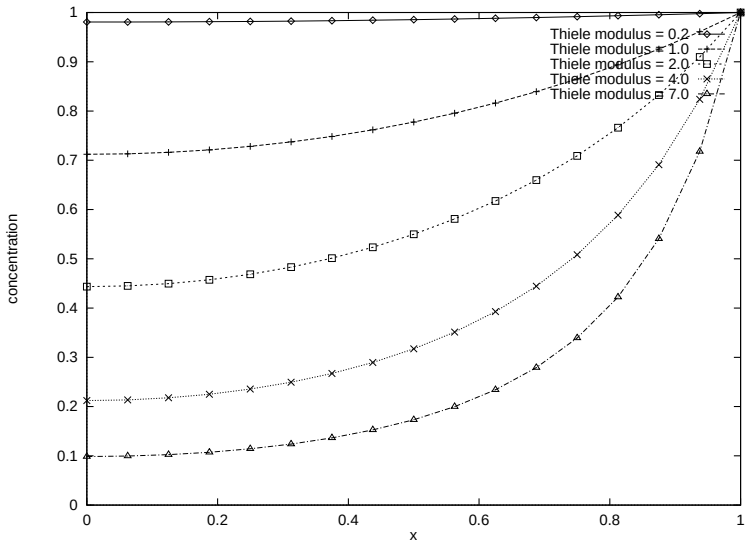

Figure 5.3: Steady-state solution in catalyst for $\phi = 0.2$, 1.0, 2.0, 4.0 and 7.0.

and boundary conditions

$$\begin{aligned} \nabla T \cdot \mathbf{n} &= \nabla c \cdot \mathbf{n} = 0 && \text{on } \partial\Omega_1 \\ -k\nabla T \cdot \mathbf{n} &= h_g(T - \tilde{T}) && \text{on } \partial\Omega_2 \\ -\mathcal{D}\nabla c \cdot \mathbf{n} &= k_g(c - \tilde{c}) && \text{on } \partial\Omega_2, \end{aligned} \tag{5.15}$$

where ρ is the density, c_p is the specific heat, k is the thermal conductivity, $\mathcal{D}$ is the diffusivity, h_g is the heat transfer coefficient, k_g is the mass transfer coefficient, $\mathbf{n}$ is the unit outward normal, and $\partial\Omega = \partial\Omega_1 \cup \partial\Omega_2$ is the boundary of the domain.

The equations can be scaled as follows: $x^* = \frac{x}{L}$, $y^* = \frac{y}{L}$, $u^* = u\frac{t_s}{L}$, $v^* = v\frac{t_s}{L}$, $c^* = \frac{c}{c_0}$, $T^* = \frac{T}{T_0}$, and $t^* = \frac{t}{t_s}$. Substituting these relations into (5.12), (5.13), (5.14) and (5.15), we obtain the dimensionless unsteady equations for the nonisothermal problem

$$\frac{\partial T}{\partial t} + \mathbf{u} \cdot \nabla T - \frac{1}{M_1}\nabla^2 T = \frac{\phi^2 c\beta}{M_1} \exp(\gamma(1 - \frac{1}{T})) \tag{5.16}$$

$$\frac{\partial c}{\partial t} + \mathbf{u} \cdot \nabla c - \frac{1}{M_2}\nabla^2 c = -\frac{\phi^2 c}{M_2} \exp(\gamma(1 - \frac{1}{T})), \tag{5.17}$$

with initial conditions

$$\begin{aligned} T(x, y, 0) &= h_1(x, y) \\ c(x, y, 0) &= h_2(x, y), \end{aligned} \tag{5.18}$$

and boundary conditions

$$\begin{aligned} \nabla T \cdot \mathbf{n} &= \nabla c \cdot \mathbf{n} = 0 && \text{on } \partial\Omega_1 \\ -\nabla T \cdot \mathbf{n} &= \frac{Nu}{2}(T - g_1(t)) && \text{on } \partial\Omega_2 \\ -\nabla c \cdot \mathbf{n} &= \frac{Sh}{2}(c - g_2(t)) && \text{on } \partial\Omega_2, \end{aligned} \tag{5.19}$$

where we drop the superscript * for simplicity, $M_1 = \rho c_p L^2/kt_s$, $M_2 = L^2/\mathcal{D}t_s$, $Nu = h_g 2L/\mathcal{D}$ is the Nusselt number, $Sh = k_g 2L/\mathcal{D}$ is the Sherwood number, $\phi = \sqrt{k_0 L^2/\mathcal{D}}$ is the Thiele modulus, and $\Omega = [0,1] \times [0,1]$ is the dimensionless section. Here $k_0 = a\exp(-\gamma)$. The dimensionless variables γ and β are defined as

$$\begin{aligned} \gamma &= \frac{\Delta E}{\hat{R}T_0}, \\ \beta &= \frac{(-\Delta H_R)c_0\mathcal{D}}{kT_0}, \end{aligned}$$

where $-\Delta H_R$ is the heat of reaction.

5.2.2 Nonisothermal Reaction on a Catalyst Section

First we solve the steady-state nonisothermal case under conditions in which the Nusselt and Sherwood numbers are very large [33]. The boundary conditions are

$$\begin{aligned} \nabla T \cdot \mathbf{n} &= \nabla c \cdot \mathbf{n} = 0 && \text{on } \partial\Omega_1 \\ T &= 1.1 && \text{on } \partial\Omega_2 \\ c &= 1.0 && \text{on } \partial\Omega_2 \end{aligned}$$

where $\partial\Omega_2$ is the right side of the unit square Ω, and $\partial\Omega_1 = \partial\Omega - \partial\Omega_2$. The functions h_1 and h_2 in (5.18) defining the initial conditions are

$$h_1(x,y) = h_2(x,y) = 1 + sin(\pi x)sin(\pi y).$$

The velocity field is given by the numerical solution of the Stokes flow [50, 64, 14], defined by the transient Navier-Stokes equations (2.7) and (2.8) subject to prescribed boundary conditions (2.14). The analytic solution for this problem is defined by the smooth velocity components

$$\begin{aligned} u(x,y) &= 100x^2(1-x)^2(2y - 6y^2 + 4y^3) \\ v(x,y) &= 100y^2(1-y)^2(-2x + 6x^2 - 4x^3) \end{aligned}$$

and the pressure field is $p(x,y) = 100(x^2 - y^2)$. The steady-state solution is obtained when the velocity field at two different timesteps reaches a difference less than an

input tolerance. The viscosity is $\nu = 0.01$, and we take a penalty parameter of $\epsilon = 10^{-8}$. This velocity field is divergence free and satisfies the no-slip condition $\mathbf{u} = 0$ on the entire boundary of the square $\partial\Omega$. To find the velocity field we use biquadratic basis functions in a 4×4 grid with 2×2 point integration of the penalty term. Figure 5.4 shows the velocity for the Stokes problem.

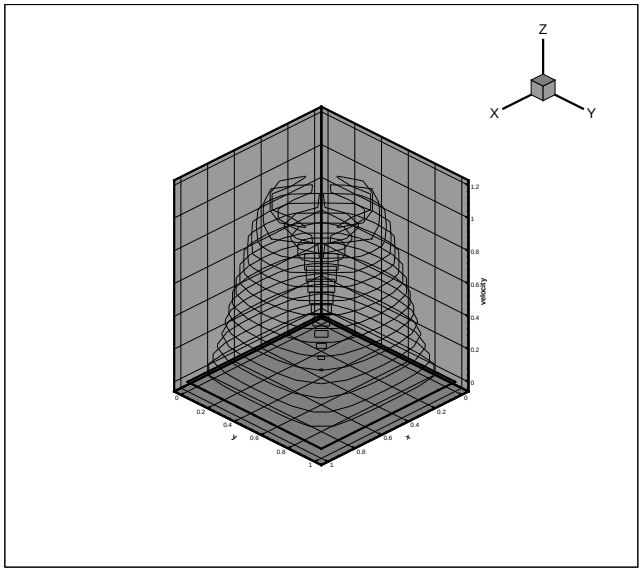

Figure 5.4: Velocity for the Stokes flow.

Here, the approximate solution for the Stokes problem is calculated and the velocities are substituted into the transport equations, which are solved for concentration and temperature. We calculate the steady-state approximate solution for the Thiele modulus $\phi = 0.8$, $\beta = 0.6$, $\gamma = 20$, $M_1 = 176$, $M_2 = 199$, and a grid with 8×8 bilinear elements. We assume that the steady-state occurs when the following condition is satisfied

$$\frac{\|(\mathbf{T}^{m+1} - \mathbf{T}^m) + (\mathbf{c}^{m+1} - \mathbf{c}^m)\|}{\|\mathbf{T}^{m+1} + \mathbf{c}^{m+1}\|} < \tau$$

where m denotes the timestep index and $\|\cdot\|$ denotes Euclidean norm. The initial time step size is 10^{-3}, and the minimum and maximum time step sizes allowed are 10^{-3} and 10, respectively. A tolerance $\tau = 10^{-4}$ was supplied for changes in nodal temperature and concentration. We need to start with this small timestep to obtain convergence of Newton's method in the transport equation.

We perform parametric studies of the PID controller for values around those used by Gustafsson et al. [39] and also by Coutinho and Alves [24]. We choose values of k_P ranging from 0.03 to 0.20, k_I from 0.03 to 0.40, and k_D from 0.003 to 0.02. We also study the case where $k_P = k_D = 0$. Table 5.1 shows for different values of

the PID parameters the number of time iterations, $ntstep$, the number of rejected steps, $nrejec$, the number of Newton iterations, $newt$, and the computational effort, c_{effort}, defined as $newt$ divided by the number Newton iterations obtained using a fixed timestep size of 10^{-3}. We need about 800 Newton iterations to obtain the solution applying the PID control, in contrast with 2998 Newton iterations (case 10) when a fixed timestep is used. We have in this example a 3.75 times improvement in the computational effort to compute the solution within the same accuracy.

case	k_P, k_I, k_D	$ntstep$	$nrejec$	$newt$	c_{effort}
1	0.075 0.175 0.01	240	7	800	0.27
2	0.1 0.3 0.015	232	11	792	0.26
3	0.05 0.05 0.005	282	1	897	0.30
4	0.1 0.16 0.011	242	7	807	0.27
5	0.06 0.13 0.008	247	6	819	0.27
6	0.08 0.216 0.0116	237	9	800	0.27
7	0.2 0.4 0.02	229	14	791	0.26
8	0.03 0.03 0.003	315	0	981	0.33
9	0.0 0.175 0.0	241	8	807	0.27
10	No Control	1101	0	2998	1
11	Winget & Hughes	264	8	876	0.29

Table 5.1: Results for the PID timestep controller and Winget and Hughes approach

The PID control is robust since the number of Newton iterations does not change much for different choices of PID parameters. We can also observe that the number of rejected timesteps is relatively small. The results for the Winget and Hughes approach [79] are presented in case 11. The PID controller finds the steady-state solution a little faster than the Winget and Hughes approach. Figure 5.5 and 5.6 show respectively the timestep size against time for case 1 and the Winget and Hughes approach. We observe that the PID control produces a very smooth curve, while in contrast, the Winget and Hughes approach yields a curve with several steps. The initial temperature profile and the steady state solution are shown in Figure 5.7. Note that all the steady-state solutions are indistinguishable.

Next we solve the unsteady problem (5.16), (5.17), (5.18) and (5.19) with $M_1 = 176$, $M_2 = 199$, $Nu = 55.3$, $Sh = 66.5$, $\gamma = 20$, $\beta = 0.6$, $\phi = 0.8$, $g_1(x) = 1.1$ and $g_2(x) = 1.0$. The velocity field is the same calculated in the steady-state problem (Figure 5.4). The approximate solutions are calculated using a grid with 8×8 bilinear elements. We first obtained the approximate solution for a constant timestep size of $\Delta t = 0.05$. Figure 5.8 shows the transient temperature distribution in a catalyst

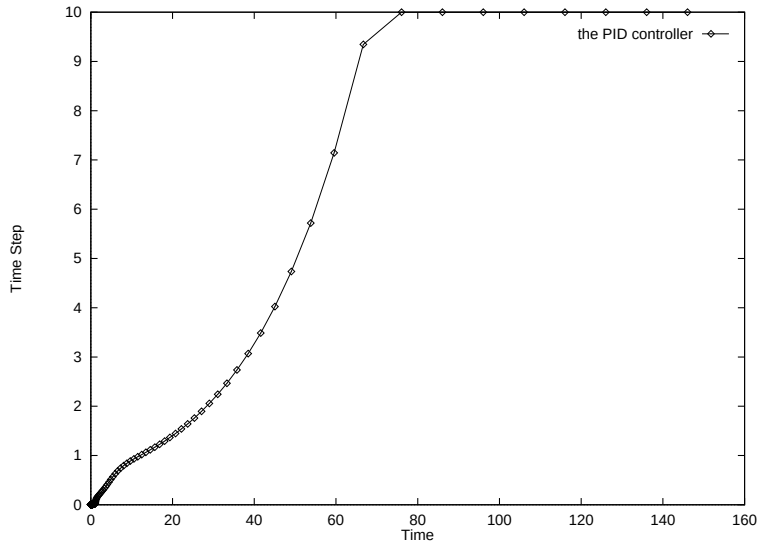

Figure 5.5: Timestep variation using the PID controller for case 1 (steady-state problem).

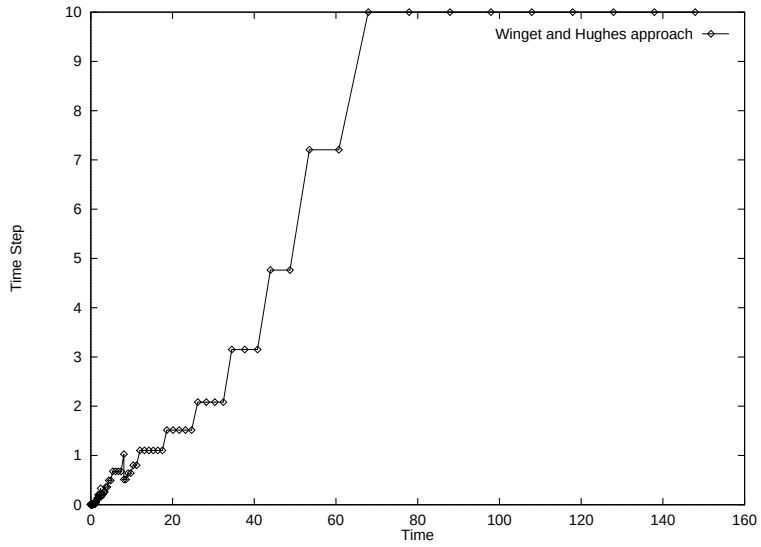

Figure 5.6: Timestep variation using Winget and Hughes approach (steady state problem).

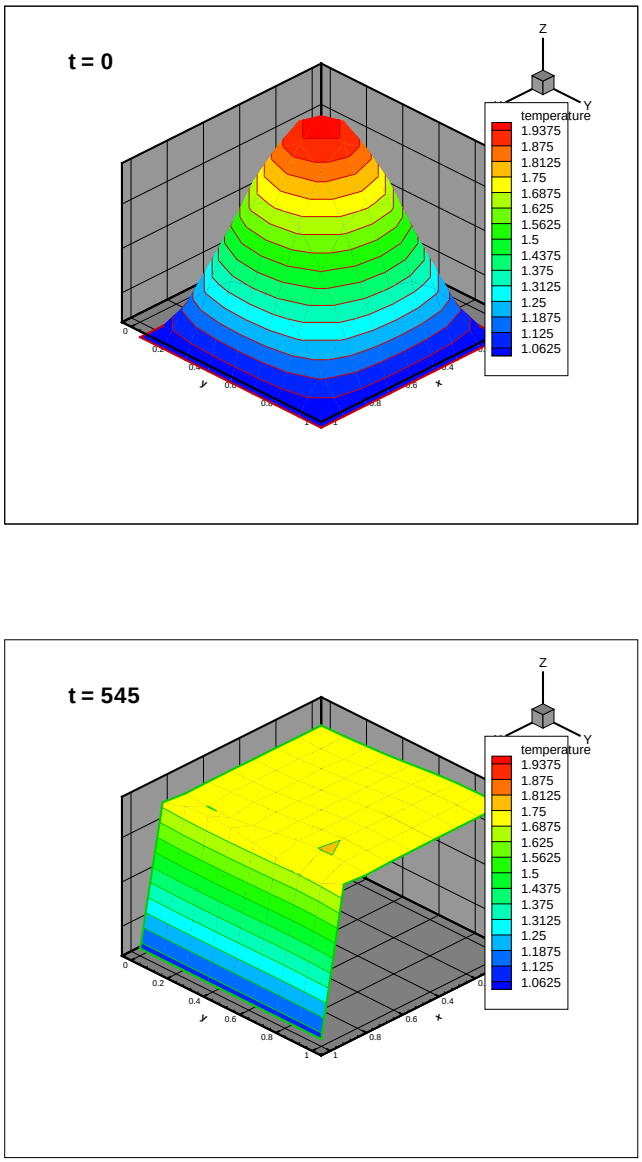

Figure 5.7: Initial temperature profile and steady-state solution using bilinear elements on a 8×8 grid ($\phi = 0.8$).

section at times t = 0, 1, 5, 10 and 20.

For a fixed time equal to 20, we compare approximate solutions using the PID controller and Winget and Hughes approach. We start with a timestep size of 0.05, and we allow minimum and maximum time steps of 0.05 and 5, respectively. The solutions are obtained with a tolerance of 10^{-6} for the changes in nodal temperature and concentration. The PID parameters are $k_P = 0.075$, $k_I = 0.175$ and $k_D = 0.01$.

Table 5.2 shows the results for each case studied. We obtain the solution with 423 Newton iterations using the PID controller, and we need 1223 Newton iterations with a fixed timestep of 0.05. Thus, we have obtained this solution 2.89 times faster with no accuracy loss. Here we also obtain the solution using the PID controller a little faster than using Winget and Hughes approach. Figure 5.9 and 5.10 show the timestep size against time for the PID controller and Winget and Hughes approach, respectively. Observe that the PID control produces a very smooth curve, while the Winget and Hughes approach yields a curve with several steps.

case	$ntstep$	$nrejec$	$newt$	c_{effort}
No Control	400	0	1223	1
PID Control	104	1	423	0.34
Winget&Hughes	112	1	433	0.35

Table 5.2: Results for the transient catalyst problem with timestep control and Winget and Hughes approach.

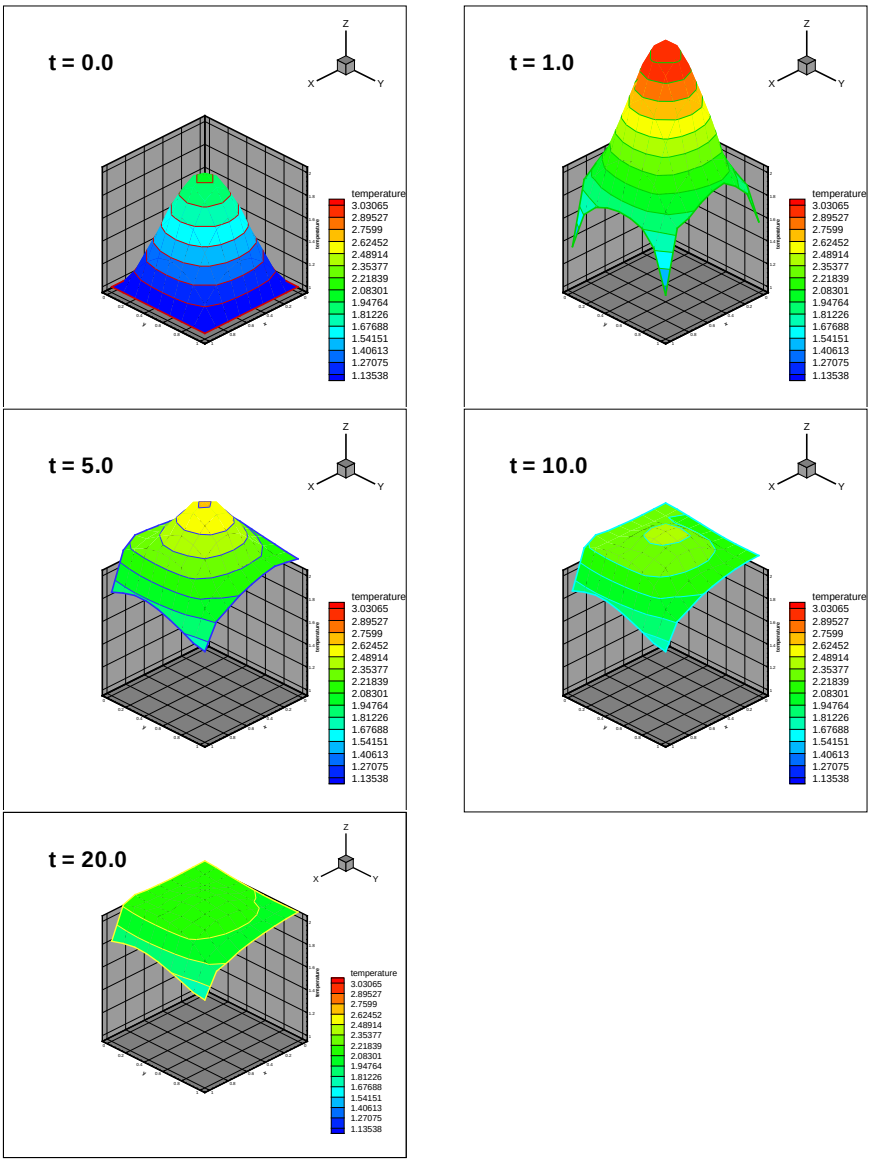

Figure 5.8: Evolution of temperature solution using bilinear elements on a 8×8 grid

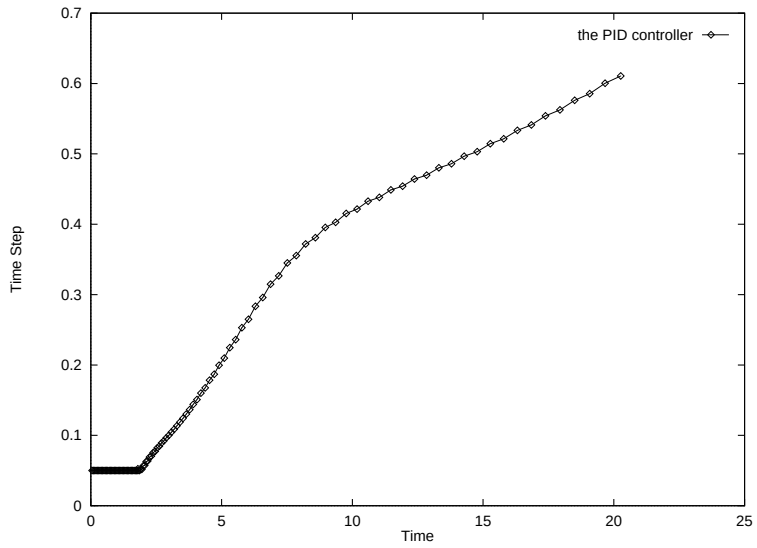

Figure 5.9: Timestep variation using the PID controller (transient problem).

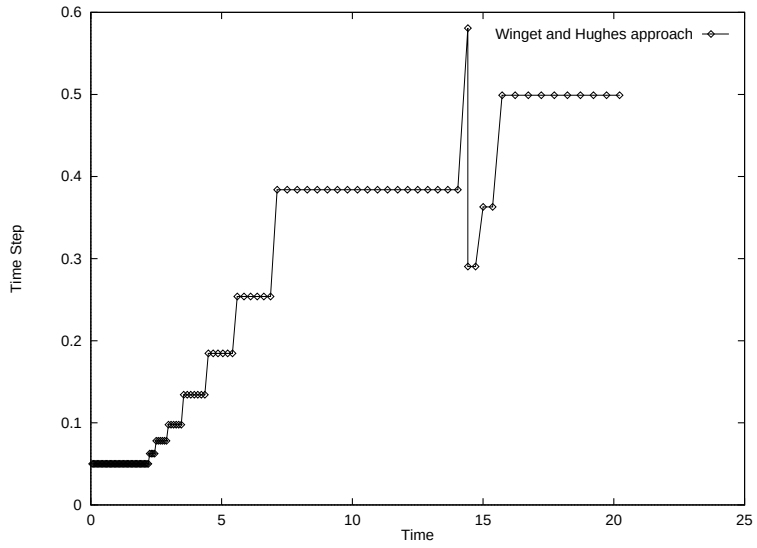

Figure 5.10: Timestep variation using Winget and Hughes approach (transient problem).

Chapter 6

Rayleigh-Benard-Marangoni Problems

The objective of this chapter is to compare the efficiency of Control 1 and Control 2 with the scheme given by Winget and Hughes in [79]. In particular, we want to study the performance of the controllers to solve Rayleigh-Benard-Marangoni problems. We perform numerical experiments for different parameters of Rayleigh-Benard and Rayleigh-Benard-Marangoni flows and compare our results with those found in the literature.

6.1 Dimensionless Equations

Natural convection of an incompressible fluid can be driven by buoyancy forces due to temperature gradients and thermocapillary forces caused by gradients in the surface tension [6, 18, 29, 80]. When buoyancy is the dominant component in driving the flow, they are termed Rayleigh-Benard flows. When both buoyancy and thermocapillary effects provide the dominant forces driving the flow, the associated coupled flow and transport problem is termed the Rayleigh-Benard-Marangoni problem. We are particularly interested in the interaction of buoyancy and thermocapillary forces, and their effects in a microgravity environment where buoyancy is small. However, the work is equally important for thin fluid layers in a normal gravity environment.

The effect of buoyancy is included as a temperature dependent body force term in the momentum equations by means of the Boussinesq approximation [38]. The applied temperature field induces a surface tension equivalent to the application of a shear stress at the horizontal free surface. The velocity field enters the convective term in the heat transfer equation. The equations describing Rayleigh-Benard-Marangoni flows are the coupled Navier Stokes equations for viscous flow of an

incompressible fluid and the heat transfer equation,

$$\frac{\partial \mathbf{u}}{\partial t} + \mathbf{u} \cdot \nabla \mathbf{u} - \nu \nabla^2 \mathbf{u} + \frac{1}{\rho} \boldsymbol{\nabla} p = \beta_T (T - T_0) \mathbf{g} \quad \text{in } \Omega \times I \tag{6.1}$$

$$\boldsymbol{\nabla} \cdot \mathbf{u} = 0 \quad \text{in } \Omega \times I \tag{6.2}$$

$$\rho c_p \frac{\partial T}{\partial t} + \rho c_p \mathbf{u} \cdot \nabla T - \nabla \cdot (k \nabla T) = 0 \quad \text{in } \Omega \times I \tag{6.3}$$

where $\mathbf{u}$ is the velocity, p is the pressure, Ω is the flow domain, T is the temperature, T_0 is the reference temperature, ν is the kinematic viscosity, ρ is the density, β_T is the thermal coefficient, $\mathbf{g}$ is the gravity vector, c_p is the specific heat, k is the thermal conductivity, and $I = [0, \bar{t}]$ is the time interval.

We assume that there is no slip at the solid walls $\partial\Omega_1$, i.e., $\mathbf{u} = \mathbf{u_w}$ where $\mathbf{u_w}$ is the specified wall boundary velocity. Temperature, flux or mixed thermal boundary conditions may be applied. The Marangoni problem involves a shear stress boundary in the free surface $\partial\Omega_2$. The surface stress, τ_{fb}, tangent to the free boundary is equal to the gradient in the surface tension σ,

$$\tau_{fb} = \mu \, \nabla u \cdot \mathbf{n} = \nabla \sigma \cdot \tau = -\sigma_T \, \nabla T \cdot \tau \tag{6.4}$$

where $\sigma_T = \frac{\partial \sigma}{\partial T}$ is determined empirically for a given fluid and τ is a unit tangent vector. We assume here that σ varies linearly with T, so σ_T is a constant for a given fluid.

The equations (6.1), (6.2) and (6.3) are scaled as follows: $x^* = \frac{x}{L}$, $y^* = \frac{y}{L}$, $t^* = \frac{t\nu}{L^2}$, $u^* = \frac{uL}{\nu}$, $v^* = \frac{vL}{\nu}$, $T^* = \frac{T - T_0}{\Delta T}$ and $p^* = (\frac{p}{\rho})\frac{L^2}{\nu^2}$ where ΔT is a scaling factor. Substituting these relations into (6.1), (6.2) and (6.3), we obtain the dimensionless formulation of the equations

$$\frac{\partial \mathbf{u}}{\partial t} + \mathbf{u} \cdot \nabla \mathbf{u} - \nabla^2 \mathbf{u} + \boldsymbol{\nabla} p = \frac{Ra}{Pr} T \mathbf{g} \quad \text{in } \Omega \times I \tag{6.5}$$

$$\boldsymbol{\nabla} \cdot \mathbf{u} = 0 \quad \text{in } \Omega \times I \tag{6.6}$$

$$\frac{\partial T}{\partial t} + \mathbf{u} \cdot \nabla T - \frac{1}{Pr} \nabla^2 T = 0 \quad \text{in } \Omega \times I \tag{6.7}$$

where we dropped the superscript * for simplicity. The non-dimensional constants are: the Rayleigh number $Ra = \frac{\beta_T \Delta T g L^3}{\nu \alpha}$ and the Prandtl number $Pr = \frac{\nu}{\alpha}$, where $\alpha = \frac{k}{\rho c_p}$ is the thermal diffusivity. The boundary condition on the free surface (6.4) becomes

$$\nabla u \cdot \mathbf{n} = -\frac{Ma}{Pr} \, \nabla T \cdot \tau \tag{6.8}$$

where $Ma = \frac{\sigma_T \Delta T L}{\rho \nu \alpha}$ is the Marangoni number. Equations (6.5), (6.6) and (6.7) constitute a coupled system of equations to be solved for velocity, pressure and temperature. The finite element formulation and the coupled algorithm to solve the problem are described in Chapter 2.

6.2 Rayleigh-Benard Flows

The classic Rayleigh-Benard problem corresponds to flow between two horizontal plates where the top plate is held at a constant (cool) temperature and the bottom plate is held at a higher constant temperature. At critical Rayleigh number the heated fluid near the bottom plate becomes less dense and begins rise while the (cool) fluid near the top is more dense and descends. This leads to circular convection cells in two dimensions. If the plate is removed from the upper surface, then the thermocapillary surface traction due to temperature gradients on the free surface also becomes important. This is a direct consequence of the dependence of surface tension on temperature (Marangoni effect). Now, both buoyancy and thermocapillary effects may be important in driving the flow for this classical Rayleigh-Benard-Marangoni problem.

The first case studied involves natural convection in a unit square $\Omega = [0,1]\times[0,1]$ with temperatures $T = 1$, $T = 0$ on the left and right walls respectively, adiabatic top and bottom wall (no free surface), with $Pr = 0.71$ and different Rayleigh numbers, Ra, of 10^3, 10^4 and 10^5. The computed Nusselt number at the left wall,

$$Nu_0 = \int_0^1 q dy, \tag{6.9}$$

where q is the heat flux, and the stream function at the midpoint, ψ_{mid}, are compared to benchmark computations given by Davis in [31, 30]. The benchmark case reports the quantities to four significant figures, and the reported accuracy is within 1 per cent for all Rayleigh numbers. Davis and Carey in [27] obtain parallel multilevel solution of this problem with superior accuracy due to high-p finite element simulations. We compare approximate solutions using fixed timestep sizes, Control 1, Control 2, the Winget and Hughes approach (W&H) and the benchmark solution, as shown in Table 6.1.

The approximate velocities and temperature are calculated using 9-node isoparametric quadrilaterals elements in a uniform mesh of 16×16 elements at $Ra = 10^3, 10^4$ and 32×32 elements at $Ra = 10^5$. The initial timestep size in all cases is chosen to allow convergence of the successive iterations at the beginning of the process. That is, if we start with a timestep size greater than the initial timesteps chosen here, the successive approximation iterations failed to converge after a few time steps. We start with a timestep size of 0.01 at $Ra = 10^3, 10^4$ and 0.001 at $Ra = 10^5$. We assume that the steady-state occurs when the kinetic energy at two different time steps reaches a relative difference less than a given tolerance, tol_{st}. We establish

that the steady-state occurs when $tol_{st} = 10^{-4}$ at $Ra = 10^3$ and $tol_{st} = 10^{-3}$ at $Ra = 10^4, 10^5$.

Table 6.1: Comparison of specific results to benchmark case

	Fixed Δt		Control 1		Control 2		W&H		Benchmark	
Ra	Nu_0	ψ_{mid}	Nu_0	ψ_{mid}	Nu_0	ψ_{mid}	Nu_0	ψ_{mid}	Nu_0	ψ_{mid}
10^3	1.118	1.175	1.119	1.175	1.117	1.174	1.119	1.175	1.117	1.174
10^4	2.255	5.067	2.236	5.077	2.246	5.064	2.249	5.066	2.238	5.071
10^5	4.550	9.134	4.518	9.036	4.553	9.120	4.503	8.925	4.509	9.111

Table 6.2 contains the percentage relative differences between the values calculated by each case studied and the corresponding values of the benchmark solution for different Rayleigh numbers. The results are in good agreement for all cases, with percentage errors no more than 1% in all quantities for Control 1 and Control 2, see Table 6.2. However, observe that the differences increase as Ra increases due to the growing difficulty of the problem. The Winget and Hughes approach also produces good results with percentage errors no more than 2% in all quantities. The stream function contours and temperature contours for $Ra = 10^3$, $Ra = 10^4$ and $Ra = 10^5$ are shown in Figure 6.1 and Figure 6.2, respectively. The contour values are the same as in Davis [31] and show excellent agreement with his results.

Table 6.2: Percentage errors

	Fixed Δt		Control 1		Control 2		W&H	
Ra	Nu_0	ψ_{mid}	Nu_0	ψ_{mid}	Nu_0	ψ_{mid}	Nu_0	ψ_{mid}
10^3	0.1	0.1	0.2	0.1	0.0	0.0	0.2	0.1
10^4	0.8	0.1	0.1	0.1	0.4	0.1	0.5	0.1
10^5	0.9	0.3	0.2	0.8	1.0	0.1	0.1	2.0

Now we compare the computational effort to calculate the solution for each case studied. The computational effort is measured by the total number of successive approximations needed to calculate the velocity field using one of the approaches divided by the number of successive approximations obtained using a fixed timestep size. For each case, we calculate the number of time iterations, $ntstep$, the number of rejected steps, $nrejec$, the total number of successive approximations, nsa, and the computational effort, c_{effort}. The PID parameters in all cases are $k_p = 0.075$, $k_i = 0.175$ and $k_d = 0.01$ [75, 74, 71]. Since Control 2 uses the change in the kinetic

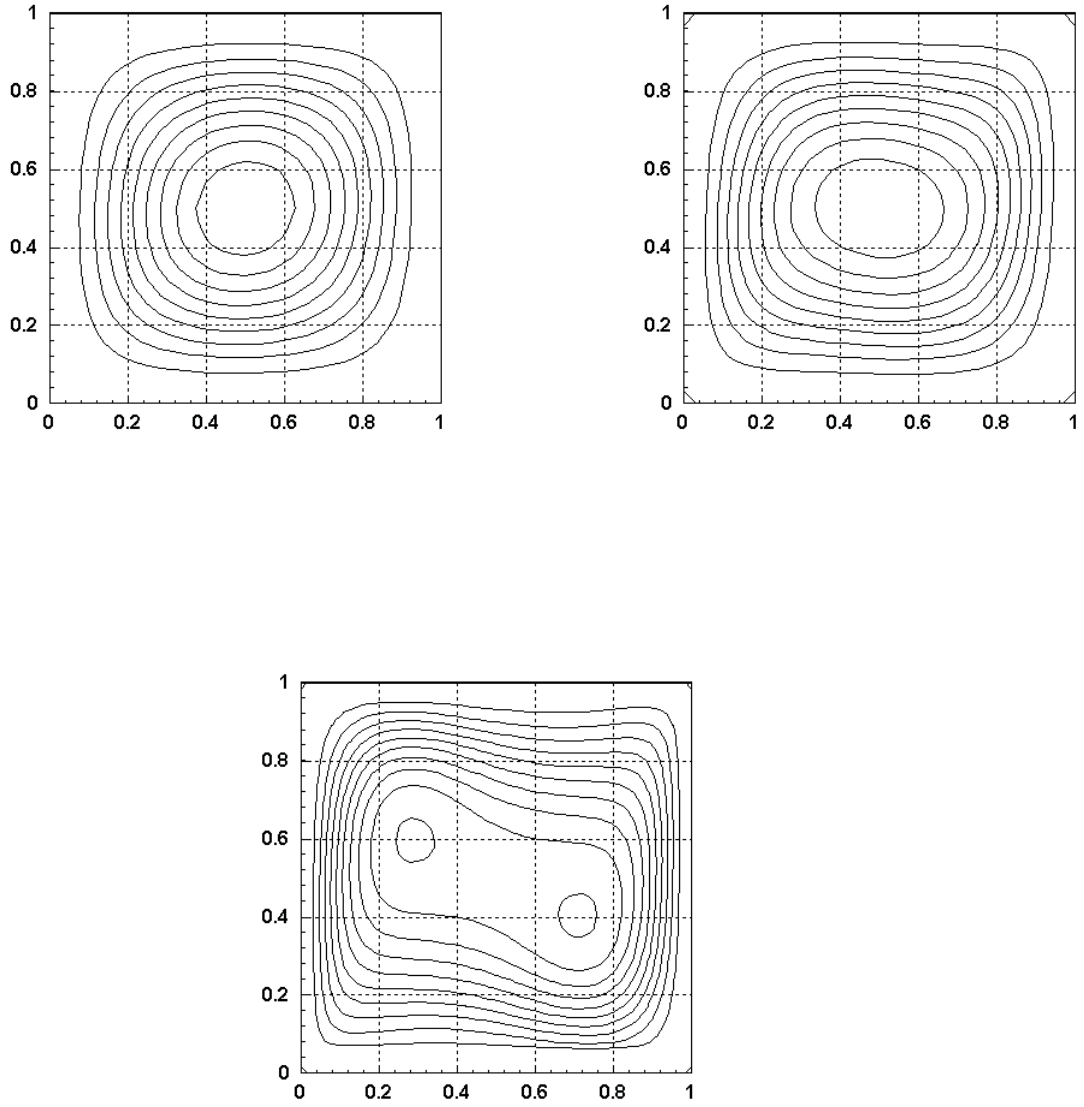

Figure 6.1: Stream functions contours for $Ra = 10^3$ (equally spaced (0.1174) between -1.0566 and 0), $Ra = 10^4$ (equally spaced (0.5071) between -4.5639 and 0) and $Ra = 10^5$ (equally spaced (0.9607) between -9.507 and 0).

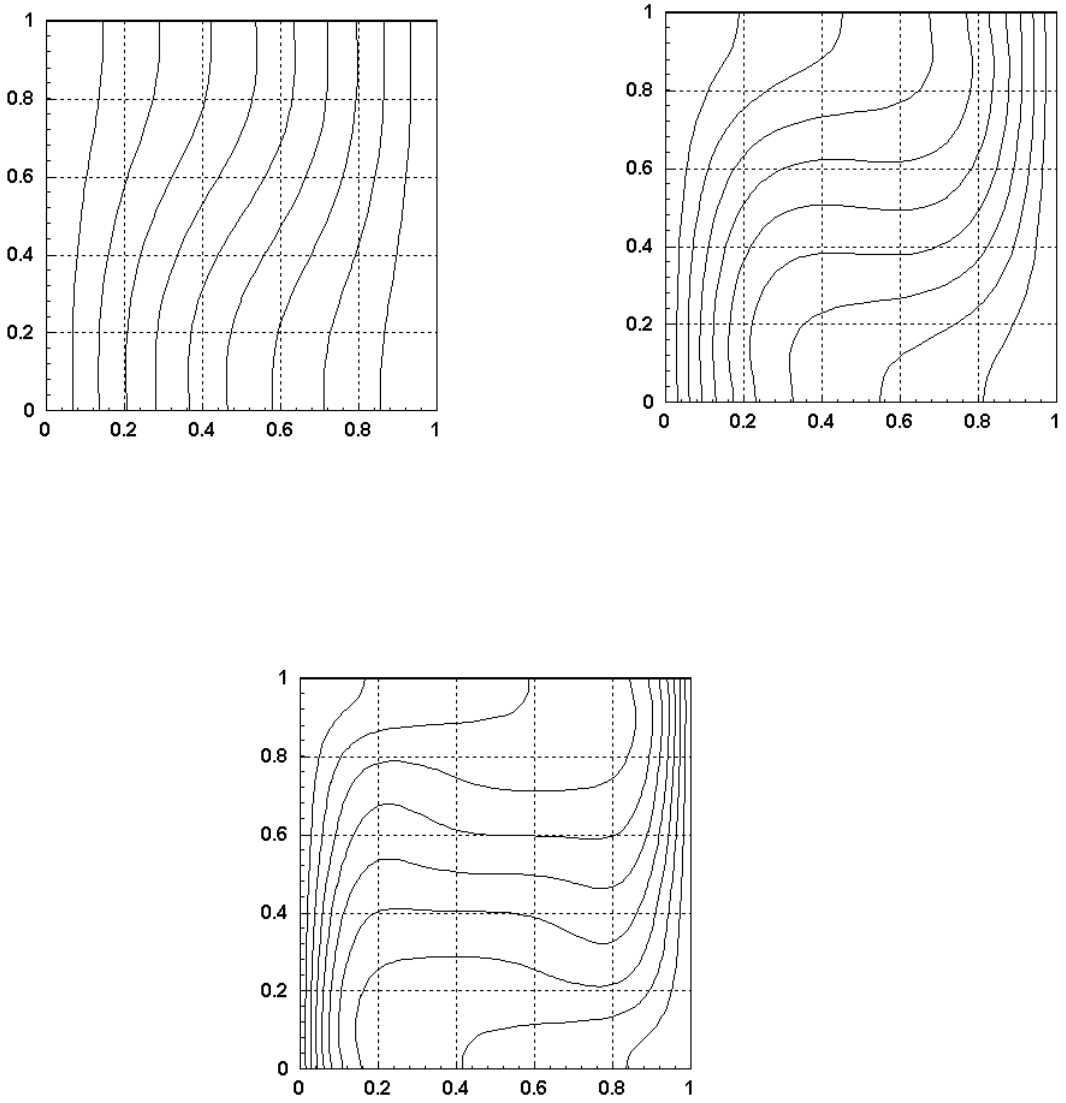

Figure 6.2: Temperature contours for $Ra = 10^3$, $Ra = 10^4$ and $Ra = 10^5$ (equally spaced (0.1) between 1 and 0).

energy to obtain the timestep size, we show in Figure 6.3 the nondimensional kinetic energy for $Ra = 10^3$, $Ra = 10^4$ and $Ra = 10^5$.

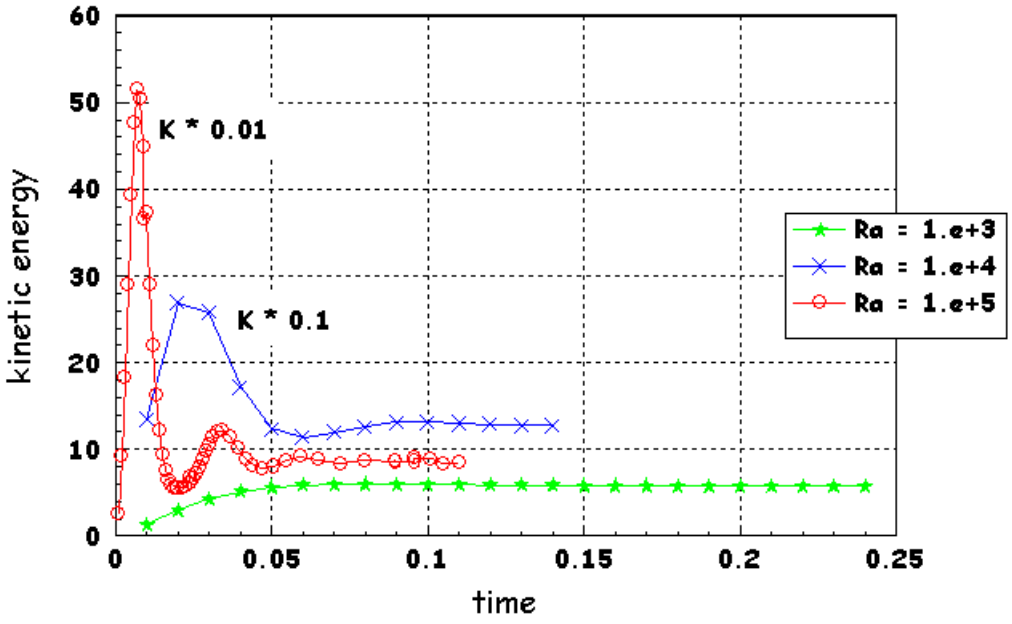

Figure 6.3: Nondimensional kinetic energy plotted as a function of time for $Ra = 10^3$, $Ra = 10^4$ and $Ra = 10^5$.

The results for $Ra = 10^3$ are shown in Table 6.3. We start with a minimum timestep size of 0.01, and we allow a maximum timestep size of 0.1. We define a tolerance of 0.1 for changes in nodal velocities and temperature. The tolerance corresponding to the normalized changes in kinetic energy is equal to one. The reference rate of convergence is equal to 0.2. We can observe in Table 6.3 that the number of successive approximations necessary to calculate the approximate solutions is reduced for all approaches. However, Control 2 presents the best results. We obtain the solution with 24 successive iterations using Control 2, and we need 64 iterations with the fixed timestep size. Thus, we are able to calculate the solution 2.4 times faster using Control 2 without any significant loss of accuracy. For Control 2, the choice of the timestep is dominated by the changes in the kinetic energy in all iterations.

Figure 6.4 shows the timestep size and the number of successive approximations against time using Control 1, Control 2 and the Winget and Hughes approach for $Ra = 10^3$. In this example, the kinetic energy is the most suitable parameter to choose the timestep, since Control 2 gives the best result. It is worthwhile noting also that Control 2 begins to act before any other approach and, after a few steps,

Table 6.3: Computational effort for the natural convection problem, $Ra = 10^3$.

$Ra = 10^3$	$ntstep$	$nrejec$	nsa	c_{effort}
Fixed Δt	24	0	58	1
Control 1	11	0	32	0.55
Control 2	8	0	24	0.41
Winget&Hughes	15	0	41	0.71

provides a timestep equal to the maximum stepsize allowed, 0.1.

Table 6.4 shows the results for $Ra = 10^4$. We start with a minimum timestep of 0.01, and we allow a maximum timestep size of 0.1. We define tolerances of 0.2, 0.1 and 0.5 for changes in nodal velocities, temperature and kinetic energy, respectively. The reference rate of convergence is equal to 0.19. Here we also improve efficiency for all approaches, reducing the number of successive approximations necessary to calculate the approximate solutions. Control 1 and Control 2 are equivalent in terms of efficiency. The choice of the timestep in Control 2 is dominated by the convergence rate of the successive iterations, with only two time iterations limited by the changes in the kinetic energy. Control 1, which is based on controlling accuracy, gives timestep sizes larger than the ones calculated by Control 2, see Figure 6.5.

Table 6.4: Computational effort for the natural convection problem, $Ra = 10^4$.

$Ra = 10^4$	$ntstep$	$nrejec$	nsa	c_{effort}
Fixed Δt	14	0	56	1
Control 1	10	0	47	0.84
Control 2	10	0	45	0.80
Winget&Hughes	12	0	52	0.93

Table 6.5 shows the results for $Ra = 10^5$. We start with a minimum timestep size of 0.001, and we allow a maximum timestep size of 0.1. We define a tolerance of 0.1 for changes in nodal velocities and temperature. The tolerance corresponding to the normalized changes in kinetic energy is equal to one. The reference rate of convergence is equal to 0.25. Now, Control 2 is dominated by the changes in the kinetic energy, with only 4 iterations calculated according to the convergence rate of the successive iterations. All approaches reduce the number of successive approximations to obtain the solution, but Control 2 gives the best result. The total number of successive approximations obtained by Control 1 can be reduced if we define large tolerances for changes in nodal velocities and temperature. However,

the results will loose accuracy, yielding errors greater than 1% as the case of the Winget and Hughes approach (see Table 6.2).

Table 6.5: Computational effort for the natural convection problem, $Ra = 10^5$.

$Ra = 10^5$	$ntstep$	$nrejec$	nsa	c_{effort}
Fixed Δt	108	0	363	1
Control 1	48	5	260	0.72
Control 2	39	0	189	0.52
Winget&Hughes	48	3	244	0.67

Figure 6.6 shows the timestep size and the number of successive approximations against time using Control 1, Control 2 and the Winget and Hughes approach for $Ra = 10^5$. Since the size of the timestep increases significantly when time progress for Control 1 and the Winget and Hughes approach, the number of successive iterations to obtain convergence of the nonlinear process at each corresponding time also increases. This fact is responsible for the larger number of successive iterations calculated by these two approaches when compared with Control 2.

In the second experiment the two horizontal walls are fixed at different temperatures. In the previous example involving lateral walls at different temperatures, even small temperature differences lead to a temperature-driven convection. In contrast with the configuration of the previous example, in this case the temperature difference must exceed a critical Rayleigh number value before any flow sets in. According to Bejan in [5], natural convection will develop only for Rayleigh numbers $Ra >\approx 1108$. Moreover, the influence of the lateral walls (carrying no slip conditions) produces three-dimensional effects, and hence the flow may be approximated as two-dimensional in only two cases: if the lateral walls are far enough apart that their effect may be neglected and if the depth of the horizontal walls is very small (Hele-Shaw flow).

We investigate the formation of Rayleigh-Benard cells in this example treating the flow in a two-dimensional simulation. We consider the flow in an air-filled rectangular container with aspect ratio 4:1 (length:width), insulated lateral walls, $Pr = 0.72$ and $Ra = 30000$. The temperatures on the bottom surface and top surface are $T = 1$ and $T = 0$, respectively. The approximate velocity and temperature are calculated using biquadratic shape functions with a grid of 32×8 elements, and the control algorithms for timestep selection. We consider the steady-state problem and the computed velocity field, streamlines and temperature contours are shown

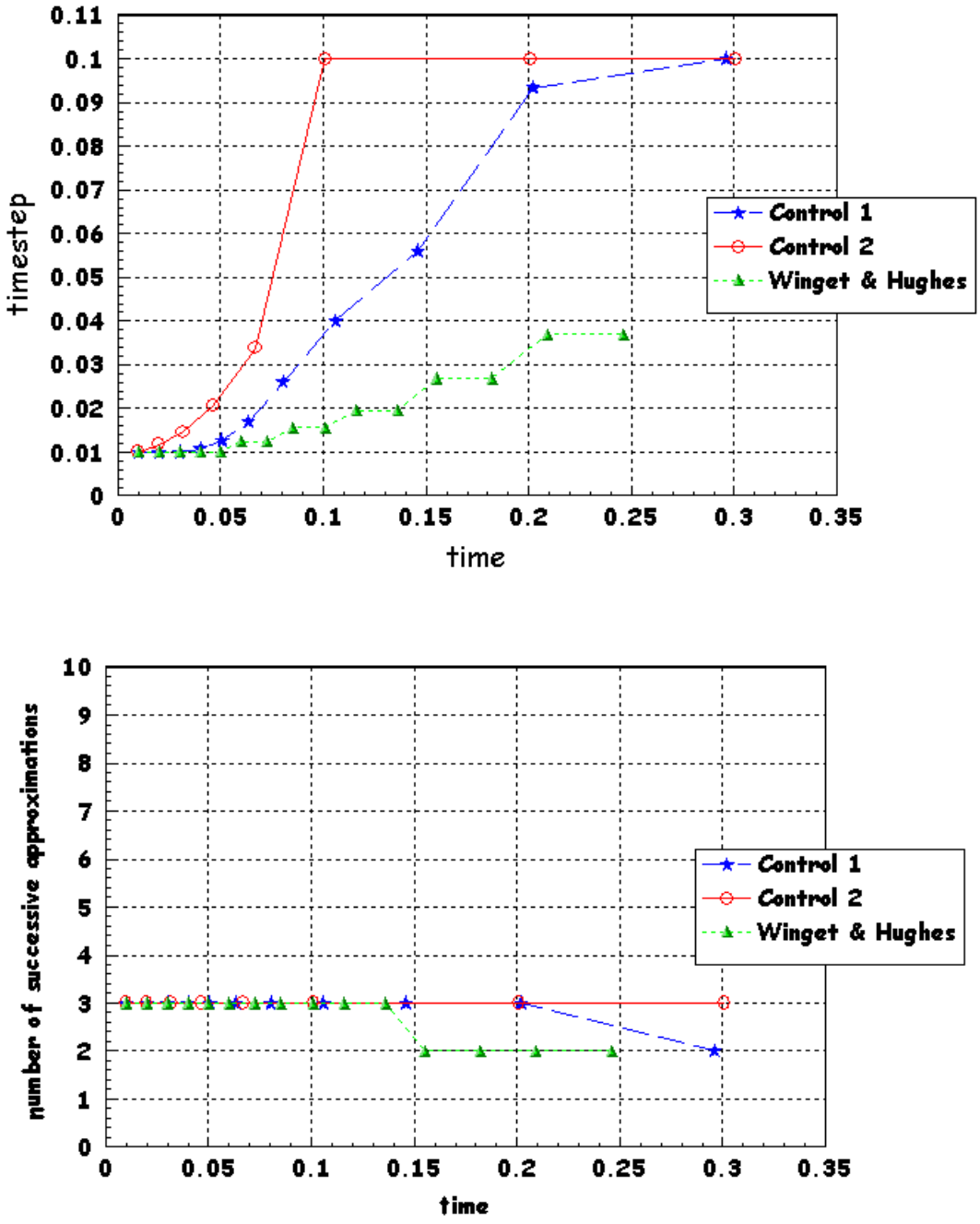

Figure 6.4: Timestep variation (top) and number of successive approximations (bottom) using Control 1, Control 2 and the Winget and Hughes approach for $Ra = 10^3$.

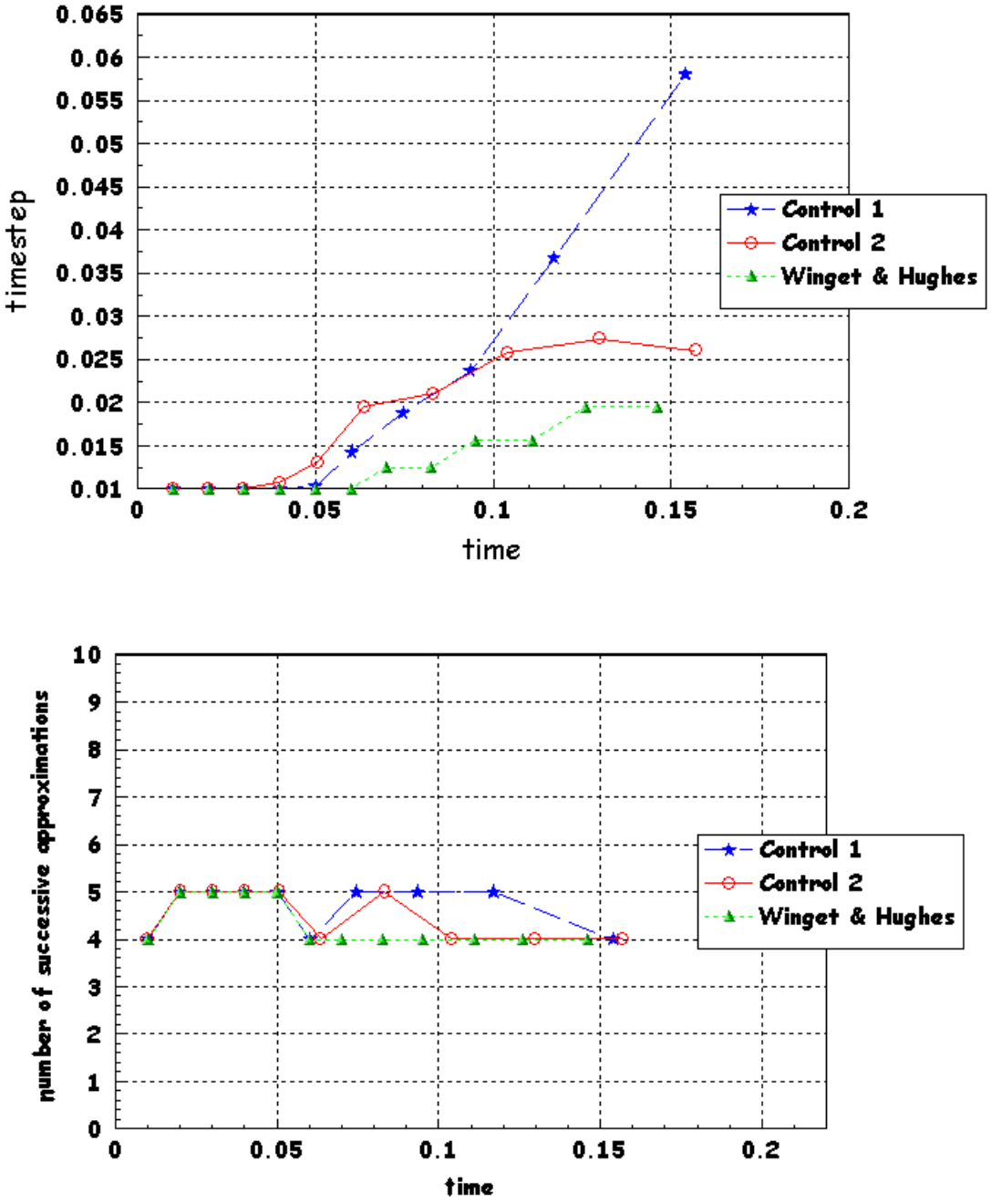

Figure 6.5: Timestep variation (top) and number of successive approximations (bottom) using Control 1, Control 2 and the Winget and Hughes approach for $Ra = 10^4$.

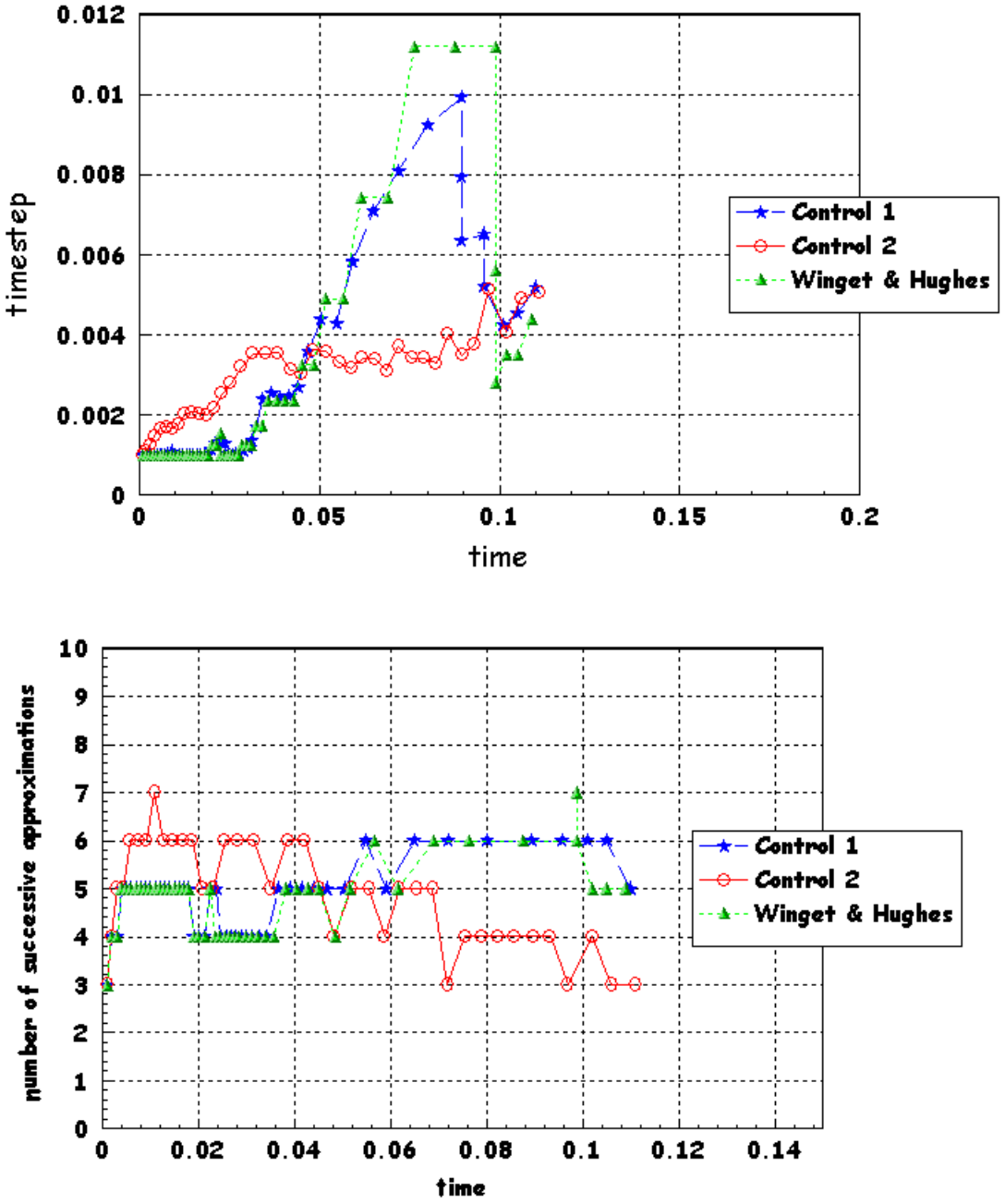

Figure 6.6: Timestep variation (top) and number of successive approximations (bottom) using Control 1, Control 2 and the Winget and Hughes approach for $Ra = 10^5$.

in Figure 6.7. There are six recirculation cells, and the results agree with those obtained by Griebel, Dornseifer and Neunhoeffer in [38].

Now, we assume that the steady-state is reached when $\|\mathbf{U}^n - \mathbf{U}^{n-1}\| < 3 \times 10^{-3} \|\mathbf{U}^n\|$ and $\|\mathbf{T}^n - \mathbf{T}^{n-1}\| < 10^{-3} \|\mathbf{T}^n\|$. We set a tolerance of 0.01 for changes in nodal velocities and temperature and 0.8 for changes in the kinetic energy. We start with a timestep size of 0.001, and we allow minimum and maximum time steps of 0.001 and 0.5, respectively. This starting timestep is the largest for which we obtained convergence in the successive iterations. The reference rate of convergence of nonlinear iterations is chosen equal to 0.35 in this example. The PID parameters are $k_p = 0.075$,$k_i = 0.175$ and $k_d = 0.01$. Table 6.6 shows the computational effort for this problem calculated for each case studied.

Table 6.6: Computational effort for the flow in a container with aspect ratio 4:1.

	$ntstep$	$nrejec$	nsa	c_{effort}
Fixed Δt	241	0	731	1
Control 1	192	0	643	0.88
Control 2	89	1	380	0.52
Winget&Hughes	193	0	644	0.88

As we can see in Table 6.6, we obtain the solutions with a reduced number of successive approximation iterations using all the controllers. However, Control 2 gives the smallest computational effort. With a fixed timestep size of 0.001 we need 731 iterations, and only 380 iterations when Control 2 is applied. Thus, the solution is obtained 1.9 times faster using Control 2. In this example, Control 1 and the approach used by Winget and Hughes are equivalents in terms of the computational effort. Figure 6.8 shows the timestep size against time and the number of successive approximation iterations using Control 1, Control 2 and the Winget and Hughes approach.

6.3 Rayleigh-Benard-Marangoni Flows

This numerical experiment involves buoyancy forces due to temperature gradients and thermocapillary forces caused by gradients in the surface tension. The objective is to compare pure buoyancy-driven flow with thermo-capillary-driven flow. The flow domain and boundary conditions correspond to those in the first example of the previous section ($T = 1$ and $T = 0$ on the left and right walls, respectively), except

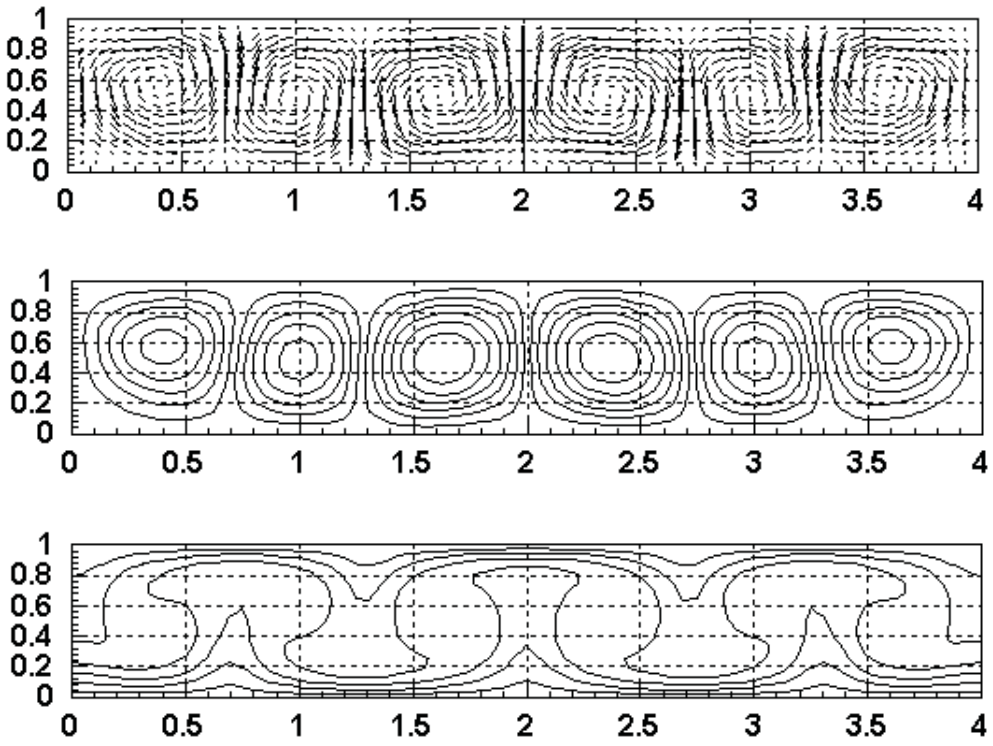

Figure 6.7: Vector field, streamlines, and temperature contours for the flow in a container with aspect ratio 4:1

that the top is now a flat free surface. The Rayleigh number is 10^3, the Prandtl number is $Pr = 0.71$, and the problem is solved at different Marangoni numbers Ma. The approximate steady-state velocities and temperature are calculated using biquadratic elements in a uniform mesh with size $h = \frac{1}{16}$. Here we assume that the steady-state occurs when $\|\mathbf{U}^{n+1} - \mathbf{U}^n\| < \tau_u \|\mathbf{U}^{n+1}\|$ and $\|\mathbf{T}^{n+1} - \mathbf{T}^n\| < \tau_T \|\mathbf{T}^{n+1}\|$, where n denotes the timestep index, $\|\cdot\|$ denotes Euclidean norm, and τ_u and τ_T are input tolerances.

First, we find solutions at $Ma = 1$, 100 and 1000 (see Figure 6.9). At $Ma = 1$, the effect of the surface tension is small and the streamlines are roughly circular. The solution is similar in structure to the classic buoyancy driven flow studied in the first example, Figure 6.1. At $Ma = 100$, the effect of the thermocapillary force at the free surface is more pronounced. The streamlines are concentrated near the top boundary. At $Ma = 1000$, the flow is being strongly driven at the top boundary as seen in similar experiments presented by Zebib, Homsy and Meiburg [80]. Second, we consider the case of a fluid where the surface tension acts in the direction contrary to the flow. This is the case for certain fluids when inpurities are presented, see McLay and Carey in [61]. Figure 6.10 shows the stream function

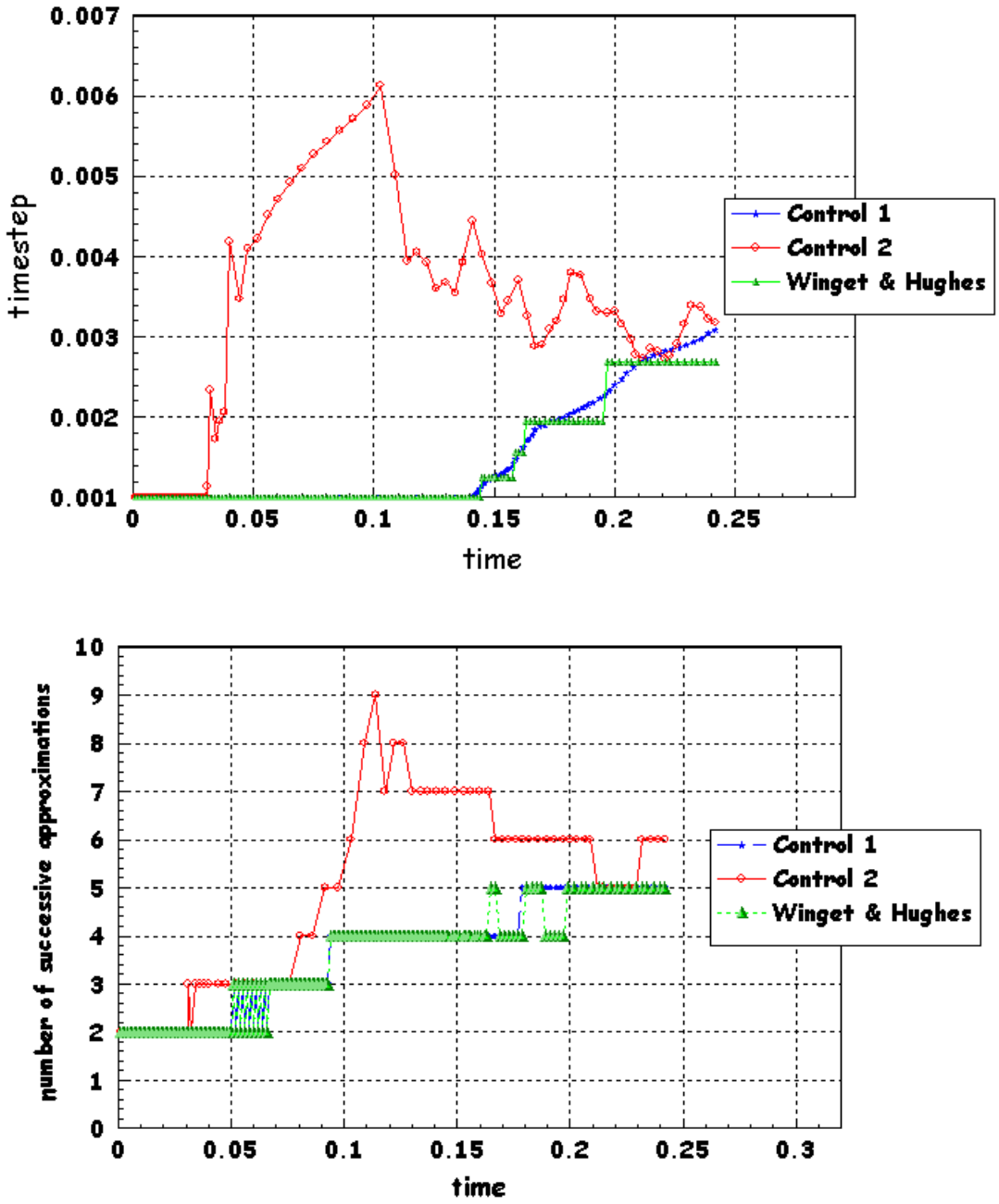

Figure 6.8: Timestep variation (top) and number of successive approximations (bottom) using Control 1, Control 2 and the Winget and Hughes approach for the flow in a container with aspect ratio 4:1.

contours for $Ma = -10$ and $Ma = -100$. The contours at $Ma = -10$ look similar to the solution at $Ma = 1$ due to the small thermocapillary effect. At $Ma = -100$, the surface tension effect is strong enough to reverse the flow on the top surface and two cells are formed.

To study the behavior of the PID timestep selection in the second problem, we select the case where $Ma = 100$. The steady-state solution is obtained at $\tau_u = 10^{-3}$ and $\tau_T = 10^{-4}$. We start with a minimum timestep size of 0.001, and we allow a maximum timestep of 0.1. Solutions are obtained with tolerances of 0.2 and 0.1 for changes in nodal velocities and temperature, respectively. The tolerance corresponding to the normalized changes in kinetic energy is equal to one. The reference rate of convergence is equal to 0.2. Figure 6.11 shows the time evolution of the nondimensional kinetic energy for $Pr = 0.71$, $Ra = 1000$ and $Ma = 100$. Note that the kinetic energy presents smooth oscillations, damped as the solution progresses towards the steady-state.

As we can see in Table 6.7, we obtain the solutions with 57 successive approximation iterations using Control 2. With a fixed timestep size of 0.001, we need 272 iterations. Thus, the solutions are obtained 4.8 times faster using Control 2. Here, the choice of the timestep in Control 2 is dominated by the changes in the kinetic energy, with only three time iterations limited by the changes in the convergence rate of the successive iterations. Figure 6.12 shows the timestep variation and the number of successive approximations against time using Control 1, Control 2 and the Winget and Hughes approach, respectively. We can observe that Control 1 yields a smoother sequence of time steps than the Winget and Hughes approach. However, these two approaches are equivalent in terms of efficiency. Control 2 calculates the solutions with the smallest computational effort.

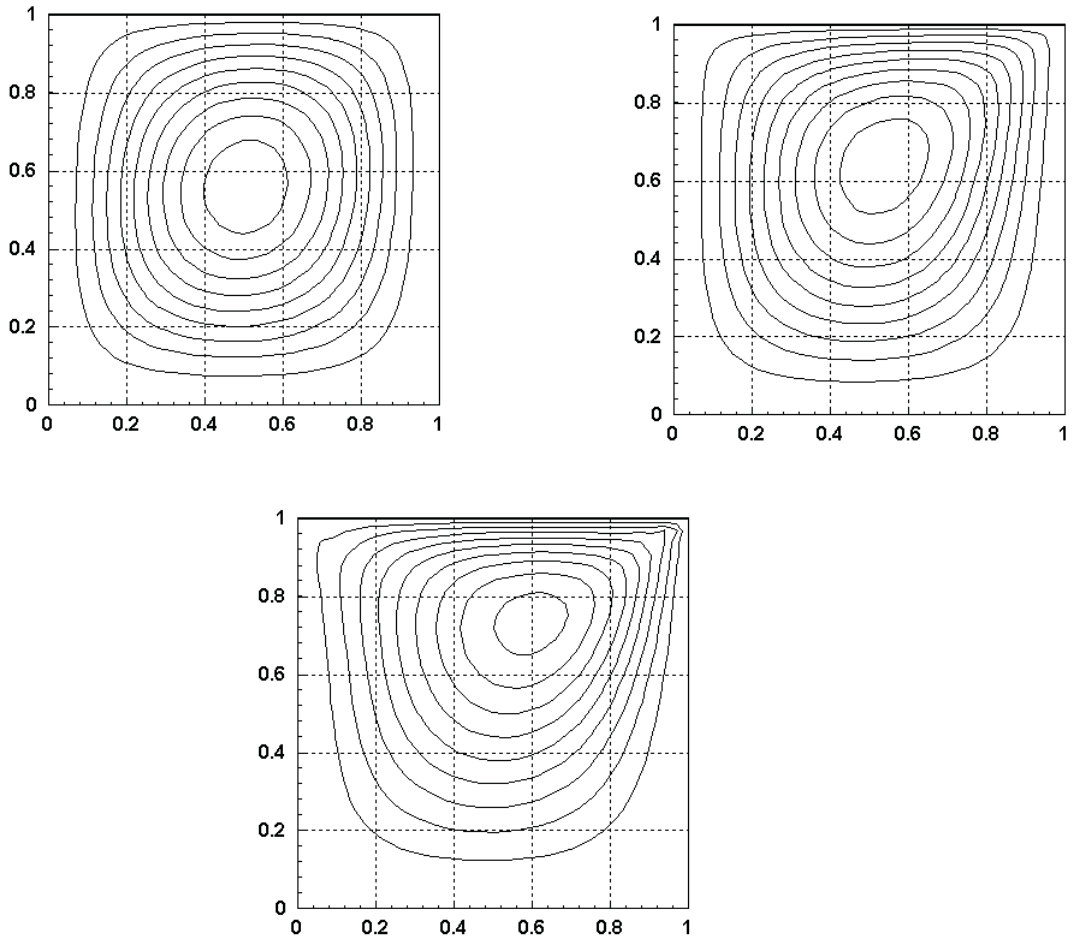

Figure 6.9: Stream function contours for $Ma = 1$ (equally spaced (0.150625) between -1.32 and -0.115), $Ma = 100$ (equally spaced (0.206625) between -1.81 and -0.157) and $Ma = 1000$ (equally spaced (0.4383) between -3.9234 and -0.417).

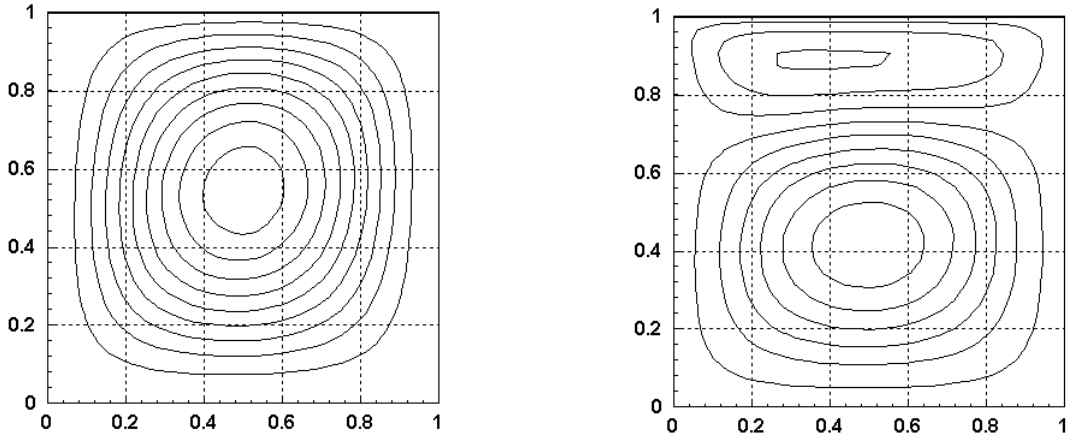

Figure 6.10: Stream function contours for $Ma = -10$ (equally spaced (0.143875) between -1.26 and -0.109) and $Ma = -100$ (equally spaced (0.133) between -0.71 and 0.354).

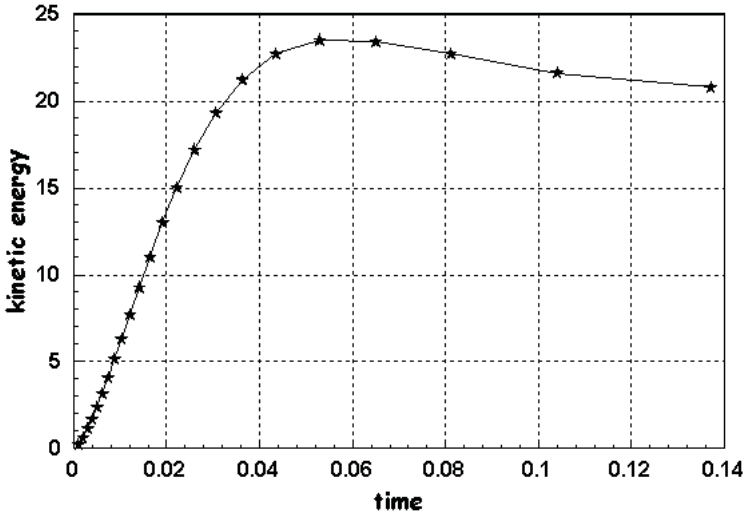

Figure 6.11: Nondimensional kinetic energy plotted as a function of time for $Pr = 0.71$, $Ra = 1000$ and $Ma = 100$ in a unit square.

Table 6.7: Computational effort for the Rayleigh-Benard-Marangoni problem, $Pr = 0.71$, $Ra = 1000$ and $Ma = 100$ in a unit square.

Case	$ntstep$	$nrejec$	nsa	c_{effort}
Fixed Δt	118	0	272	1
Control 1	23	0	75	0.28
Control 2	13	0	57	0.21
Winget&Hughes	25	0	80	0.29

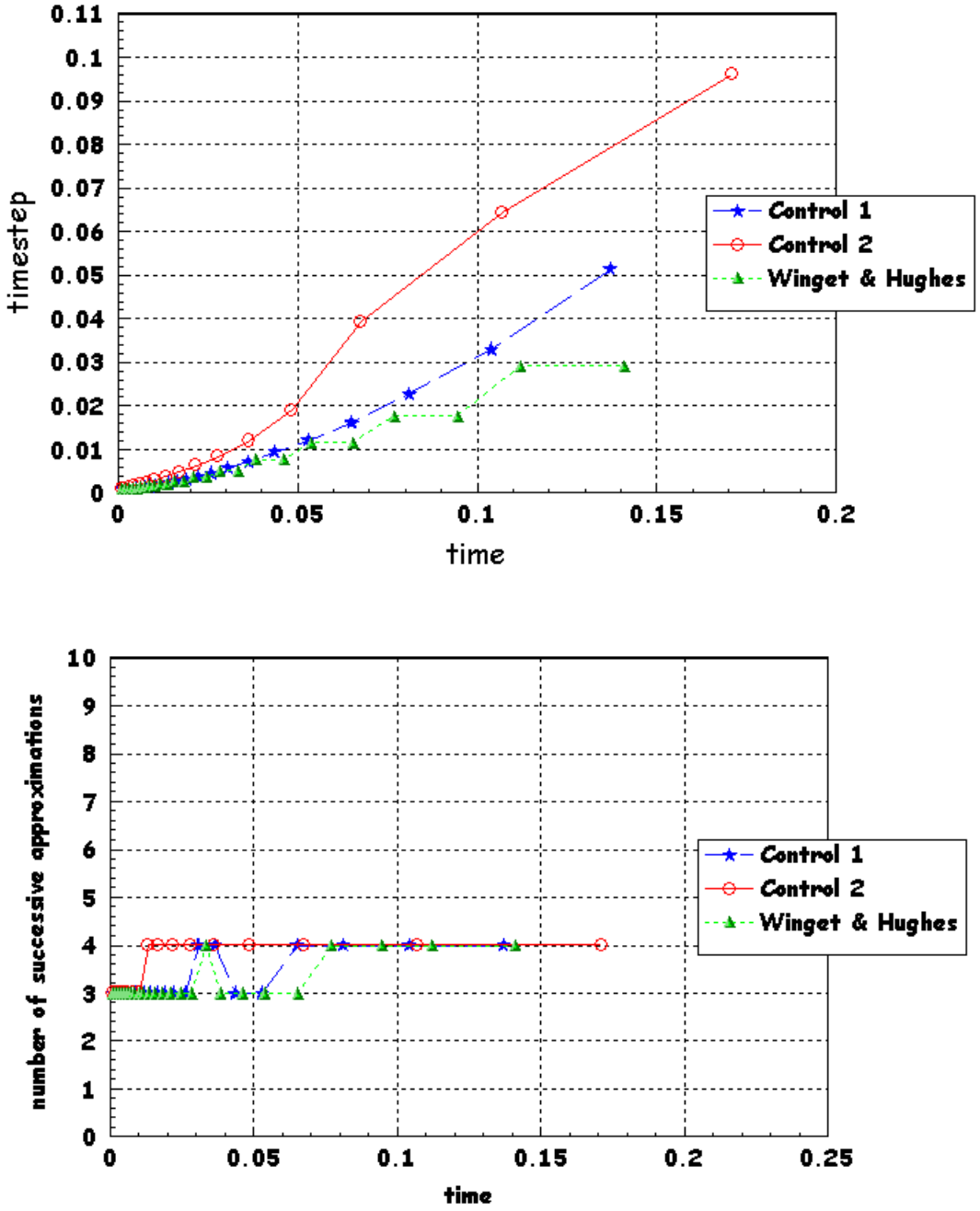

Figure 6.12: Timestep variation (top) and number of successive approximations (bottom) using Control 1, Control 2 and the Winget and Hughes approach for $Pr = 0.71$, $Ra = 1000$ and $Ma = 100$ in a unit square.

Chapter 7

Heat and Mass Transfer Problems

In this Chapter, we solve simultaneous heat and mass transfer by natural convection above horizontal surfaces. Numerical results for different problems with several parameters that influence the convection are obtained and compared with reported experiments.

7.1 Dimensionless Equations

We study natural convection with combined buoyancies of heat and mass diffusion over horizontal surfaces using a numerical experiment similar to the problem reported in [65]. The geometry and coordinate system are shown in Figure 7.1, where the length of the horizontal surface is L, the temperature of the lower heated surface is T_w and the concentration of the diffusing species is c_w. We assume that the flow is two-dimensional and laminar, the thermo-physical properties of the fluid are constant, and viscous dissipation are negligible. Under these assumptions, the flow, thermal, and concentration fields adjacent to the horizontal surface can be described by the following equations,

$$\frac{\partial u}{\partial x} + \frac{\partial v}{\partial y} = 0 \tag{7.1}$$

$$\frac{\partial u}{\partial t} + u\frac{\partial u}{\partial x} + v\frac{\partial u}{\partial y} = -\frac{1}{\rho}\frac{\partial p}{\partial x} + \nu\left(\frac{\partial^2 u}{\partial x^2} + \frac{\partial^2 u}{\partial y^2}\right) \tag{7.2}$$

$$\begin{aligned}\frac{\partial v}{\partial t} + u\frac{\partial v}{\partial x} + v\frac{\partial v}{\partial y} &= -\frac{1}{\rho}\frac{\partial p}{\partial y} + \nu\left(\frac{\partial^2 v}{\partial x^2} + \frac{\partial^2 v}{\partial y^2}\right) \\ &- g\beta_T(T - T_\infty) + g\beta_c(c - c_\infty)\end{aligned} \tag{7.3}$$

$$\frac{\partial T}{\partial t} + u\frac{\partial T}{\partial x} + v\frac{\partial T}{\partial y} = \alpha_T\left(\frac{\partial^2 T}{\partial x^2} + \frac{\partial^2 T}{\partial y^2}\right) \tag{7.4}$$

$$\frac{\partial c}{\partial t} + u\frac{\partial c}{\partial x} + v\frac{\partial c}{\partial y} = \alpha_c\left(\frac{\partial^2 c}{\partial x^2} + \frac{\partial^2 c}{\partial y^2}\right) \tag{7.5}$$

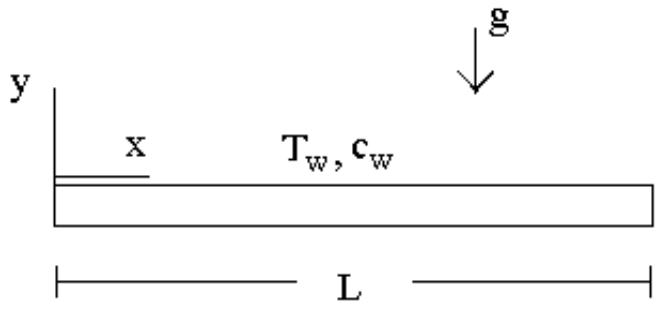

Figure 7.1: Geometry and coordinate system.

in $\Omega \times I$, where $I = (0, \bar{t}]$ is the time interval, u is the horizontal component of the velocity, v is the vertical component of the velocity, c is the concentration of the diffusing species, T is the temperature, p is the pressure, ρ is the density, ν is the kinematic viscosity, g is the gravitational acceleration, β_T is the coefficient of thermal expansion, β_c is the volumetric coefficient due to concentration, T_∞ and c_∞ are the reference remote temperature and concentration, α_T is the thermal diffusivity and α_c is the species diffusion coefficient.

In order to make the results more general in their applicability, the above equations are scaled using the following dimensionless variables:

$$\begin{aligned} & x^* = \frac{x}{L}, \quad y^* = \frac{y}{L}, \quad t^* = \frac{tu_0}{L}, \quad u^* = \frac{u}{u_0}, \quad v^* = \frac{v}{v_0}, \\ & u_0 = \sqrt{g\beta_T \Delta T L}, \quad T^* = \frac{T - T_\infty}{\Delta T}, \quad c^* = \frac{c - c_\infty}{\Delta c}, \quad p^* = \frac{p}{\rho u_0^2} \end{aligned} \tag{7.6}$$

where $\Delta T = T_w - T_\infty$ and $\Delta c = c_w - c_\infty$ are the initial temperature and concentration differences, respectively. Substituting these relations into (7.1)-(7.5), we get the nondimensional form of mass conservation, two momentum, energy conservation and species conservation equations

$$\frac{\partial u}{\partial x} + \frac{\partial v}{\partial y} = 0 \tag{7.7}$$

$$\frac{\partial u}{\partial t} + u\frac{\partial u}{\partial x} + v\frac{\partial u}{\partial y} = -\frac{\partial p}{\partial x} + \frac{1}{\sqrt{Gr}}\left(\frac{\partial^2 u}{\partial x^2} + \frac{\partial^2 u}{\partial y^2}\right) \tag{7.8}$$

$$\begin{aligned} \frac{\partial v}{\partial t} + u\frac{\partial v}{\partial x} + v\frac{\partial v}{\partial y} &= -\frac{\partial p}{\partial y} + \frac{1}{\sqrt{Gr}}\left(\frac{\partial^2 v}{\partial x^2} + \frac{\partial^2 v}{\partial y^2}\right) \\ &\quad - T + Nc \end{aligned} \tag{7.9}$$

$$\frac{\partial T}{\partial t} + u\frac{\partial T}{\partial x} + v\frac{\partial T}{\partial y} = \frac{1}{\sqrt{Gr}Pr}\left(\frac{\partial^2 T}{\partial x^2} + \frac{\partial^2 T}{\partial y^2}\right) \tag{7.10}$$

$$\frac{\partial c}{\partial t} + u\frac{\partial c}{\partial x} + v\frac{\partial c}{\partial y} = \frac{1}{\sqrt{Gr}Sc}\left(\frac{\partial^2 c}{\partial x^2} + \frac{\partial^2 c}{\partial y^2}\right) \tag{7.11}$$

where we have dropped the superscript * for simplicity. The non-dimensional constants are: the thermal Grashof number $Gr = \frac{g\beta_T \Delta T L^3}{\nu^2}$, the Prandtl number $Pr = \frac{\nu}{\alpha_T}$, the Schmidt number $Sc = \frac{\nu}{\alpha_c}$ and the Buoyancy number $N = \frac{\beta_c \Delta c}{\beta_T \Delta T}$. In the momentum equation (7.9), the buoyancy ratio N is the defining parameter for the relative strengths between species and thermal buoyancies. The thermal buoyancy acts vertically upward. The direction of species-generated buoyancy force depends on the molecular weight of the species relative to the medium in which it diffuses. Boundary and initial conditions complete the mathematical statement of the problem and will be discussed in the next section.

7.2 Numerical Experiments

We solve the problem (7.7)-(7.11) assuming that the Prandtl and Schmidt numbers are equal and as a consequence, the thermal and concentration fields are identical. First, we consider a numerical experiment for thermal convection, i.e., $N = 0$, over a horizontal surface with a central plume, and our results are compared to experimental data given by Ishiguro et al. in [47] and numerical calculations presented by Sripada and Angirasa in [65]. Then, we calculate the approximate solutions for a test problem shown by Sripada and Angirasa in [65] with $N = -1$.

The artificial boundary conditions, for the rectangular domain $0 \leq x \leq 1, 0 \leq y \leq 0.5$, are shown in Figure 7.2. At the lower wall ($y = 0, 0 < x < 1$), we assume no slip condition, $u = v = 0$, and temperature and species concentration equal to 1, $T = c = 1$, for the simulation. On the vertical sides, we assume zero vertical velocity, $v = 0$, and zero flux for the horizontal velocity, $\frac{\partial u}{\partial x} = 0$. In the inflow, we impose temperature and species concentration equals to zero, $T_{in} = c_{in} = 0$, and in the outflow, we assume temperature and species concentration flux equals to zero, $\frac{\partial T}{\partial x}|_{out} = \frac{\partial c}{\partial x}|_{out} = 0$. This can be accomplished in the code by testing for the sign of the appropriate velocity component on the boundary. On the open horizontal top ($y = 0.5$, $0 \leq x \leq 1$), conditions similar to the vertical sides are applied: $u = 0$, $\frac{\partial v}{\partial y} = 0$, $T_{in} = c_{in} = 0$ and $\frac{\partial T}{\partial y}|_{out} = \frac{\partial c}{\partial y}|_{out} = 0$. For the initial conditions, we assume that $u = v = 0$ and $T = c = 0$ for all values of x and y. This physically means that the lower surface is impulsively heated at $t = 0$, and the species concentration is simultaneously increased to a constant value on the surface.

In the first experiment, we solve the problem for thermal convection, i.e., $N = 0$, over a horizontal surface with a central plume. Numerical calculations are carried

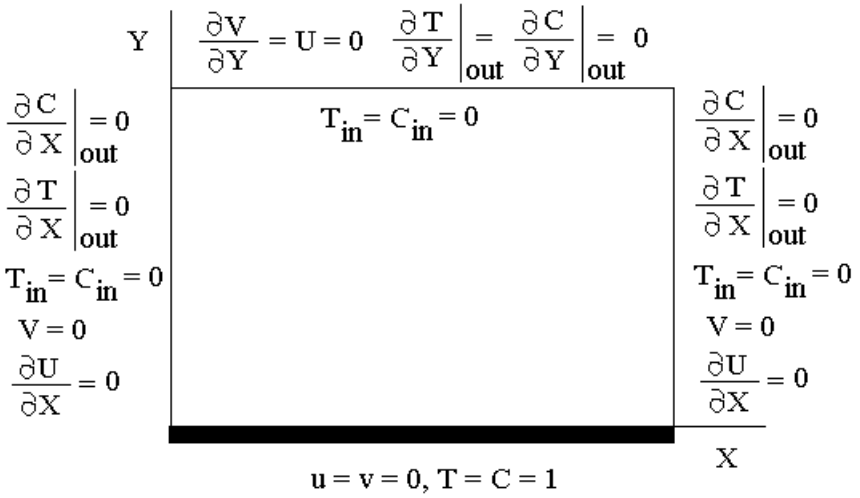

Figure 7.2: Artificial Boundary Conditions of the Problem.

out for $Pr = Sc = 7$, and $Gr = 0.2 \times 10^5$. The approximate velocities, temperature and species concentration are calculated using 9-node isoparametric quadrilateral elements in a uniform mesh of 32×16 elements, and we use a fixed timestep size of 10^{-3}. The steady-state is achieved when the nondimensional kinetic energy at two different timesteps reaches a difference less than 10^{-4}. The Nusselt number, defined as $Nu = \int_0^1 (-\frac{\partial T}{\partial y})_{y=0}\, dx$, is obtained and compared with the numerical experiments of [65] and the experimental data of [47], see Table 7.1. The agreement is found to be good.

	Nu
Sripada et al. [65]	12.22
Ishiguro et al. [47]	12.8 ± 0.1
Present	12.936

Table 7.1: Comparison with experimental data [47] and numerical calculations [65] for $N = 0$ ($Pr = Sc = 7$, and $Gr = 0.2 \times 10^5$).

In the second experiment, we assume $Pr = Sc = 0.7$, $Gr_T = 10^5$ and $N = -1$. The finite element mesh and the timestep size are the same used in the first example. When $N = -1$ for $Pr = Sc$, the thermal and species buoyancies are equal in magnitude and opposite in direction with thermal buoyancy acting vertically upward, and the species buoyancy opposing it. Hence, they cancel out each other, resulting in no flow at all. When $N \geq 0$, the flow resembles that of pure thermal convection. Here the fluid is entrained from the side, and partly from the top, as shown by the velocity field in Figure 7.3. The flow and transport are steady in this

example. The isotherm contours are shown in Figure 7.4, and we observe the central plume which rises vertically upward, as expected. The patterns match well with the flow visualizations of Ishiguro et al. in [47] and contour plots presented by Sripada and Angirasa in [65].

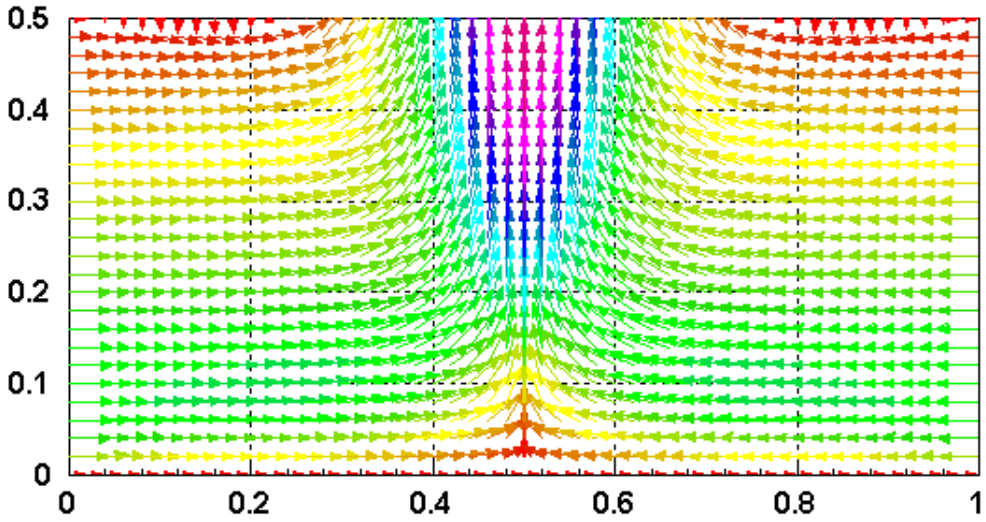

Figure 7.3: Velocity field for $Gr = 10^5$, $N = -1$ and $Pr = Sc = 0.7$.

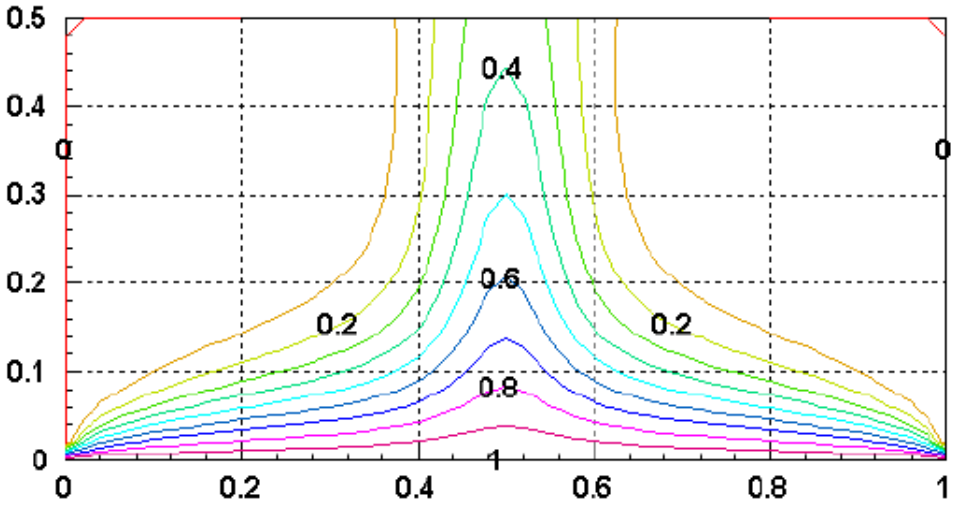

Figure 7.4: Isotherm contours for $Gr = 10^5$, $N = -1$ and $Pr = Sc = 0.7$.

We next solve the problem with adaptive timestepping using Control 1 and the approach suggested by Winget and Hughes. We start with a minimum timestep size of 0.001, and we allow a maximum timestep size of 0.1. We define tolerances of 0.001 and 0.01 for changes in nodal velocities and temperature for any timestep, respectively. The PID parameters here are again $k_p = 0.075$, $k_i = 0.175$ and $k_d =$

0.01. First, we show in Figure 7.5 the nondimensional kinetic energy plotted as a function of time for $Gr = 10^5$, $N = -1$ and $Pr = Sc = 0.7$. Then, we plot the timestep variation in Figure 7.6. We observed that the controller allows the timestep grows in a small time interval around $t = 4$, which corresponds to the interval where the kinetic energy decrease from its maximum value. Further, we may note in Figure 7.6 that the maximum timestep is just 1.4 times the minimum specified value. However, just after the instant which the kinetic energy starts to grow again, the timestep size assumes its minimum value, $\Delta t = 0.001$, and it remains constant until the end of the calculations. We see that the controller chooses the timesteps in conformity with the physical behavior of the solution.

Table 7.2 shows the total number of time steps, *ntstep*, the number of rejected steps, *nrejec*, the total number of successive approximations, *nsa*, and the total number of Newton iterations, *nnewt*, when we solve the problem with a fixed timestep size of 10^{-3} and adaptive timestepping using Control 1. We can observe in Table 7.2 that the number of successive approximations and Newton iterations necessary to calculate the approximate solutions are reduced using Control 1, although this improvement is not very significant. Numerical experiments indicate that the complexity of the problem requires small timesteps and tolerances to have convergence of the successive approximation process in the Navier-Stokes equations. That is, the minimum timestep chosen is already the biggest value allowed to maintain the user-specified accuracy requirement and to obtain convergence of the successive approximations. Parametric studies demonstrated that the problem was not related to the choice of the PID parameters. We also solved the problem using the approach suggested by Winget and Hughes. In this case the timestep selection algorithm did not produce timestep sizes bigger than the minimum value, which confirms the overall behavior of Control 1. Due to computational and time limitations, we do not discuss in the present work more numerical experiments related to this application problem.

Table 7.2: Comparison results using fixed timestep size and Control 1.

	ntstep	*nrejec*	*nsa*	*nnewt*
Fixed Δt	12001	0	36003	36003
Control 1	11785	45	35835	35490

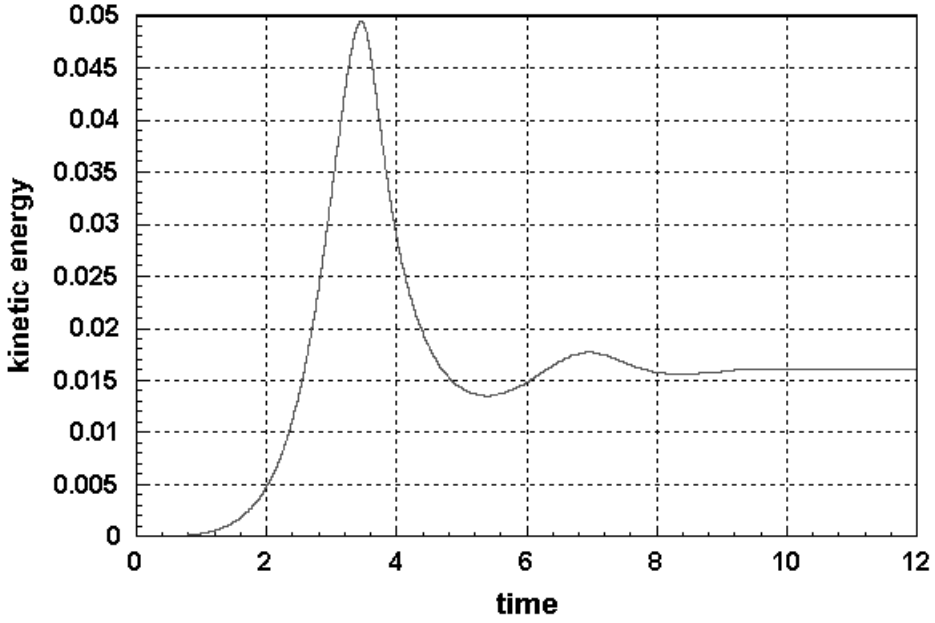

Figure 7.5: Nondimensional kinetic energy for $Gr = 10^5$, $N = -1$ and $Pr = Sc = 0.7$.

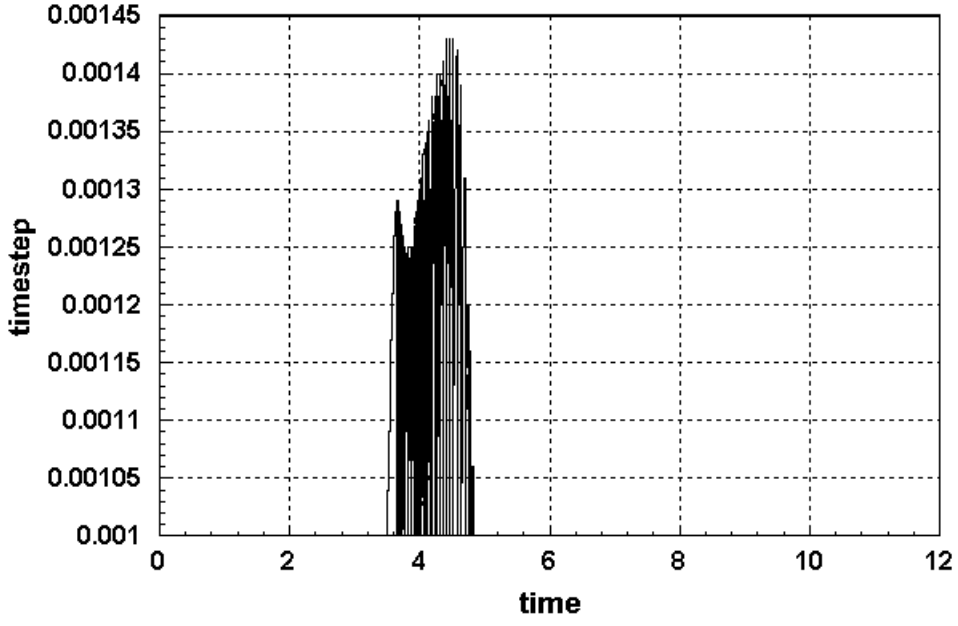

Figure 7.6: Timestep variation using Control 1 for $Gr = 10^5$, $N = -1$ and $Pr = Sc = 0.7$.

Chapter 8

Conclusions

In this dissertation we introduced two adaptive timestep selection schemes based on feedback control theory to increase the robustness of our finite element formulation of coupled incompressible viscous flow and transient heat and mass transfer with surface effects included. We solved chemical reaction systems, Rayleigh-Benard and Rayleigh-Benard-Marangoni flows, heat and mass transfer by natural convection for several case problems with different parameters that influence the numerical experiments. The finite element flow formulation is based on a penalty Galerkin method and the transport equations utilize a SUPG formulation. The algorithm employs an iteratively decoupled scheme. In the application problems, we were interested in obtaining steady-state and transient solutions using fixed timestep sizes and adaptive timestep sizes to test the efficiency of our controllers to solve the related class of coupled problems. We also compared our controllers with a timestep selection algorithm found in the literature.

A standard timestep selection algorithm uses a estimate of the local truncation error to adjust the stepsize in accordance with a user-specified accuracy requirement. This kind of algorithm normally performs quite well. However, there are differential equations and integration methods for which its performance is unacceptable. The stepsize oscillates tremendously and the number of rejected steps is too high. As a consequence, much computation time is spent recalculating rejected steps and changing the stepsize. To overcome this potential problems, we investigated two PID control algorithms for timestep selection based on controlling accuracy or the convergence rate of the successive iterations. We performed parametric studies for different values of PID parameters (k_P, k_I, k_D) for two test problems, to verify whether the PID controller is robust or not. Although feedback control theory provides techniques to choose PID parameters, robustness is required when a general

finite element method is used for a wide range of different situations. The controller was found to be very robust, allowing us to fix the values of the PID parameters for all the numerical experiments performed subsequently.

Another important issue is to assess solution accuracy when the timestep control strategies are applied to a specified problem. For this investigation, we used a validation problem for the transport equations and a Rayleigh-Benard problem, and results were compared with fixed timestep, the adaptive timestep scheme suggested by Winget and Hughes, and our PID control approaches. Based on the numerical studies, it was concluded that we may find approximate solutions with a smaller number of steps without any significant loss of accuracy. For example, in the second problem both approaches produced good results with percentage errors no more than 1% for all cases. The controllers produced a smooth variation of timesteps, while the Winget and Hughes approach yielded a curve with several steps. The results suggest that a robust control algorithm is possible. Further, computational cost of the selection procedures are negligible, since they involve only storing a few extra vectors, computation of norms and evaluation of kinetic energy.

In Chapter 5 we demonstrated the efficiency of our first control to solve nonlinear flow and reactive transport. We were interested in state-state and transient solutions, and the performance of Control 1 to reduce computational costs. We measured the computational effort by the number of Newton iterations, and we were able to obtain solutions with a much smaller number of steps without any significant loss of accuracy. For instance, we have a 3.75 times improvement in the computational effort to compute the solution in the nonisothermal reaction problem. This very good improvement in the computational effort is due to the very small timestep needed to obtain convergence of the nonlinear iterations in the beginning of the transport calculations. In this example, efficient computation of the transport process demands the use of a timestep selection algorithm, since the process is highly nonlinear because of an exponential chemical reaction term.

The efficiency of Control 2 was verified in the numerical simulations of the Rayleigh-Benard-Marangoni problems. In this case, the computational effort was measured by the total number of successive approximations needed to calculate the velocity field using one of the controllers divided by the number of successive approximations obtained using a fixed timestep size. We observed that the number of successive approximations necessary to calculate the approximate solutions is reduced for all approaches, and Control 2 presented the best results. In some of the

test problems, the choice of the timestep in Control 2 was dominated by the convergence rate of the successive iterations, and in other cases by the changes in the kinetic energy. However, in all cases the kinetic energy appeared to be a suitable parameter to improve the timestep selection when coordinated with the convergence rate control of the nonlinear iterations.

Numerical studies on simultaneous heat and mass transfer by natural convection above horizontal surfaces were performed with fixed timestep sizes in Chapter 7. Preliminary results obtained using Control 1 have shown that the problem requires very small timesteps to maintain the user-specified accuracy requirement. The controller allows the timestep size to grow from the minimum value allowed, but reduces the timestep to this value after some steps. After that, the controller keeps the timestep size to the minimum value until the steady-state is reached. Parametric studies demonstrated that the problem was not related to the choice of the PID parameters. The timestep selection algorithm suggested by Winget and Hughes did not produce timestep sizes bigger than the minimum value, which confirms the overall behavior of Control 1. Experiments indicate that the complexity of the problem requires small timesteps to have convergence of the successive approximation process in the Navier-Stokes equations. However, more numerical experiments are necessary to better understand the physics and the performance of the controllers.

Future studies include solving the coupling between Marangoni convection and double diffusion convection in a multi-cavity system with a moving free surface. Important practical applications are related to this type of problems, and we also need to investigate the performance of the controllers to solve them. For this study, we need iterative solutions of the linear systems instead of the direct frontal solver used until now. Preliminary numerical studies with the GMRES method and the penalty formulation indicated that another finite element formulation for the Navier-Stokes equations may be more suitable to this class of application problems. Another natural extension of this work is the utilization of the controllers for timestep selection in the finite element simulations of 3D viscous flows involving heat transfer and surface tension effects. We also need to investigate partitioned analysis procedures for coupled systems to improve the efficiency of the numerical calculations [12]. In the partitioned solution approach, the solution is separately advanced in time over each partition chosen in accordance with physical or computational characteristics. Finally, a related PID controller was developed by Valli, Catabriga and Coutinho in [77, 19] to select the CFL condition to accelerate convergence toward steady state

for a local-time-stepping strategy in compressible gas dynamic simulation.

References

[1] B.F. Armaly, F. Durst, J.C.F. Pereira, and B. Schönung. Experimental and theoretical investigation of backward-facing step flow. *J. Fluid Mech.*, 127:473–496, 1983.

[2] I. Babuška and A.K. Aziz. Survey lectures on the mathematical foundations of the finite element method. In A.K. Aziz, editor, *The Mathematical Foundations of the Finite Element Method with Applications to Partial Differential Equations*. Academic Press, New York, 1972.

[3] E. Barragy and G.F. Carey. Stream function vorticity solution using high-p element-by-element techniques. *Communications in Numerical Methods in Engineering*, 9:387–395, 1993.

[4] K-J Bathe. *Finite Element Procedures*. Prentice–Hall, Inc., Upper Saddle River, NJ, 1996.

[5] A. Bejan. *Convection Heat Transfer*. Wiley-Interscience, New York, 1984.

[6] H. Bénard. Les tourbillons cellulaires dans une nappe liquide. *Rev. Gén. Sci. Pure Appl.*, 11:1261–1271,1309–1323, 1900.

[7] R.B. Bird, W.E. Stewart, and E.N. Lightfoot. *Transport Phenomena*. John Wiley & Sons, New York, NY, 1960.

[8] J. Blasco, R. Codina, and A. Huerta. A fractional step method for the incompressible navier-stokes equations related to a predictor-multicorrector algorithm. *Int. J. Numerical Methods Fluids*, 28:1391–1419, 1998.

[9] G.J. Borse. *Numerical Methods with Matlab - A Resourse for Scientists and Engineers*. PWS Publishing Company, New York, NY, 1997.

[10] F. Brezzi. On the existence, uniqueness and approximation of saddle-point problems arising from Lagrangian multipliers. *Rev. Fr. Autom. Inf. Rech. Oper. Numer. Anal.*, pages 129–151, 1974.

[11] A.N. Brooks and T.J.R. Hughes. Streamline Upwind/Petrov-Galerkin formulations for convection dominated flows with particular emphasis on the incompressible Navier-Stokes equations. *Comput. Methods Appl. Mech. and Engrg.*, 32:199–259, 1982.

[12] C.A.Fellipa, K.-C. Park, and C. Farhat. Partitioned analysis of coupled systems. In *Proc. 4th World Congress on Computational Mechanics CD-ROM, CIMNE*, Barcelona, Spain, 1998.

[13] G.F. Carey, C. Harlé, R. McLay, and S. Swift. MPP solution of Rayleigh-Benard-Marangoni flows. In *Supercomputing 97*, pages 1–13, San Jose, CA, 1997.

[14] G.F. Carey and R. Krishnan. Penalty approximation of Stokes flow. *Comput. Meths. Appl. Mech. Engrg.*, 35:169–206, 1982.

[15] G.F. Carey and R. Krishnan. Penalty finite element methods for the Navier–Stokes equations. *Comput. Meths. Appl. Mech. Engrg.*, 42:183–224, 1984.

[16] G.F. Carey and J.T. Oden. *Finite Elements: Fluid Mechanics*, volume 6. Prentice–Hall, Inc., Englewood Cliffs, NJ, 1986.

[17] G.F. Carey, A. Pehlivanov, Y. Shen, and A. Base. Some questions concerning the least-squares mixed navier-stokes problem. Technical report, TICOM, Austin, TX, 1994.

[18] B. M. Carpenter and G.M. Homsy. Combined buoyant-thermocapillary flow in a cavity. *J.Fluid Mech.*, 207:121–132, 1989.

[19] L. Catabriga, A.M.P. Valli, and A.L.G.A. Coutinho. Acceleration strategies for stabilized finite element solution of steady compressible flows. In *22st Iberian Latin American Congress on Computational Methods in Engineering CD-ROM*, Campinas, SP, Brazil, November 2001.

[20] R. Codina. Comparison of some finite element methods for solving the diffusion-convection-reaction equation. *Comput. Methods Appl. Mech. and Engrg.*, 156:185–210, 1998.

[21] R. Codina. A nodal-based implementation of a stabilized finite element method for incompressible flow problems. *Int. J. Numerical Methods Fluids*, 33:737–766, 2000.

[22] R. Codina. Pressure stability in fractional step finite element methods for incompressible flows. *Journal of Computational Physics*, 170:112–140, 2001.

[23] R. Codina, E. Oñate, and M. Cervera. The intrinsic time for the streamline upwind - PG formulation using quadratic elements. *Comput. Methods Appl. Mech. and Engrg.*, 94:239–262, 1992.

[24] A.L.G.A. Coutinho and J.L.D. Alves. Parallel finite element simulation of miscible displacements in porous media. *SPE Journal*, 4(1):487–500, 1996.

[25] M.J. Crochet, F.T. Geyling, and J.J. Van Schaftingen. Finite element method for calculating the horizontal bridgman growth of semiconductor crystals. *Finite Elements in Fluids*, 6:321–337, 1985.

[26] M.A. Cruchaga. A study of the backward-facing step problem using a generalized streamline formulation. *Communications in Numerical Methods in Engineering*, 14:697–708, 1998.

[27] M.B. Davis and G.F. Carey. Parallel multilevel solution of Rayleigh-Benard-Marangoni problems. *Int. J. Num. Meth. Heat & Fluid Flow*, 10(3):248–267, 2000.

[28] P.A.B. de Sampaio and A.L.G.A. Coutinho. Simulation of free and forced convection incompressible flows using an adaptive parallel/vector finite element procedure. *Int. J. Num. Meth. Fluids*, 29:289–309, 1999.

[29] G. de Vahl Davis. Laminar natural convection in a enclosed rectangular cavity. *Int. J. Heat Mass Transfer*, 11:1675–1693, 1968.

[30] G. de Vahl Davis. Natural convection in a square cavity: A comparison exercise. *Int. J. Num. Meth. Fluids*, 3:227–248, 1983.

[31] G. de Vahl Davis. Natural convection of air in a square cavity: A benchmark numerical solution. *Int. J. Num. Meth. Fluids*, 3:249–264, 1983.

[32] R.C. Dorf and R.H. Bishop. *Modern Control Systems.* Addison-Wesley Publishing Company, 1995.

[33] B.A. Finlayson. *The Method of Weighted Residuals and Variational Principles*, volume 87 of *Mathematics in Science and Engineering*. Academic Press, New York, NY, 1972.

[34] D.K. Gartling. A test problem for outflow boundary conditions - flow over a backward-facing step. *Internat. J. Numer. Methods Fluids*, 11:953–967, 1990.

[35] D.K. Gartling and E. Becker. Finite element analysis of viscous incompressible fluid flow. *Comput. Meths. Appl. Mech. Engrg.*, 8:1–2,51–60,127–138, 1976.

[36] J.D. Powell G.F. Franklin and A. Emami-Naeini. *Feedback Control of Dynamic Systems*. Addison-Wesley Publishing Company, 1994.

[37] P.M. Gresho, R.L. Sani, and M.S. Engelman. *Incompressible Flow and the Finite Element Method - Advection-Diffusion and Isothermal Laminar Flow*. John Wiley and Sons Ltd, Chichester, 1999.

[38] M. Griebel, T. Dornseifer, and T. Neunhoeffer. *Numerical Simulation in Fluid Dynamics - A Practical Introduction*. SIAM, Philadelphia, PA, 1998.

[39] K. Gustafsson, M. Lundh, and G. Söderlind. A PI stepsize control for the numerical solution for ordinary differential equations. *BIT*, 28:270–287, 1988.

[40] K. Gustafsson and G. Söderlind. Control strategies for the iterative solution of nonlinear equations in ODE solvers. *SIAM J. Sci. Comput.*, 18(1):23–40, 1997.

[41] E. Hairer and G. Wanner. *Solving Ordinary Differential Equations II: Stiff and Differential-Algebraic Problems*. Springer–Verlag, New York, NY, 1993.

[42] J.C. Heinrich. A finite element model for double diffusive convections. *Int. J. Numer. Meth. Eng.*, 20:447–464, 1984.

[43] T.J.R. Hughes. *The Finite Element Method*. Prentice–Hall, Inc., Englewood Cliffs, NJ, 1987.

[44] T.J.R. Hughes and A.N. Brooks. A multi-dimensional upwind scheme with no crosswind diffusion. In T.J.R. Hughes, editor, *Finite Element Methods for Convection Dominated Flows, AMD*, volume 34, pages 19–35. ASME, New York, 1979.

[45] T.J.R. Hughes, L.P. Franca, and G.M. Hulbert. A new finite element formulation for computational fluid dynamics: Viii. the galerkin/least-squares methods for advective-diffusive equations. *Comput. Methods Appl. Mech. and Engrg.*, 73:173–189, 1989.

[46] B.M. Irons. A frontal solution program for finite element analysis. *Internat. J. Numer. Meth. Eng.*, 2:5–12, 1970.

[47] R. Ishiguro, T. Abe, H. Nagase, and S. Nakanishi. Heat transfer and flow instability of natural convection over upward-facing horizontal surfaces. In *Sixth International Heat Transfer Conference*, number NC-8 in 2, pages 229–234, 2000.

[48] B.P. Jacob and N.F.F. Ebecken. Adaptive time integration of nonlinear structural dynamic problems. *Eur. J. Mech*, 12(2):277–298, 1993. A/Solids.

[49] Z. Johan, T.J.R. Hughes, and F. Shakib. A globally convergent matrix-free algorithm for implicit time-marching schemes arising in finite element analysis in fluids. *Comput. Methods Appl. Mech. and Engrg.*, 87:281–304, 1991.

[50] C. Johnson and J. Pitkäranta. Analysis of some mixed finite elements related to reduced integration. Technical report, Chalmers University of Technology and University of Göteborg, Göteborg, Sweden, 1980.

[51] D. Kahaner, C. Moler, and S. Nash. *Numerical Methods and Software.* Prentice–Hall, Inc., Upper Saddle River, NJ, 1992.

[52] B.C. Kuo. *Automatic Control Systems.* Prentice Hall, Inc., seventh edition, 1995.

[53] O.A. Ladyzhenskaya. *The Mathematical Theory of Viscous Incompressible Flows.* Gordon and Breach, New York, NY, second edition, 1969.

[54] J.M. Leone and P.M. Gresho. Finite element simulations of steady, two-dimensional, viscous incompressible flow of a step. *J. Comp. Phys.*, 41:167–191, 1981.

[55] D.S. Malkus and T.J.R. Hughes. Mixed finite element methods - reduced and selective integration techniques: A unification of concepts. *Comput. Methods Appl. Mech. and Engrg.*, 15:63–81, 1978.

[56] T. Maxworthy. The dynamics of double-diffusive gravity currents. *J. Fluid Mech.*, 128:259–282, 1983.

[57] J.T. Oden and L.C. Wellford. Analysis of flow of viscous fluids by the finite element method. *AIAA J.*, 10(12):1590–1599, 1972.

[58] E.E. Petersen. *Chemical Reaction Analysis*. Prentice–Hall, Englewood Cliffs, NJ, 1965.

[59] W.H. Press, S.A. Teukolsky, W.T. Vetterling, and B.P. Flannery. *Numerical Recipes in C - The Art of Scientific Computing*. Cambridge University Press, New York, NY, second edition, 1992.

[60] A. Ralston and P. Rabinowitz. *A First Course in Numerical Analysys*. Dover Publications, second edition, 2001.

[61] R.McLay and G.F. Carey. Coupled heat transfer and viscous flow, and magnetic effects in weld pool analysis. *Int. J. Numerical Methods Fluids*, 9:713–730, 1989.

[62] M.Z. Saghir, M. Hennenberg, and M.R. Islam. Double diffusive and Marangoni convection in a multi-cavity system. *Int. J. Heat Mass Transfer*, 41(14):2157–2174, 1998.

[63] M.Z. Saghir and M.R. Islam. Displacement of salty water by fresh water in the presence of Marangoni convection. *Intern. J. in Comp. Fluid Dynamics*, 11:303–311, 1999.

[64] Y.J. Song, J.T. Oden, and N. Kikuchi. Discrete LBB-conditions for RIP-finite element methods. Technical report, TICOM Report 80, The Texas Institute for Computational Mechanics, Austin, Texas, 1980.

[65] R.K.L. Sripada and D. Angirasa. Simultaneous heat and mass transfer by natural convection above upward facing horizontal surfaces. *Intern. J. of Non-Linear Mechanics*, 36:1019–1029, 2001.

[66] J. Tanny, C.C. Chen, and C.F. Chen. Effects of iteration between Marangoni and double-diffusive instabilities. *J. Fluid Mech.*, 303:1–21, 1995.

[67] T.E. Tezduyar. Stabilized finite element formulations for incompressible flow computations. *Advances in Applied Mechanics*, 28:1–44, 1992.

[68] T.E. Tezduyar and Y. Osawa. Finite element stabilization parameters computed from element matrices and vectors. *Comput. Methods Appl. Mech. and Engrg.*, 190:411–430, 2000.

[69] J.S. Turner. Double diffusive phenomena. *Ann. Rev. Fluid Mech.*, 6:37–56, 1974.

[70] J.S. Turner. *Buoyancy Effects in Fluids*. Cambrigde Univ. Press, 1979.

[71] A.M.P. Valli, G.F. Carey, and A.L.G.A. Coutinho. Finite element simulation and control of nonlinear flow and reactive transport. In *Proc. 10th Int. Conf. Finite Element in Fluids*, pages 450–455, Tucson, Arizona, January 1998.

[72] A.M.P. Valli, G.F. Carey, and A.L.G.A. Coutinho. Control strategies for timestep selection in simulation of coupled viscous flow and heat transfer. *Communications in Numerical Methods in Engineering*, 18:131–139, 2002.

[73] A.M.P. Valli, L. Catabriga, and A.L.G.A. Coutinho. Acceleration strategies for solution of euler equations using an edge-based supg formulation with shock-capturing. In *ECCOMAS Computational Fluid Dynamics 2001 Conference CD-ROM*, Swansea, Wales, UK, September 2001.

[74] A.M.P. Valli, A.L.G.A. Coutinho, and G.F. Carey. Adaptive control for time step selection in finite element simulation of coupled viscous flow and heat transfer. In *European Conference on Computational Mechanics CD-ROM*, Munchen, Germany, August 1999.

[75] A.M.P. Valli, A.L.G.A. Coutinho, and G.F. Carey. Adaptive stepsize control strategies in finite element simulation of 2D Rayleigh-Benard-Marangoni flows. In *15th Brazilian Congress on Mechanical Sciences CD-ROM*, Águas de Lindóia, SP, Brazil, November 1999.

[76] A.M.P. Valli, A.L.G.A. Coutinho, and G.F. Carey. Adaptive control strategies in finite element simulation of double diffusion and Marangoni convection problems. In *Finite Elements in Flow Problems 2000*, page 71, Austin, Texas, USA, April 2000.

[77] A.M.P. Valli, A.L.G.A. Coutinho, and G.F. Carey. Adaptive control for timestep selection in finite element simulation of coupled viscous flow and simultaneous heat and mass transfer. In *6th Workshop on Computational Meth-*

ods for Oceanic, Atmospheric and Groundwater Flows, Petrópolis, RJ, Brazil, September 2001.

[78] D. Walgraef. *Spatio-Temporal Pattern Formation*. Springer-Verlag, New York, NY, 1997.

[79] J.M. Winget and T.J.R. Hughes. Solution algorithms for nonlinear transient heat conduction analysis employing element-by-element iterative strategies. *Comput. Methods Appl. Mech. and Engrg.*, 52:711–815, 1985.

[80] A. Zebib, G.M. Homsy, and E. Meiburg. High Marangoni number convection in a square cavity. *Phys. Fluids*, 28(12):3467–3476, 1985.

[81] O.C. Zienkiewicz. *The Finite Element Method*. McGraw-Hill, U.K., 1977.